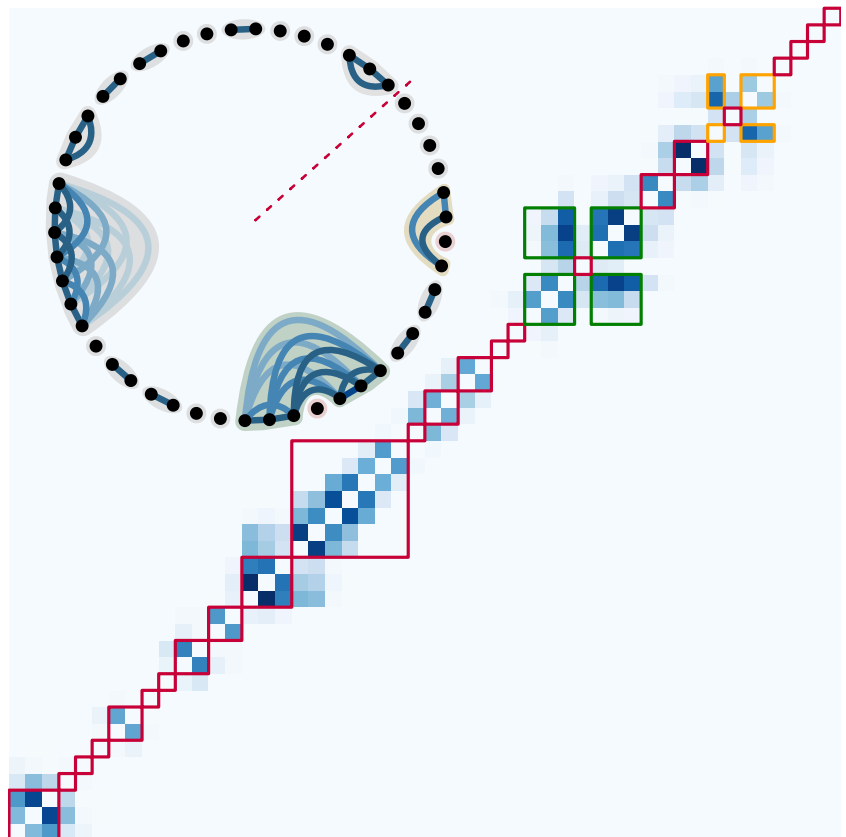


Efficient tensor network simulations of localized and ergodic quantum many-body systems

Dissertation

Kévin Hémerly

Dissertation zur Erlangung des akademischen Grades
Doktor der Naturwissenschaften (Dr. rer. nat.)



Fakultät für Physik

Efficient tensor network simulations of localized and ergodic quantum many-body systems

Kévin Hémerly

Vollständiger Abdruck der von der Fakultät für Physik der Technischen Universität München zur Erlangung des akademischen Grades eines **Doktors der Naturwissenschaften (Dr. rer. nat.)** genehmigten Dissertation.

Vorsitzender: Prof. Dr. Christian Pfleiderer

Prüfer der Dissertation:

1. Prof. Dr. Frank Pollmann
2. Prof. Dr. Michael Knap

Die Dissertation wurde am 05.05.2022 bei der Technischen Universität München eingereicht und durch die Fakultät für Physik am 05.07.2022 angenommen.

Abstract

Out-of-equilibrium quantum many-body systems exhibit a rich variety of behaviors. First we study the propagation of quantum information in an isolated ergodic system using matrix product states. Second we obtain steady states of boundary-driven dissipative systems using matrix product states, and deduce an estimate of the diffusion coefficient. Third we present a strategy to characterize the structure of many-body localized states using correlations and a graph-theory approach.

Kurzfassung

Quanten-Vielteilchensysteme außerhalb des Gleichgewichts weisen eine Vielzahl an Phänomenen auf. Zuerst untersuchen wir die Ausbreitung von Quanteninformation in einem isolierten ergodischen System unter Verwendung von Matrixproduktzuständen. Darüber hinaus analysieren wir Diffusion in randgetriebenen dissipativen Systemen. Abschließend präsentieren wir eine Charakterisierung der Struktur von lokalisierten Vielteilchenzuständen unter Verwendung eines graphentheoretischen Ansatzes.

Contents

Abstract	iii
Kurzfassung	v
List of Publications	1
1 Introduction	3
2 Quantum thermalization: the eigenstates thermalization hypothesis	7
2.1 Elements of random matrix theory: some properties of the Gaussian unitary ensemble	7
2.1.1 Definition	7
2.1.2 The eigenstates of matrices sampled from the Gaussian unitary ensemble	8
2.2 The Structure of the matrix elements of hermitian operators under the Gaussian unitary ensemble	9
2.3 The eigenstate thermalization hypothesis	10
2.3.1 Thermalization in closed quantum system	10
2.3.2 From random matrix theory to thermalization	11
2.3.3 The eigenstate thermalization hypothesis (ETH)	11
2.4 Entanglement of the states of ergodic Hamiltonians	12
3 Localized systems	13
3.1 Anderson localization	13
3.1.1 Localization length: the Thouless formula	13
3.1.2 Disordered spinless fermions in second quantization and the Jordan-Wigner transformation	15
3.2 Many-body localization	15
3.2.1 Local integrals of motions	16
3.2.2 Spin one-half case: the l-bits	18
3.2.3 Dynamical behavior of many-body localized systems	19
3.2.4 Strong randomness renormalization group approaches to many-body localization	19
4 Matrix-product states	25
4.1 The matrix-product state formalism	25
4.1.1 The matrix-product state ansatz	25
4.1.2 Some properties of matrix-product states	27
4.2 Matrix-product state algorithms	28
4.2.1 The density matrix renormalization group	28
4.2.2 Time evolving block decimation	29
4.2.3 The time dependent variational principle using matrix-product states	30

5	Matrix-product state approaches to operator spreading in non-integrable systems	37
5.1	Introduction	37
5.2	Measures of operators spreading in closed quantum systems: the out-of-time-order correlator	38
5.2.1	the out-of-time-order correlator, a measure of the propagation of quantum information	38
5.2.2	The out-of-time-order correlator, a marker of quantum chaos	40
5.3	Numerical considerations: calculating the out-of-time-order correlator with matrix-product states	40
5.4	Results	43
5.4.1	Comparison of the methods with exact results	44
5.4.2	Large systems and range of validity of the approximation	47
5.4.3	Discussion	53
5.5	Conclusion	53
6	Probing diffusion in boundary-driven dissipative systems	55
6.1	Introduction	55
6.2	Probing transport properties using equilibrium steady states	56
6.2.1	The setup	56
6.2.2	Obtaining the diffusion coefficient from the non-equilibrium steady state	56
6.2.3	Lindbladian perturbation theory and linear response theory	57
6.2.4	Matrix-product state implementation	58
6.3	Energy transport	59
6.3.1	Two spin bath	59
6.3.2	Diffusion in the tilted field Ising model	60
6.4	Spin transport	62
6.4.1	The integrable XXZ model	63
6.4.2	The XX ladder	65
6.5	Conclusion	66
7	Identifying correlation clusters in many body localized systems	67
7.1	Introduction	67
7.2	From correlations to graph theory	69
7.3	The modularity, a quality measure of the partition of a graph	70
7.4	Scaling of the modularity with system size	71
7.5	Correlation clusters	71
7.5.1	A graph theory algorithm to obtain correlation clusters	71
7.5.2	Comparison between “entanglement clusters” and “correlation clusters”	72
7.6	Correlation clusters in eigenstates	73
7.6.1	Exploring the many-body localized phase transition based on graph theory and entanglement entropy	74
7.6.2	Exploring the many-body localized phase transition based only on graph theory	75
7.6.3	Variational methods for obtaining highly excited states of many-body localized Hamiltonians	77
7.6.4	Structure of individual eigenstates obtained via matrix-product states	78
7.7	Non-equilibrium dynamics	81
7.7.1	Setup	81

7.7.2	A configuration example	82
7.7.3	Disorder average graph theory quantities	83
7.7.4	Information propagation using pairwise correlation in the σ_z basis	84
7.7.5	Interpretation	85
7.8	Conclusion	85
8	Summary and outlook	87
	Acknowledgments	89
	Appendix	91
	A. Scaling with different modularity thresholds	91
	B. Scaling collapse of the number of clusters using the pairwise correlation functions in the σ^z basis	91
	List of Figures	98
	Bibliography	99

List of Publications

Parts of the content of this thesis have been published in the following Refs. [1,2]. The author of this thesis has made significant and substantial contributions to these publications, ranging from the development of ideas, literature research, analytical calculations, design, development and implementation of numerical codes, to the interpretation of results, and writing of the papers.

- [1] K. Hémary, F. Pollmann, and D. J. Luitz. “Matrix product states approaches to operator spreading in ergodic quantum systems.” *Phys. Rev. B* **100**, p. 104303, 2019. doi:[10.1103/PhysRevB.100.104303](https://doi.org/10.1103/PhysRevB.100.104303).
- [2] K. Hémary, F. Pollmann, and A. Smith. “Identifying correlation clusters in many-body localized systems.” *Phys. Rev. B* **105**, p. 064202, 2022. doi:[10.1103/PhysRevB.105.064202](https://doi.org/10.1103/PhysRevB.105.064202).

Specifically, the chapter about simulating out-of-time-order-correlators (OTOCs) in chapter 5 has been published in Ref. [1]. The chapter about the graph theory approach to the structure of the many-body localized states 7 has been published in [2].

1 Introduction

“The behavior of large and complex aggregates of elementary particles, it turns out, is not to be understood in terms of a simple extrapolation of the properties of a few particles” wrote Anderson in his celebrated paper entitled “More is different” (1972) [3]. He argued that the scale and the complexity of such large aggregates preclude the prediction of their properties by direct applications of the laws of fundamental particles. Instead, he argued, complexity leads to the emergence of entirely new fundamental laws.

Nevertheless, recent progress in experiments, in numerics, as well as in quantum information theory, has rendered the project of “reconstructing” the behavior of matter from microscopic consideration feasible in certain cases. In ground state physics, the invention of the density matrix renormalization group algorithm [4] and subsequently of the tensor network formalism has led to tremendous progress. For one dimensional gapped systems [5], these methods allow for the representation of the ground state wave function on a classical computers with an arbitrary precision. For example, the advent of such algorithms allowed to verify the Haldane conjecture [6] – an intuition based on field theory considerations – which states that the spin-one Heisenberg chain is gapped in the thermodynamic limit. Experimentally, the ever increasing control has led to the possibility of creating artificial quantum systems. An early breakthrough was made with the observation of the Bose-Einstein condensation in dilute gases [7, 8]. Since then, *quantum simulators* have become a corner stone of modern experimental condensed matter physics. Various technologies have been used to implement these artificial quantum systems, including ultracold neutral atoms [9, 10], trapped ions [11] and quantum superconducting circuits [12]. The realization of such devices led to a shift in the relation between theoretical and experimental condensed matter. In the past, theoretical physicists were constructing some effective, simplified models to account for the low energy properties of matter, accessible in experiments at low temperature. Such highly controllable experimental devices now allow experimental simulations of these systems. Not only these artificial quantum systems allow for the realization of exotic phases of matter – such as the ones emerging in presence of an artificial gauge field [13]– but they are able to simulate certain models in regimes that remain challenging to address theoretically, such as the Bose-Hubbard model [14] or the Fermi-gas in the regime of large scattering lengths [15]. Furthermore, these quantum simulators offer the ability to explore a vast range of yet unexplored possibilities, and in turn stimulate theoretical endeavours.

This unprecedented level of control has allowed the realization of increasingly well isolated quantum systems and led to a surge of interest in the field of out-of-equilibrium quantum physics. One of the core questions could be summarised as follows: what are the possible behaviors of isolated quantum systems as they evolve under their unitary quantum time evolution? This inquiry is relevant for the foundations of the laws of statistical physics, which are primary examples of the kind of emergent fundamental laws dear to Anderson. In the past few decades, “continuing the relentless campaign of physics to try to explain all phenomena from the Schrödinger equation” [16], efforts have been made to recover the results of statistical physics from first prin-

ciples. From our experience of everyday life, as well as from experimental results, one expects that a system being initially out of equilibrium will eventually relax toward a state of thermal equilibrium. This process is known as thermalization. Already in the early days of quantum mechanics, von Neumann put forward an apparent conflict between the Schrödinger equation and statistical physics, as the application of the Schrödinger equation does not automatically lead to thermal equilibrium [17]. The *eigenstate thermalization hypothesis* (ETH) [18, 19] is so far the most successful approach to resolve this paradox. Inspired by random matrix theory considerations, the ETH essentially states that the eigenstates of generic quantum systems behave as thermal ensemble for few body observables, explaining why local measurements agree with the predictions of statistical physics.

Nevertheless, this idea does not exclude the possibility that some quantum systems can escape such a mechanism, and therefore be able to avoid reaching thermal equilibrium. In particular, ETH does not apply to systems which possess a large number of conserved quantities, such as integrable systems [20–22] or *localized* systems. The latter were first introduced by Anderson [23], who postulated that disordered non interacting systems would not thermalize due to the localization in real space of their eigenstates. Recently, many-body localization (MBL) [24], the interacting generalization of Anderson localization, has been proposed as a more realistic exception to thermalization— as interactions are unavoidable in real systems. A lot of efforts have been dedicated to the detection of MBL in experiments, especially in artificial quantum systems. Local measurements in one dimension [25] as well as in two dimensions [26, 27], have established the presence of a non ergodic behavior signalling MBL physics.

While strong evidence suggests the existence of both the thermal phase (also called ergodic phase), satisfying ETH, and the MBL phase, displaying localization in presence of interactions, we do not have yet a full description of the *phase transition* taking place between these two states of matter. The concept of phase transition is one of the most successful unifying framework in many-body physics. It explains the abrupt changes in macroscopic behavior displayed at some particular points by some systems under the continuous change of their defining parameters, either in the Hamiltonian (interaction strength, disorder etc.), either in the external conditions (pressure, temperature etc.). In the case of continuous phase transitions, where a distinct phase exists at the critical point, a few relevant variables exhibit characteristic scaling relations, allowing for the classification of a wide range of disparate phenomena into unifying universality classes [28]. The ergodic/MBL phase transition is unusual as it happens at all energy levels, and is not simply confined to the low energy region of the spectrum. It is called a *dynamical phase transition*, since the dynamics of a quantum system is fully determined by all its eigenstates. In addition to its fundamental importance, MBL has been proposed to store and protect information in quantum devices [29, 30].

In recent years, theoretical progress has been made towards the understanding of the dynamics of out-of-equilibrium quantum systems. In particular, considerations based on random circuits [31–34], complementing the existing tools of field theory [35, 36], has allowed to identify simple behaviors at long times through the hydrodynamic picture. Nevertheless, a precise microscopic description of these systems often remains elusive. In certain cases, the current capabilities of experimental quantum simulators far exceed what is possible to predict analytically and numerically [26]. In particular, their simulation on classical computers is extremely difficult, due to the exponentially large in system size dimension of the associated Hilbert space. As

already mentioned, the tensor network formalism has allowed tremendous progress to be made in the understanding of ground state physics. As the dimension of the Hilbert space in both cases is identical, why can't we straightforwardly use this approach to simulate out-of-equilibrium quantum systems? To understand the source of the difficulty at hand, we need to introduce the concept of *quantum entanglement*, often referred to as *quantum information*, which first appeared in a thought experiment of Einstein, Podolsky and Rosen [37]. Two particles are said to be entangled if one can not be described independently of the other, a situation which does not occur in classical physics. The success of the tensor network formalism in ground state physics is due to the relatively low entanglement carried by most eigenstates at low energies, which allows to represent very efficiently the wave-function on a classical computer, using relatively few parameters compared to the full Hilbert space dimension. In contrast, out-of-equilibrium quantum physics often involves highly entangled quantum states. The large amount of "information" contained in these states prohibits a straightforward simulation using tensor network.

Nevertheless, one can wonder whether tensor networks can be pushed beyond their current limitations. For example, when the wave function cannot be obtained exactly, can we make some approximations in order to retain the correct physical behavior? Are there certain regimes where these algorithms remain usable to simulate out-of-equilibrium many-body quantum systems? Can we learn more about the ergodic/MBL phase transition using these methods? In this thesis, we shed light on these questions, as we explore the rich phenomenology of out-of-equilibrium quantum many-body systems in one dimension using tensor networks.

This thesis starts, in Chapters 2, 3 and 4, by a review of results already contained in the literature and which are necessary to the understanding of the dissertation. In Chapters 5, 6 and 7, we present our main results, some of which have already been published in Refs. [1, 2].

To begin with, in Chapter 2, we review the eigenstate thermalization hypothesis. We show how it naturally emerges as a generalization of random matrix theory (RMT) and why it implies thermalization. In Chapter 3, we introduce a primary example of exception to thermalization, many-body localization (MBL). We start by presenting its non interacting counterpart, Anderson localization, and review how the phenomenology of MBL arises from the emergence conserved quantities which are localized in real space. We also give an overview of the renormalization approaches aimed at explaining the transition between the many-body localized and thermal phases. In Chapter 4, we give a concise but nevertheless self contained review of the matrix-product state (MPS) formalism, a particular kind of tensor network theory suited for one dimensional systems. We introduce the principles underlying the algorithms used in this work, and explain the most currently used MPS algorithms, both to resolve eigenstates or to perform time evolution.

In Chapter 5, we explore the possibility of probing the propagation of quantum information in isolated systems by using various MPS methods to calculate the so called *out-of-time-order correlator*. We carefully benchmark the different approaches, and compare intermediary system sizes with state of the art exact methods to identify the limitations of each MPS calculation. We extend our MPS simulations to larger system sizes, and identify the features captured correctly by each method. In Chapter 6, we show how the simulation boundary dissipative systems allows us to estimate a particular transport coefficient, the diffusion coefficient. The method used rests on the idea that the steady states of dissipative systems can be efficiently be represented as matrix-product operators (MPO), the generalization of MPS to operators. We compare our results with various other values obtained either analytically in the integrable case, with exact

methods or with another well controlled MPS method. Finally, in Chapter 7, we demonstrate how graph theory concepts can be used to understand some properties of the MBL phase, both in the static and dynamic cases. As our graph theory approach is highly efficient, we demonstrate its applicability to states obtained through MPS calculations. We also discuss their experimental relevance.

2 Quantum thermalization: the eigenstates thermalization hypothesis

The concept of *thermalization* — the process by which a system reaches the state of equilibrium predicted by statistical physics — is central to this thesis. Although quantum thermalization was first discussed by Schrödinger [38] and von Neumann [39], a new approach emerged in the end of the 20th century [16, 18, 19, 40]. It consists in reproducing the prediction of the micro-canonical ensemble by using the microscopic degrees of freedom, i.e. the Schrödinger equation. To achieve this, the main idea is that the eigenstates of generic non integrable Hamiltonians behave as statistical ensembles as far as few body observables are concerned. A precise mathematical statement of this can be made through the *eigenstates thermalization hypothesis* (ETH), which is a generalization of random matrix theory.

2.1 Elements of random matrix theory: some properties of the Gaussian unitary ensemble

In the nineteen fifties, Wigner understood that explaining the energy spectrum of atomic nuclei was impossible from exact calculations. However, he realized that within a small enough energy window, where the density of states is constant, the energies of the nuclei would follow the same distribution as the eigenvalues of a random matrix [41–43]. By doing so, not only he was extremely successful in explaining experimental results, but he laid out the foundation of random matrix theory (RMT), a formalism which has since proven useful to explain the behavior of highly complex systems, such as in our case, quantum many-body systems described by generic non integrable Hamiltonian, also called *ergodic systems*.

2.1.1 Definition

In order to understand thermalization, we need some properties of random matrix theory (RMT). First we define the Gaussian unitary ensemble (GUE), which describe the most general probability distribution for hermitian random matrices. These random matrices will serve as a model to understand the Hamiltonian of ergodic systems. In order to obtain the properties of such an ensemble, we must impose the natural condition that the probability distribution of the matrix elements should not depend on the choice of basis. Therefore, the two following properties are enough to fully define the GUE [44]:

- 1) The invariance of the ensemble under any unitary transformation:

$$H \rightarrow U^\dagger H U \tag{2.1}$$

where $U^\dagger U = 1$.

- 2) The elements of the random matrix H_{ij} are statistically independent for $i \leq j$.

It is remarkable that such minimal assumptions are enough to derive a probability distribution for matrix elements which properties are useful to characterize a large number of physical systems. However, in order to understand the mechanism of thermalization, we need to understand the properties of the eigenstates of such random matrices.

2.1.2 The eigenstates of matrices sampled from the Gaussian unitary ensemble

In the spirit of the last section, we want to start from the definition of the GUE to derive a joint probability distribution of the components of an eigenvector of a matrix sampled from the GUE. In fact, this probability distribution will be valid only if the size of the matrix is large enough.

Let ψ be an eigenvector of a matrix sampled from the GUE. Let us choose a particular basis in which ψ has components $(\psi_1, \psi_2, \dots, \psi_N)$. We are looking for the probability distribution $P(\psi_1, \psi_2, \dots, \psi_N)$. However, due to the property 1) of the GUE, P should not depend on the choice of basis. Therefore, for any unitary transformation U , we can write [40, 45, 46]:

$$P\left(\sum_i U_{1i}\psi_i, \sum_i U_{2i}\psi_i, \dots, \sum_i U_{Ni}\psi_i\right) = P(\psi_1, \psi_2, \dots, \psi_N) = f(|\psi|). \quad (2.2)$$

In the last equality, we have used the fact that a function that is symmetric under all unitary transformations can only depend on the norm of the state. However the normalization of the state implies:

$$P(\psi_1, \psi_2, \dots, \psi_N) \propto \delta\left(1 - \sum_{i=1}^N |\psi_i|^2\right). \quad (2.3)$$

where the metric is given by $\mathcal{D}[\psi] = \prod_i^N d\text{Re}(\psi_i)d\text{Im}(\psi_i)$. That is to say that ψ should be a vector of norm one pointing in a random direction in the $2N$ -dimensional sphere. One should note that in the reasoning above we have considered that the eigenvectors of a matrix sampled from a GUE are completely independent of each other. This can not be true, since they need to be orthogonal to each other. If the Hilbert space is large enough, we can relax the orthogonality constraint, since random vectors will have a very large probability to be orthogonal to each other.

It is useful to derive the distribution of a finite number of components ψ_1, \dots, ψ_l , $l < N$. In order to do so, we need to integrate (2.3) [45, 46]:

$$P(\psi_1, \psi_2, \dots, \psi_l) \propto \int_{\psi_{l+1}, \dots, \psi_N} \mathcal{D}[\psi_{l+1}, \dots, \psi_N] \delta\left(1 - \sum_{i=1}^N |\psi_i|^2\right). \quad (2.4)$$

Keeping in mind that the integration runs over $2(N-l)$ variables (taking into accounts the real and the imaginary parts), we go to hyperspherical coordinates:

$$P(\psi_1, \psi_2, \dots, \psi_l) \propto S(2(N-l)) \int_R dR R^{2(N-l)-1} \delta\left(1 - \sum_{i=1}^l |\psi_i|^2 - R^2\right), \quad (2.5)$$

where $R^2 = \sum_{i=1}^N |\psi_i|^2$ and $S(2(N-l))$ is the surface of the $2(N-l)$ -dimensional sphere. After integration, one obtains:

$$P(\psi_1, \psi_2, \dots, \psi_l) \propto \left(1 - \sum_{i=1}^l |\psi_i|^2\right)^{(N-l-1)}. \quad (2.6)$$

We are particularly interested in the results for one and two components. Using the fact that $(1 + x/n)^n \rightarrow e^x$ when $n \rightarrow \infty$, the asymptotic value yields [45, 46]:

$$P(\psi_i)_{N \gg 1} = \frac{N}{\pi} \exp(-N|\psi_i|^2) \quad \text{and} \quad P(\psi_i, \psi_j)_{N \gg 1} = \frac{N^2}{\pi^2} \exp(-N|\psi_i|^2) \exp(-N|\psi_j|^2). \quad (2.7)$$

This property allow us to derive several relations which will be useful in section 2.2:

$$\overline{|\psi_i|^2} = \frac{N}{\pi} \int |\psi_i|^2 \exp(-N|\psi_i|^2) \mathcal{D}[\psi_i] = 2\pi \frac{N}{\pi} \int_0^\infty r^3 \exp(-Nr^2) dr = \frac{1}{N}, \quad (2.8)$$

$$\overline{\psi_i \psi_j^*} = \frac{N^2}{\pi^2} \int \psi_i \psi_j^* \exp(-N|\psi_i|^2) \exp(-N|\psi_j|^2) \mathcal{D}[\psi_i, \psi_j] = 0, \quad (2.9)$$

$$\overline{|\psi_i|^4} = \frac{N}{\pi} \int |\psi_i|^4 \exp(-N|\psi_i|^2) \mathcal{D}[\psi_i] = 2\pi \frac{N}{\pi} \int_0^\infty r^5 \exp(-Nr^2) dr = \frac{2}{N^2}. \quad (2.10)$$

Therefore we obtain the following important relation:

$$\overline{|\psi_i|^4} = 2\overline{|\psi_i|^2}^2. \quad (2.11)$$

We are now equipped to understand the average value of hermitian operators under GUE Hamiltonian. In turn, this will allow us to understand thermalization process.

2.2 The Structure of the matrix elements of hermitian operators under the Gaussian unitary ensemble

Let \hat{O} be an hermitian operator such that:

$$\hat{O} = \sum_i O_i |i\rangle \langle i|. \quad (2.12)$$

Let $|m\rangle$ and $|n\rangle$ be two eigenstates of a Hamiltonian sampled from the GUE distribution, with energies E_m and E_n . We would like to understand the behavior of the matrix elements $\langle m | \hat{O} | n \rangle = \sum_i O_i \langle m | i \rangle \langle i | n \rangle$. For this purpose, it is useful to note that because of (2.8) and (2.9):

$$\overline{\langle m | i \rangle \langle i | n \rangle} = \frac{1}{N} \delta_{mn} \delta_{ij}, \quad (2.13)$$

where N is the dimension of the Hilbert space.

Hence we find:

$$\overline{\langle m | \hat{O} | m \rangle} = \frac{1}{N} \sum_i O_i := \bar{O} \quad \text{and} \quad \overline{\langle m | \hat{O} | n \rangle} = 0 \quad \text{for } m \neq n. \quad (2.14)$$

The fluctuations of the diagonal elements are the following:

$$\overline{\langle m|\hat{O}|m\rangle^2} - \overline{\langle m|\hat{O}|m\rangle}^2 = \sum_i O_i^2 \left(\overline{|\langle m|i\rangle|^4} - \overline{|\langle m|i\rangle|^2}^2 \right) = \frac{1}{N^2} \sum_i O_i^2 = \frac{1}{N} \overline{O^2}, \quad (2.15)$$

where we have used (2.11) and (2.13).

Furthermore, for the variance of the off-diagonal correlations, one finds:

$$\overline{|\langle m|\hat{O}|n\rangle|^2} - \overline{|\langle m|\hat{O}|n\rangle|}^2 = \overline{|\langle m|\hat{O}|n\rangle|^2} = \frac{1}{N} \overline{O^2}, \quad (2.16)$$

where we made use of the (approximate) independence of the eigenvectors and equation (2.8).

Therefore, to the leading order in the inverse of the Hilbert space dimension, if we write the elements of \hat{O} as [40]:

$$\langle m|\hat{O}|n\rangle = \overline{O} \delta_{mn} + \sqrt{\frac{\overline{O^2}}{N}} R_{mn} \quad (2.17)$$

with R_{mn} a random variable with zero mean and unit variance, then \hat{O} has the correct mean and variances calculated in equations (2.14), (2.15) and (2.16).

2.3 The eigenstate thermalization hypothesis

2.3.1 Thermalization in closed quantum system

Let us consider a quantum isolated system described by a Hamiltonian. We prepare a state $|\psi\rangle$ with total energy E . We can write the decomposition of $|\psi\rangle$ in the eigenbasis:

$$|\psi\rangle = \sum_i \psi_i |i\rangle. \quad (2.18)$$

We now consider an observable \hat{O} . It's expectation value will evolve in time according to:

$$\langle \hat{O} \rangle(t) = \sum_i |\psi_i|^2 O_i + \sum_{i,j,i \neq j} \psi_i \psi_j^* e^{i(E_j - E_i)t} \langle i|\hat{O}|j\rangle. \quad (2.19)$$

An observable is said to thermalize if after a time called the Thouless time t_{Th} , it's expectation value relaxes toward the value predicted by the microcanonical statistical ensemble [16]:

$$\langle \hat{O} \rangle_{\text{micro}, E} = \frac{1}{W} \sum_{E_m \in [E + \delta_E]} \langle m|\hat{O}|m\rangle, \quad (2.20)$$

where W is the number of energy levels between E and $E + \delta_E$.

2.3.2 From random matrix theory to thermalization

At first sight, it is not straightforward to see how to reconcile equations (2.19) and (2.20). However, following the original insight of J.M. Deutsch presented into his seminal paper [18], let us suppose that the Hamiltonian is a random matrix following GUE. We now from Sec. 2.2 that the fluctuation of the diagonal elements of \hat{O} will be suppressed in system size (see Eq. (2.15)). Using (2.14), we can write:

$$\sum_i |\psi_i|^2 O_i = \bar{O} \sum_i |\psi_i|^2 = \bar{O}. \quad (2.21)$$

Therefore the late times expectation value do not depend on the initial state. Furthermore, since the off-diagonal elements are suppressed exponentially in system size, the second term of the sum (2.19) will not need an exponentially long time in system size to vanish.

However, this approach is not completely satisfying, since in practice both the thermalization time and the thermal value of the operator depend on the temperature and are operator dependent. Predictions of random matrix theory cannot account for these facts since the microcanonical average always correspond to infinite temperature average. Indeed, unlike in physical Hamiltonians, the properties of eigenstate $|m\rangle$ do not depend on the position of its energy E_m in the spectrum. The next section will introduce the eigenstate thermalization hypothesis (ETH) to overcome this shortcoming.

2.3.3 The eigenstate thermalization hypothesis (ETH)

The ETH has been introduced by M. Srednicki [19], and can be seen as energy dependent version of equation (2.17):

$$\langle i|\hat{O}|j\rangle = g_O \left(\frac{E_i + E_j}{2} \right) + \exp \left(-\frac{S \left(\frac{E_i + E_j}{2} \right)}{2} \right) f_O \left(\frac{E_i + E_j}{2}, E_i - E_j \right) R_{mn}, \quad (2.22)$$

where $S(E)$ is the statistical entropy at energy E , f_O and g_O are smooth functions of their argument—they depend on the operator \hat{O} and $g_O(E)$ must be equal to the microcanonical ensemble average at energy E —and R_{mn} is a random variable such that $\overline{R_{mn}} = 0$ and $\overline{|R_{mn}|^2} = 0$.

First, this ansatz explains the phenomena of thermalization for initial states which are "peaked" in energy i.e. which overlap only with eigenstates which are close together in the spectrum. This restriction does not need to concern us since most initial states of interest will have this property. First, states sampled from a statistical ensemble will be peaked in energy, as well as states with short range correlations (if the Hamiltonian is local).

To see why ETH explains thermalization, let us consider the following:

$$\lim_{t \rightarrow \infty} \frac{1}{t} \int_{t_0}^t \langle \hat{O} \rangle(t') dt' = \sum_m |\psi_m|^2 \langle m|\hat{O}|m\rangle + \lim_{t \rightarrow \infty} \frac{1}{t} \int_{t_0}^t dt' \sum_{i,j,i \neq j} \psi_i \psi_j^* e^{i(E_j - E_i)t'} \langle i|\hat{O}|j\rangle. \quad (2.23)$$

The second term vanishes and we are left in the same situation than in Eq. (2.21). Indeed, the ETH guarantees that within a small energy window the diagonal elements of the operator do not

change much. That is to say that within this window, the ETH reduces to RMT. Therefore we can apply the same reasoning as before and write:

$$\lim_{t \rightarrow \infty} \frac{1}{t} \int_{t_0}^t \langle \hat{O} \rangle(t') dt' \approx g_O(E) \sum_m |\psi_m|^2 = \langle O \rangle_{E, \text{micro}}, \quad (2.24)$$

where E is as before the energy of the initial state $|\psi(t=0)\rangle$.

We can look at the following fluctuations:

$$\begin{aligned} \sigma_O^2 &= \lim_{t \rightarrow \infty} \frac{1}{t} \int_0^t dt \langle \hat{O}(t)^2 \rangle - \langle O \rangle_{E, \text{micro}}^2 \\ &= \lim_{t \rightarrow \infty} \frac{1}{t} \int_0^t dt \sum_{i,j,k,l} \psi_i \psi_j^* \psi_k \psi_l^* \exp(i(E_j - E_i + E_k - E_l)t) - \langle O \rangle_{E, \text{micro}}^2 \\ &= 2 \sum_{n,m,m \neq n} |\psi_n|^2 |\psi_m|^2 |\langle n | \hat{O} | m \rangle|^2 \leq 2 \max |\langle n | \hat{O} | m \rangle|^2 \sum_{n,m,m \neq n} |c_n|^2 |c_m|^2 \\ &= 2 \max |\langle n | \hat{O} | m \rangle|^2 \propto \exp(-S(E)). \end{aligned} \quad (2.25)$$

Therefore, at almost every time the expectation value of the operator \hat{O} is the same as the one given by the canonical ensemble.

Of course, due to ensemble equivalence, all the results above can be extended to the canonical ensemble.

2.4 Entanglement of the states of ergodic Hamiltonians

We have seen in the previous section that the ETH is a generalization of an intuition derived from RMT. Therefore it is natural to expect the eigenstates of ergodic Hamiltonian to be similar to random states and therefore highly entangled. Indeed, a subsystem of size n embedded of a random system of size N , with local Hilbert space dimension d , has for entanglement entropy the so called ‘‘Page value’’ [47], if $1 \ll d^n \leq d^{(N-n)}$, given by:

$$S_{\text{page}} = n \ln(d) - \frac{1}{2} d^{n-N}. \quad (2.26)$$

One can confirm this intuition by the following reasoning: if one split the system into two parts A and B , B being much larger than A , then the reduced density of eigenstate i for the subsystem A should be the thermal density matrix at temperature T :

$$\rho_A^\alpha = \frac{1}{Z} \exp\left(-\frac{H}{k_B T}\right), \quad (2.27)$$

since all local operators would reach the expectation value of the canonical ensemble at temperature T , with $\frac{1}{T} = \frac{dS}{dE}$. The entanglement of such a density matrix is proportional to the area of system A . First let us look at the infinite temperature matrix $\rho_\infty = \frac{1}{\mathcal{D}} \hat{I}$, where \mathcal{D} is the Hilbert space dimension. The entanglement entropy associated with this density matrix is given by $S_\infty = \ln(\mathcal{D}) = V \ln(d)$, where V is the volume. This idea can be generalized to other temperatures as well. Indeed, since the subsystem is described by the canonical ensemble, the entanglement entropy is equal to the physical entropy, which is an extensive quantity.

3 Localized systems

In his original paper [23], Anderson noted that an *Anderson insulator* was a system where “the approach to equilibrium is simply not possible”. However, in order to find a robust non integrable exception to thermalization, one needs to make sure that localization is in some sense stable against the addition of interactions, since they are hardly avoidable in real systems. Such a phenomenon is called many-body localization (MBL).

In this chapter, we start by briefly reviewing Anderson localization in one dimension before describing some of the key phenomenological aspects of MBL and the theoretical models aimed at explaining them.

3.1 Anderson localization

3.1.1 Localization length: the Thouless formula

We consider the following one-dimensional tight binding model:

$$\hat{H} = \sum_i -t(|i\rangle\langle i+1| + |i+1\rangle\langle i|) + \mu_i|i\rangle\langle i| \quad (3.1)$$

where t is the hopping term and μ_i are random onsite chemical potential drawn from a uniform disorder distribution: $h_i \in [-W, W]$. We will consider $t = 1$ in what follows. This model was conjectured to be localized for any amount of disorder by Mott and Twose in Ref. [48]. This means that the wave functions $\psi(x)$ obeys the following relationship:

$$\psi(x) \propto e^{-x/\xi}, \quad (3.2)$$

where ξ is the localization length. A mathematical proof of this assertion [49] was given first in a related model in Ref. [50] and in the actual model above in Ref. [51].

We are now going to derive a relation between the density of states and the localization length –originally found by Thouless [52]– for Dirichlet (open) boundary conditions. More precisely we will consider the problem for N -sites with boundary conditions $\psi_0^N = \psi_{N+1}^N = 0$. We denote the eigenvalues of this problem $\{E_i^N, i \in [1, N]\}$. The eigenvectors have components $(\psi_1^N(E), \dots, \psi_N^N(E))$ where $E \in [E_1, \dots, E_N]$, with initial conditions $\psi_1^N = 1$. We are then going to add one more site (the new boundary condition is now $\psi_{N+2}^{N+1} = 0$) and express $\psi_{N+1}^{N+1}(E)$ as a function of the E_i^N 's. As we are going to show, the eigenvectors can be expressed as a function of the eigenenergies, and their expression does not depends on system size. However, the energies themselves are system size dependant. We will therefore drop the upper index of the

eigenvectors from now on.

The components $\psi_n(E)$ of the eigenvectors $\psi(E)$ are related by the following recursive formula:

$$\psi_{n+1}(E) = (\mu_n - E)\psi_n(E) - \psi_{n-1}(E). \quad (3.3)$$

Let us solve first the problem for one site. We obtain $E_1^1 = \mu_n$. For two sites the problem reduces to

$$\psi_2(E) = (\mu_1 - E)\psi_1(E) = (E_1^1 - E). \quad (3.4)$$

At this point, we have found an expression for the eigenvectors (ψ_1, ψ_2) as a function of E , but we do not know yet what values the energy is allowed to take. Note that we have not used the boundary conditions yet, so the above relationship remains valid independently of system size: as mentioned above, the expression of the components of the eigenvectors as function of the energy do not depend on system size. The eigenenergies are to be found by considering equation (3.3) at the last site of the chain. Indeed, we need to solve

$$(\mu_3 - E)\psi_2 - \psi_1 = (\mu_3 - E)(E_1^1 - E) - 1 = 0. \quad (3.5)$$

The energies of the system satisfy the above equation. The energies E_1^2 and E_2^2 are therefore the roots of this polynomial of degree 2. We can carry on recursively this procedure until we arrive to site N . The procedure is always the same: the eigenenergies are entirely determined by the solution of the equation (3.3) at the last site of the system. The first $N - 1$ components of the eigenvectors will be given by:

$$\psi_n(E) = C_n \prod_{\alpha=1}^{n-1} (E_\alpha^{n-1} - E), \quad (3.6)$$

where C_n is an overall factorization constant. Using once again (3.3) at site N (and setting $\psi_{N+1} = 0$), we obtain a polynomial of degree N which roots are the energies of the system of length N :

$$(\mu_N - E)\psi_N(E) - \psi_{N-1}(E) = C_N(\mu_N - E) \prod_{\alpha=1}^{N-1} (E_\alpha^{N-1} - E) - C_{N-1} \prod_{\alpha=1}^{N-2} (E_\alpha^{N-2} - E) = 0. \quad (3.7)$$

Now we add one more site to the system. The ψ_{N+1} components of the eigenvectors is no longer zero, and the equation (3.3) now reads:

$$\begin{aligned} \psi_{N+1}(E) &= (\mu_N - E)\psi_N(E) - \psi_{N-1}(E) \\ &= C_N(\mu_N - E) \prod_{\alpha=1}^{N-1} (E_\alpha^{N-1} - E) - C_{N-1} \prod_{\alpha=1}^{N-2} (E_\alpha^{N-2} - E) = 0. \end{aligned} \quad (3.8)$$

Since the roots of the polynomial of degree N in the equation above are simply the eigenenergies of the system of size N , we can write :

$$\psi_{N+1}(E) = C_{N+1} \prod_{\alpha=1}^N (E_\alpha^N - E). \quad (3.9)$$

We are now ready to express the localization length:

$$\frac{-1}{\xi(E)} = \lim_{N \rightarrow \infty} \frac{1}{N} \ln(\psi_{N+1}(E)) = \lim_{N \rightarrow \infty} \frac{1}{N} \sum_{\alpha=1}^N \ln(|E_\alpha - E|) = \int_{E'} \rho(E') \ln(|E' - E|), \quad (3.10)$$

where $\rho(E) = \lim_{N \rightarrow \infty} \sum_{\alpha=1}^N \delta(E_\alpha - E)$. Equation (3.10) is called the Thouless formula [52], and is extremely useful to detect localization in one dimensional systems.

3.1.2 Disordered spinless fermions in second quantization and the Jordan-Wigner transformation

In one dimension, the Anderson localization Hamiltonian expressed in second quantization reads:

$$\hat{H} = \sum_i \left(\hat{a}_i^\dagger \hat{a}_{i+1} + \hat{a}_{i+1}^\dagger \hat{a}_i + h_i \hat{n}_i \right), \quad (3.11)$$

where a_i^\dagger , a_i are the fermionic creation and destruction operators, and $\hat{n}_i = \hat{a}_i^\dagger \hat{a}_i$. However, for numerical simulations, it is convenient to map this free fermion model to a spin model. To this aim one uses the *Jordan-Wigner transformation* [53]:

$$\hat{a}_i = \left(\prod_{k \langle i} \hat{\sigma}_k^z \right) \hat{\sigma}_i^+, \quad (3.12)$$

$$\hat{a}_i^\dagger = \left(\prod_{k \langle i} \hat{\sigma}_k^z \right) \hat{\sigma}_i^-, \quad (3.13)$$

$$\hat{n}_i = \frac{1}{2} \left(\hat{I} - \hat{\sigma}_i^z \right). \quad (3.14)$$

Applying this transformation to the Hamiltonian (3.11), one obtain, up to an irrelevant constant, the XX model:

$$\hat{H} = \sum_i \left(\hat{\sigma}_i^x \hat{\sigma}_{i+1}^x + \hat{\sigma}_i^y \hat{\sigma}_{i+1}^y + \frac{h_i}{2} \hat{\sigma}_i^z \right). \quad (3.15)$$

3.2 Many-body localization

Many-body localization is the interacting generalization of the Anderson localized model. It was first proposed by Basko, Aleiner and Altshuler [24]. They considered the effect of a weak interaction in disordered fermions in the regime where all single particle eigenstates are localized. They found that the wave-function is localized in Fock space for sufficiently low temperature. These findings, based on analytical considerations, were later supported by numerics performed by Oganesyan and Huse [54]. They investigated a disordered next nearest neighbor fermionic chain and considered the spectral statistics of adjacent energy levels. The intuition behind the choice of this quantity is that nearby energy levels are expected to be far apart in Fock space (due to Fock space localization) and the spectrum should not display level repulsion, leading to

a Poisson statistics. This study indicated the existence of an ergodic-MBL transition at finite temperature. A very commonly studied model for MBL is the disordered XXZ spin-chain [55]:

$$\hat{H} = \sum_i \left(\hat{\sigma}_i^x \hat{\sigma}_{i+1}^x + \hat{\sigma}_i^y \hat{\sigma}_{i+1}^y + \Delta \hat{\sigma}_i^z \hat{\sigma}_{i+1}^z + \frac{h_i}{2} \sigma_i^z \right), \quad (3.16)$$

which can be mapped using the Jordan-Wigner transformation to:

$$\hat{H} = \sum_i \left[\hat{a}_i^\dagger \hat{a}_{i+1} + \hat{a}_{i+1}^\dagger \hat{a}_i + h_i \hat{n}_i + \Delta \left(\hat{n}_i - \frac{1}{2} \right) \left(\hat{n}_{i+1} - \frac{1}{2} \right) \right]. \quad (3.17)$$

Note that Eq. (3.17) is nothing but the Hamiltonian of Eq. (3.11) with an additional interaction term.

3.2.1 Local integrals of motions

Many-body localization (MBL) is understood in terms of local integrals of motion (LIOMs), proposed for the first time in Ref. [56]. We start from the following hypothesis: applying local perturbations to an MBL system only gives rise to local modifications of the eigenstates. That is to say that the degrees of freedom located at a distance much larger than the many-body localisation length ξ of the perturbation are only affected by it exponentially weakly. Let us divide the system into a number of subsystems. In the first formulation of the LIOMs, the size of the subsystems was taken to be much larger than the localization length ξ . However, we are going to see that the reasoning remains valid even if one takes every subsystem to be only one site. For every subsystem i , one can decompose the Hamiltonian as:

$$H = H_{L_i} + H_{R_i} + H_i + J_{int}(H_{R_i} + H_{L_i}) \quad (3.18)$$

where the terms H_{R_i} and H_{L_i} represent the interaction between site i and the left and right part of the system respectively. The eigenvalues of H_i are labeled by an index β . Without interaction ($J_{int} = 0$), the eigenstates are simple product states of the eigenstates of the local operators: $|\alpha\rangle_{L_i} |\beta\rangle_i |\gamma\rangle_{R_i}$. With interactions, the eigenstates $|\alpha_i, \beta_i, \gamma_i\rangle$ are given by:

$$|\alpha_i, \beta_i, \gamma_i\rangle = \hat{U}_{L_i} \hat{U}_{R_i} |\alpha\rangle_{L_i} |\beta\rangle_i |\gamma\rangle_{R_i} \quad (3.19)$$

where \hat{U}_{L_i} and \hat{U}_{R_i} are unitary rotations which only act on the degrees of freedom located at a distance smaller than ξ from subsystem i .

The LIOM associated with subsystem i is defined as [56]:

$$\hat{I}_i = \sum_{\beta} \beta \sum_{\alpha_i} \sum_{\gamma_i} |\alpha_i, \beta_i, \gamma_i\rangle \langle \alpha_i, \beta_i, \gamma_i| = \sum_{\beta} \beta P_{\beta}^i, \quad (3.20)$$

where P_{β}^i is the projector on the state $|\alpha\beta\gamma\rangle_i$, which is an eigenstate of \hat{I}_i with eigenvalue β . The integrals of motions have important properties:

- 1) Since it is a linear combination of projectors on eigenstates, I_i commutes with the Hamiltonian.

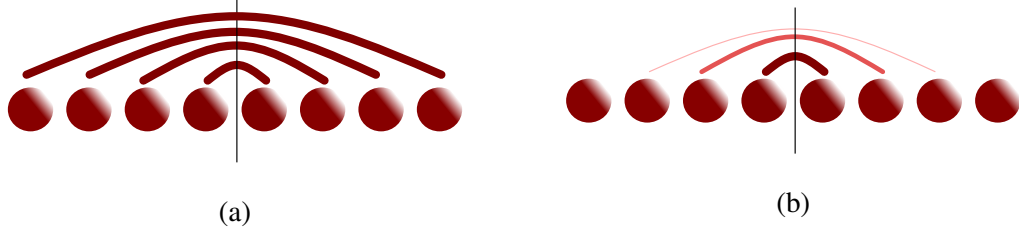


Figure 3.1 Ergodic eigenstates in the middle of the spectrum are highly entangled as they follow volume law (panel a), while all eigenstates of MBL Hamiltonian follow area law (panel b).

- 2) Because of the locality of \hat{U}_{L_i} and \hat{U}_{R_i} , the sum of projectors becomes close to the identity at a distance greater than ξ from site i .
- 3) The eigenvalue only depends on β . Therefore, the eigenstates are highly degenerate. Roughly, eigenstates with the same eigenvalue β are nearly identical at distance larger than ξ from subsystem i .
- 4) If the same construction is carried out for all subsystems i , the eigenvalues of the integral of motions completely characterize the eigenstates of the Hamiltonian, since every state is characterized locally around subsystem i by I_i .

Since all the eigenstates of the Hamiltonian can be labeled by their eigenvalues with respect to the integral of motions, the Hamiltonian can be written as a sum over the projectors P_β^i [56]:

$$H = \sum_{i=1}^N \sum_{\beta} E_{\beta}^i P_{\beta}^i + \sum_{i \neq j} \sum_{\beta, \beta'} E_{\beta, \beta'}^{i,j} P_{\beta}^i P_{\beta'}^j + \sum_{i < j < k} \sum_{\beta, \beta', \beta''} E_{\beta, \beta', \beta''}^{i,j,k} P_{\beta}^i P_{\beta'}^j P_{\beta''}^k \dots \quad (3.21)$$

Roughly, E_{β}^i can be seen as the energy associated with eigenvalue β of I_i at site i , while $E_{\beta, \beta'}^{i,j}$ quantify the interaction between sites i and j . Due to the initial assumption about the local effects of any perturbation (here the coupling with the left and the right), we expect that the interactions between sites i and j are exponentially suppressed in the distance $|i - j|$.

The locality of \hat{U}_{L_i} and \hat{U}_{R_i} has also a far reaching consequence for the structure of the state. Let us consider a cut at the right end of subsystem i . The correlations between the two parts hence generated can only come from the vicinity of subsystem i . As this is valid for any cut considered in the chain, the bipartite entanglement must be on average constant, provided that it is measured sufficiently far from the boundaries [57]. The entanglement is then said to follow *area law* [58], meaning that the entanglement between two parts of the system is proportional to the area of the cut separating the two parts, as illustrated on Fig. 3.1.

3.2.2 Spin one-half case: the l-bits

We now focus on the spin- $\frac{1}{2}$ case, where the LIOMs take a particular elegant form [59]. We show how to arrive to integrals of motions by a different route. For concreteness, let us start from the following diagonal Hamiltonian:

$$\hat{H}_{\text{diag}} = \frac{J}{2} \sum_i \hat{\sigma}_i^z \hat{\sigma}_{i+1}^z + \sum_i h_i \hat{\sigma}_i^z, \quad (3.22)$$

where $h_i \in [-W, W]$. The eigenstates are the product states in the σ^z -basis. Now let us introduce non diagonal terms in this Hamiltonian: $\hat{H} = \hat{H}_{\text{diag}} + \frac{J_x}{2} (\hat{\sigma}_i^x \hat{\sigma}_{i+1}^x + \hat{\sigma}_i^y \hat{\sigma}_{i+1}^y)$. There exists a unitary U such that:

$$U \hat{H} U^\dagger = \hat{H}_{\text{diag}} \quad (3.23)$$

Since the $\hat{\sigma}^z$ operators commute with H , rotating them with the same unitary transformation will yield the integral of motions $\hat{\tau}^z$ of \hat{H} :

$$\hat{\tau}_i^z = U \hat{\sigma}_i^z U^\dagger \quad (3.24)$$

These integral of motions correspond to the operators \hat{I}_i derived in the previous section, where the subsystems in which the chain is divided are simply the individual sites. Indeed, one can label the states of the previous section $\beta = \pm 1$ such that $\hat{\tau}^z |\beta\rangle = \pm 1 |\beta\rangle$. Then the integral of motions take the familiar form:

$$\hat{\tau}_i^z = \sum_{\alpha_i, \gamma_i} |\alpha_i, \beta_i = +1, \gamma_i\rangle \langle \alpha_i, \beta_i = +1, \gamma_i| - |\alpha_i, \beta_i = -1, \gamma_i\rangle \langle \alpha_i, \beta_i = -1, \gamma_i| \quad (3.25)$$

In the same way, we can define $\hat{\tau}_i^{x,y} = \hat{U} \hat{\sigma}_i^{x,y} \hat{U}^\dagger$. This set of $\hat{\tau}$ matrices constitutes a complete operator basis. Therefore the $\hat{\tau}^\alpha$ are simply the Pauli matrices in the basis which diagonalizes the Hamiltonian. The LIOMs act on effective spins which are denoted *localized-bits* (abbreviated *l-bits*) in opposition to the physical spins called *p-bits* [59]. Although such a transformation could be in principle performed on any Hamiltonian, the unitary \hat{U} is very special. Indeed, the couplings it generates between degrees of freedom are exponentially suppressed with distance. Therefore, it is said that \hat{U} is a *quasi-local* unitary transformation. It follows that the τ matrices are themselves quasi local operators [57]:

$$\hat{\tau}_i^z = V_i^{(0)} \hat{\sigma}_i^z + \sum_{n=1}^{\infty} V_i^{(n)} \hat{O}_i^{(n)}, \quad (3.26)$$

where $O_i^{(n)}$ has an operator support of $2n + 1$ sites and $V_i^{(n)}$ decays exponentially according to [57]:

$$V_i^{(n)} \sim e^{-\frac{n}{\xi}}, \quad (3.27)$$

where ξ is the MBL localization length. Since the Hamiltonian commutes with all the τ^z matrices, it can be written as:

$$\hat{H}_{\text{int}} = \sum_i \tilde{h}_i \hat{\tau}_i^z + \sum_{i<j} J_{ij} \hat{\tau}_i^z \hat{\tau}_j^z + \sum_{i<j<k} J_{ijk} \hat{\tau}_i^z \hat{\tau}_j^z \hat{\tau}_k^z + \dots \quad (3.28)$$

where one have added any required overall energy constant to make the Hamiltonian traceless. Up to this constant, this is exactly the form we obtained previously in Eq. 3.21. Indeed, any traceless

diagonal Hamiltonian can be written as a sum of $\hat{\sigma}^z$ Pauli strings. Because of the locality of the transformation, we expect the interactions between the l-bits to decay exponentially [57]:

$$J_{ij\dots k} = J_0 \exp(-|i - k|/\kappa) \quad (3.29)$$

where κ is the length-scale quantifying this decay.

In ref. [60], the existence of the LIOMs has been proven under the assumption that there is no level attraction. Note that this assumption is very natural, since random matrix usually display level repulsion in the case of GUE statistics or neither repulsion nor attraction in the case of poisson statistics.

3.2.3 Dynamical behavior of many-body localized systems

It has been shown numerically [61, 62] that the bipartite von Neumann entanglement entropy grows logarithmically when starting from a product state in the p-bit basis. One can explain this observation using the l-bits picture, by a mechanism called *dephasing* [57, 63, 64]. First, we write the initial state in the l-bits basis.

$$|\psi(t=0)\rangle = \sum_i A_i |\tau_{1,i}^z \dots \tau_{k,i}^z \dots \tau_{N,i}^z\rangle \quad (3.30)$$

The time evolution will add a phase to each of these terms:

$$\begin{aligned} |\psi(t)\rangle &= e^{iH_{\text{int}}t} |\psi(t=0)\rangle \\ &= \sum_i A_i \exp\left(-i\tilde{h}_i \hat{\tau}_{1,i}^z t - i \sum_{i<j} J_{ij} \hat{\tau}_{1,i}^z \hat{\tau}_{2,i}^z t - i \sum_{i<j<k} J_{ijk} \hat{\tau}_{1,i}^z \hat{\tau}_{2,i}^z \hat{\tau}_{3,i}^z t + \dots\right) |\tau_{1,i}^z \dots \tau_{k,i}^z \dots \tau_{N,i}^z\rangle \end{aligned} \quad (3.31)$$

Because of this phase, entanglement is generated. In order to see how this phase leads to the logarithmic growth, it is convenient to consider the effective magnetic field $\hat{h}_{i,i+x}$ [57] felt by spin located between sites i and $i+x$:

$$\hat{h}_{i,i+x} = J_{i,i+x} + J_{i,i+1} \hat{\tau}_{i+1}^z + \dots \quad (3.32)$$

Because all the couplings are proportional to $J_0 \exp(-|i - k|/\kappa)$, $\hat{h}_{i,i+x} \sim J_0 \exp(-x/\xi')$, where ξ' is yet another lengthscale. Spins i and $i+1$ become entangled when the phase of spin i dependent on spin $i+1$ is of order one [63]. This reasoning yields the following results:

$$J_0 \exp(-x/\xi') \sim 1 \implies x_{\text{ent}}(t) \sim \xi' \log(J_0 t) \implies S(t) \propto \xi' \log(J_0 t), \quad (3.33)$$

where x_{ent} is the length of the entangled portion of chain, and where we have used the fact that the entanglement of the system is related to the length of the entangled region within the system.

3.2.4 Strong randomness renormalization group approaches to many-body localization

In this section, we review the application of a particular type of renormalization group (RG) which has been the main theoretical approach to describe the ergodic/MBL transition: the strong

randomness RG. We start by quickly introducing the key ideas of this approach by giving an example for ground state physics in a disordered spin chain. We discuss how to generalize this method in order to target highly excited eigenstates of MBL Hamiltonians. Finally, we review the conclusions of this approach regarding the nature of the ergodic/MBL phase transition.

Introduction to strong randomness renormalization group: the Dasgupta-Ma approach to obtain the ground state

In 1980, Dasgupta and Ma introduced the first scheme of strong randomness RG [65]. This approach rests on the assumption that the disorder play a key role in the physics of the system, being dominant over thermal or quantum fluctuations [66]. The Hamiltonian considered is [65]:

$$H = \sum_r K_r \mathbf{S}_r \cdot \mathbf{S}_{r+1} \quad (3.34)$$

where $\mathbf{S} = (S^x, S^y, S^z)$ is the spin operator and K_r are randomly distributed according to $P(K)$, $0 < K < J$, where J is said to be the renormalization group (RG) *cutoff*. The idea of the renormalization group is to decimate the spin variable while transforming the distribution $P(K)$.

The RG scheme starts with spins \mathbf{S}_i and \mathbf{S}_{i+1} satisfying $K = J$. Consider

$$H_0 = J \mathbf{S}_i \cdot \mathbf{S}_{i+1}. \quad (3.35)$$

The ground state of this Hamiltonian is a singlet $|s\rangle$ while the excited states are triplets $|t\rangle$. Now we add left and right neighbors \mathbf{S}_{i-1} and \mathbf{S}_{i+1} , and consider the perturbation:

$$V = K_{i-1} \mathbf{S}_{i-1} \cdot \mathbf{S}_i + K_{i+1} \mathbf{S}_i \cdot \mathbf{S}_{i+1} \quad (3.36)$$

The new ground state can be obtained through second order perturbation theory [65]:

$$E = E_s + \langle s|V|s\rangle + \sum_t \frac{|\langle t|V|s\rangle|^2}{E_s - E_t} := E' + K' \mathbf{S}_{i-1} \cdot \mathbf{S}_{i+1} \quad (3.37)$$

It is then possible to express the new distribution $P(K, J - dJ)$ of the couplings K as a function when the cut-off J is decreased by dJ . Noticing that the fraction of the spin eliminated is given by $2dJP(J, J)$, the new probability distribution has to be normalized by $1 - 2dJP(J, J)$:

$$P(K, J - dJ) = \frac{dJ \left(\int_0^J dK_1 dK_2 P(K_1, J) P(K_2, J) [\delta(K - K') - \delta(K - K_1) - \delta(K - K_2)] \right)}{1 - 2dJP(J, J)} + \frac{P(K, J)}{1 - 2dJP(J, J)} \quad (3.38)$$

Real space renormalization group excited

In order to describe MBL, Pekker et al. introduced in [67] what they call the real space renormalization group excited (RSRG-X), which is a generalization of the scheme of Dasgupta-Ma for excited states. At each decimation step, instead of perturbatively finding the ground state, they have the choice either to select the low energy or high energy manifold, which are separated by a large gap controlling the perturbation theory, so that any excited state can be reached throughout the procedure.

As pointed out in Ref. [57], this procedure is another way to arrive to the 1-bit picture. Indeed, the decimation groups spin together into an effective spin which is actually the 1-bit. When selecting the low or high energy manifold, the algorithm actually assigns a value $\tau_i^z = \pm 1$ to the 1-bit.

Phenomenological strong randomness renormalization group approaches and quantum avalanches

This kind of RG approaches focuses on the effect of rare thermal (or conducting) region on an otherwise localized system, and usually involve a scenario called the *quantum avalanche* [68–70]. Let us first consider a thermal bath weakly coupled to an isolated spin. Provided that the coupling is strong enough, the bath will thermalize the spin, and the resulting system will be well described by a random matrix. Now suppose that we take an MBL system and that we extend it until we reach the thermodynamic limit. In the process, some rare thermal region will appear, which will thermalize the neighboring spins, creating a larger thermal region, which could in principle thermalize the whole chain [70]. This reasoning, which is the essence of the quantum avalanche scenario, seems to lead us to conclude that MBL can not be stable against the addition of small thermal grains.

Nevertheless, another mechanism counterbalances the quantum avalanche and ensures the stability of MBL in one dimension. Let us divide the system into localized (or insulating) regions and thermal (or conducting) regions which act as a bath. A thermal region needs to be large enough in order to thermalize an insulating one. Indeed, the coupling of the bath to an insulator can be seen as a perturbation. If the scale of this perturbation is smaller than the level spacing of the bath, then the coupled eigenstates can be obtained from perturbation theory and there is no thermalization. Conversely, if the perturbation is much bigger than the level spacing, perturbation theory is no longer valid. The energy levels hence hybridize, and the full system becomes ergodic [70]. As the many-body level spacing becomes exponentially small with system size, this explains why a bath needs to be large enough to thermalize an insulator. This can be also obtained from the Fermi golden rule [71], and has been confirmed numerically [72]. The interplay between these two effects are the subject of the type of phenomenological RG schemes developed in recent years to explain the ergodic/MBL phase transition [68, 73–77].

The assumptions we presented above – that the system is composed of multiple thermal and insulating regions (or “blocks”) – is at the heart of these RG approaches. The RG schemes are usually governed by two variables [78]: the typical localization length ζ , and the fraction f of the system which is thermal. In general, most of the RG schemes rest on two mechanisms: first the inclusion of thermal blocks in insulating blocks causes the localization length to increase; second, when the localization length is above a certain threshold, the critical localization length ζ_c , the system becomes thermal, a process referred to as “quantum avalanche”.

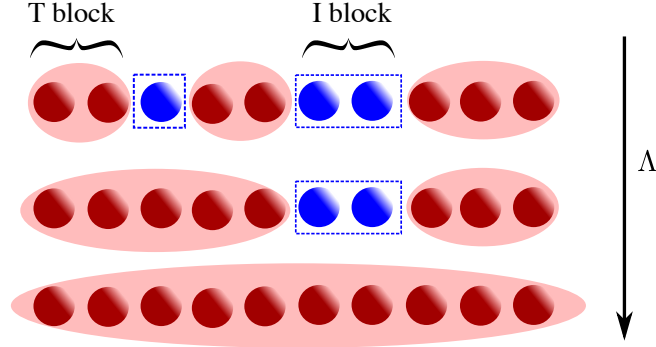


Figure 3.2 Schematic representation of the strong randomness RG scheme applied on MBL state close to the transition. During the first step, where $\Lambda = 1$, the smallest I block is thermalized by two larger T blocks. At the second step ($\Lambda = 2$) the only remaining I block is thermalized as well. At the end of the procedure, one obtain a fully thermal state.

These mechanisms give rise to RG flow equations of the form:

$$\frac{d\zeta^{-1}}{dl} = -c f \zeta^{-1} + \dots \quad (3.39)$$

$$\frac{df}{dl} = b f (\zeta - \zeta_c). \quad (3.40)$$

These equations correspond to the RG flow of the Kosterlitz-Thouless (KT) transition [79]. As KT transition are known to exhibit logarithmic corrections to finite size scaling, this scenario would naturally explain the slow convergence of finite-size numerical studies [69].

Let us now turn to the “microscopic” details of the RG which lead to this type of behavior. During the decimation procedure, instead of considering the strength of the bonds as cut-offs as in the Dagupta-Ma calculation, these approaches define a cut-off $\Lambda = \min_n l_n$, with l_n being the length of block n . The RG rules can be prescribed as follow [71, 74]: find the smallest remaining block of length Λ . Then decimate this block: if it is an insulating block surrounded by two thermal block then it becomes an insulating block (“TIT \rightarrow T”). Otherwise, if it is a thermal block surrounded by two insulating blocks, then it becomes insulating (“ITI \rightarrow I”). Of course, during this process, the properties of the newly created blocks need to be updated correctly. For example, in Ref. [74], the length of the block were added at each merger, leading to a complete symmetry between the “ITI” and the “TIT” moves:

$$\begin{aligned} l_{\text{new}}^I &= l_{n-1}^I + l_n^T + l_{n+1}^I \\ l_{\text{new}}^T &= l_{n-1}^T + l_n^I + l_{n+1}^T \end{aligned} \quad (3.41)$$

where l_{new}^I (resp. l_{new}^T) are the newly created blocks coming from the merger of blocks $l_{n-1}^I, l_n^T, l_{n+1}^I$ (resp. $l_{n-1}^T, l_n^I, l_{n+1}^T$). It turns out that this is an oversimplification [75], which does not lead to the expected RG scaling. However, equation (3.41) can be straightforwardly corrected [75]:

$$\begin{aligned} l_{\text{new}}^I &= l_{n-1}^I + \alpha l_n^T + l_{n+1}^I, \\ l_{\text{new}}^T &= l_{n-1}^T + \beta l_n^I + l_{n+1}^T, \end{aligned} \quad (3.42)$$

where $\alpha < 1$ and $\beta > 1$. The idea is that when two insulating blocks absorb a thermal block, their localization length increases, such that it becomes easier for two thermal block to thermalize

them during a “TIT” move. Equivalently [68], one can keep track of the decay length ζ of each thermal block (representing the typical decay length of the l-bits), normalized in such a way that if ζ reaches one, the quantum avalanche occurs. With this setting, during a “IT” move, the decay length of the newly formed insulating block will be smaller the larger the absorbed thermal block is. These RG rules lead to a scaling of the form (3.40).

Assuming that the ergodic/MBL transition is continuous, and using the usual RG arguments [28], quantities which characterize the phase transition, such as the entanglement density, are expected to follow a *scaling hypothesis* of the form [71, 80]:

$$A(L, W) \sim \frac{1}{L^a} \tilde{A}(\delta L^{\frac{1}{\nu}}). \quad (3.43)$$

In Ref. [80], the following bound for the critical was derived:

$$\nu \geq \frac{2}{d}. \quad (3.44)$$

It supposes only the above scaling hypothesis and that at the transition point the variable \tilde{A} experiences a jump.

4 Matrix-product states

The matrix-product state (MPS) formalism was first proposed as an analytical tool, starting in 1968 by Baxter [81], followed later by the realization that the ground state of the AKLT model [82] could be expressed under trix-prodrn [83]. Later, the connection between MPS and the density matrix renormalization group (DMRG) was first made by Ostlund and Rommer [84]. It is only in 2003 and 2004 that Vidal, Cirac, Verstraete and collaborators fully grasped the importance of the variational power of MPS [85, 86]. It was realized that not only the MPS variational class is extremely powerful to investigate ground state physics, but is also useful in the field of quantum dynamics [87].

In this chapter, we give a brief introduction to the MPS formalism and present some key algorithms used for finding ground states and performing time evolution. In particular, we give a practical introduction to the concept of tangent space of the MPS manifold and provide a derivation of the so-called time dependant variational principle (TDVP) [88].

4.1 The matrix-product state formalism

4.1.1 The matrix-product state ansatz

Any matrix M can be decomposed into matrices U, s and V according to:

$$M_{il} = U_{ij} s_{jk} V_{kl}, \quad (4.1)$$

where the matrix s is diagonal and the matrices U and V are *isometries*:

$$U^\dagger U = \mathbb{1} \text{ and } V^\dagger V = \mathbb{1}. \quad (4.2)$$

This decomposition is called the *singular value decomposition* (SVD). It can rewritten using the *graphical notation*:

$$\boxed{M} = \boxed{U} \boxed{s} \boxed{V}. \quad (4.3)$$

In this notation, the legs correspond to indices and contracted legs correspond to sum over the corresponding indices. Let us consider the following quantum state:

$$|\psi\rangle = \sum_{p_1, \dots, p_N} \psi_{p_1, \dots, p_N} |p_1, \dots, p_N\rangle \quad (4.4)$$

It can always be brought into the *matrix-product state* form, namely:

$$|\psi\rangle = \sum_{p_1, p_2, \dots, p_N} \sum_{\mu_1, \mu_2, \dots, \mu_{N-1}} M_{\mu_1}^{1, p_1} M_{\mu_1, \mu_2}^{2, p_2} \dots M_{\mu_{N-1}}^{N, p_N} |p_1, p_2, \dots, p_N\rangle \quad (4.5)$$

where $M^{i,p_i} \in \mathbb{C}^{\chi_i \times \chi_{i+1}}$ is the matrix corresponding to site i and to the local state $|p_i\rangle$. Note that, in the case of finite systems with open boundary conditions, M^{1,p_1} (resp. M^{N,p_N}) are row (resp. column) vectors of size χ_1 (resp. χ_{N-1}) to make the wave function coefficients scalar. The indices μ_i are called the *virtual* indices, while the indices p_i are the *physical* indices since they are identical with the indices found in the wave function tensor ψ_{p_1, \dots, p_N} . In the graphical notation we have:

$$\sum_{\mu_1, \mu_2, \dots, \mu_N} M_{\mu_1}^{1,p_1} M_{\mu_1, \mu_2}^{2,p_2} \dots M_{\mu_{N-1}}^{N,p_N} = \begin{array}{c} \boxed{M^1} \\ | \\ \boxed{M^2} \\ | \\ \dots \\ | \\ \boxed{M^N} \\ | \end{array} \quad (4.6)$$

In order to go from (4.4) to (4.24), we start by considering the tensor ψ_{p_1, \dots, p_N} as a matrix of dimension $2 \times 2^{L-1} : \psi_{(p_1), (p_2, \dots, p_N)}$. Then one can perform a SVD as in (4.3) and identify the matrix U as the tensor M^{1,p_1} . The matrix s is then absorbed into V , and the process can continue until all the tensors M^{i,p_i} are obtained. For the MPS representation to be exact, the required *bond dimension* χ_i at site i is given by:

$$\chi_i = \min(d^i, d^{L-i}), \quad (4.7)$$

where d is the local dimension of the Hilbert space. However, the advantage of the MPS becomes apparent when *truncation* occurs, namely when the smallest singular values of the SVD (and the corresponding columns/rows of the isometries) are discarded. When the discarded singular values are sufficiently small, their contribution to the quantum state are negligible, and the MPS is therefore a good approximation. In particular, the states following *area law* — where the entanglement entropy grows proportionally to the area of the cut, and is therefore constant in one dimension — can be arbitrarily well approximated with a finite bond dimension independent of system size. We have seen in section 3.2.1 that entanglement in eigenstates of MBL Hamiltonians follow area law. Furthermore, it has been proven in Ref. [5] that ground states of gapped one-dimensional quantum systems follow area law.

Note that the procedure that we have just described — starting from the state expressed in the full Hilbert space basis and convert it into a MPS — is impossible to carry out in practice for large system sizes, due to the exponential large dimension of the Hilbert space. In the following sections, we will review some efficient methods which were used in this work to obtain good approximations of the quantum states of interest.

Finally, as states can be efficiently written as MPS, operators such as Hamiltonian can also be efficiently represented as matrix-product operators (MPO). In general, an operator can be expressed as:

$$\begin{aligned} \hat{O} &= O^{p_1, p_2, \dots, p_N, q_1, q_2, \dots, q_N} |p_1, p_2, \dots, p_N\rangle \langle p_1, p_2, \dots, p_N| \\ &= \sum_{\mu_1, \mu_2, \dots, \mu_{N-1}} W_{\mu_1}^{1,p_1 q_1} W_{\mu_1, \mu_2}^{2,p_2 q_2} \dots W_{\mu_{N-1}}^{N,p_N q_N} |p_1, p_2, \dots, p_N\rangle \langle p_1, p_2, \dots, p_N| \end{aligned} \quad (4.8)$$

In the graphical notation, a MPO reads:

$$O^{p_1, p_2, \dots, p_N, q_1, q_2, \dots, q_N} = \begin{array}{c} | \\ \boxed{W^1} \\ | \\ \dots \\ | \\ \boxed{W^{i-1}} \\ | \\ \boxed{W^i} \\ | \\ \boxed{W^{i+1}} \\ | \\ \boxed{W^{i+2}} \\ | \\ \dots \\ | \\ \boxed{W^N} \\ | \end{array} \quad (4.9)$$

4.1.2 Some properties of matrix-product states

The MPS representation is not unique. Indeed, if one call $\{X_1, \dots, X_{L+1}\}$ a set of invertible matrices, with $X_1 = X_{L+1} = \mathbb{1}$, the following transformation leaves the state invariant:

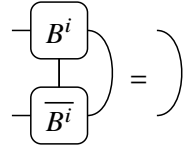
$$M^{i,p_i} \rightarrow X_i M^{i,p_i} X_{i+1}^{-1}. \quad (4.10)$$

This freedom in the representation of the state, referred as *gauge freedom*, can be used advantageously. A MPS is in the *left canonical form*, and denoted A^i if:



$$(4.11)$$

Conversly, it is in the *right canonical form*, and denoted B^i if:



$$(4.12)$$

In particular, for a MPS in either canonical form, the expectation value of local operators can be evaluated efficiently. For example, the expectation value of a single site operator O^i is given by:

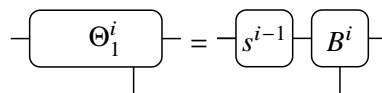


$$(4.13)$$

Indeed, one can write the wave-function in the *mixed canonical form*:

$$|\psi\rangle = \sum_{p_1, \dots, p_N} A^{1,p_1} \dots A^{i-1,p_{i-1}} s^{i-1} B^{i,p_i} \dots B^{N,p_N} |p_1, p_2, \dots, p_N\rangle. \quad (4.14)$$

When taking the overlap, the A tensors will give identity to the right and the B tensors to the left, hence the result. Since all the local degrees of freedom at site i are contained in the tensors B^i and the singular values s^{i-1} , one can express all the reduced density matrices in terms of the MPS tensors. It is useful to introduce the *one site wavefunction* tensor:



$$(4.15)$$

The one site reduced density matrix can be expressed as:

$$\rho_1^i = \sum_{p_i, p'_i} (R_1^i)^{p'_i, p_i} |p'_i\rangle \langle p_i| \quad (4.16)$$

where:

$$(R_1^i)^{p'_i, p_i} = \begin{array}{c} \text{---} \\ \text{---} \end{array} \left(\begin{array}{c} \boxed{\Theta_1^i} \\ \boxed{\Theta_1^i} \end{array} \right) \begin{array}{c} \text{---} \\ \text{---} \end{array} \quad (4.17)$$

This construction can be generalized to construct the n site wave function (from which one can obtain the n site density matrix). In particular, if one traces out the part of the system on the left of site i , the reduced density matrix ρ_R^i will be:

$$\rho_R = \sum_{\mu_i} s_{\mu_i, \mu_i}^i |\alpha_R, \mu_i\rangle \langle \alpha_R, \mu_i| \quad (4.18)$$

where $|\alpha_R, \mu_i\rangle = |\psi\rangle = \sum_{p_{i+1}, \dots, p_N} \sum_{\mu_{i+1}, \dots, \mu_N} B_{\mu_i, \mu_{i+1}}^{i+1, p_{i+1}} \dots B_{\mu_N}^{N, p_N} |p_{i+1}, \dots, p_N\rangle$. From Eq. (4.18), it is clear that the states $|\alpha_R, j\rangle$ are the eigenvectors of the density matrix, and therefore the singular values squared s^i correspond to the eigenvalues of ρ_R . The bipartite entanglement entropy can be expressed as a function of the singular values. Indeed:

$$S := -\text{Tr} \rho_R^i \log(\rho_R^i) = -\sum_{\mu_i} s_{\mu_i, \mu_i}^i \log(s_{\mu_i}^i) \quad (4.19)$$

Let us briefly review the process by which a MPS is brought into the left canonical form. Let us suppose that the tensors A^1, \dots, A^{i-1} are already in the left canonical form, and that the tensor B^i is in the right canonical form. Then we perform the following operations:

$$\text{---} \boxed{s_{i-1}} \text{---} \boxed{B^i} \text{---} \boxed{M^{i+1}} \text{---} = \text{---} \boxed{A^i} \text{---} \boxed{s_i} \text{---} \boxed{B^{i+1}} \text{---} \quad (4.20)$$

where we have grouped the two left-most (resp. right-most) legs together and performed a SVD on the hence obtained matrix. The legs were ungrouped at the end of the SVD. We have thus obtained the tensor A^i in the left canonical form, and the tensor B^{i+1} in the right canonical form. At the next step, singular values s^i and the tensor B^{i+1} can be used in combination with M^{i+2} in order to carry out the procedure further. At the end of this *sweep*, the full MPS will be in the left canonical form.

4.2 Matrix-product state algorithms

4.2.1 The density matrix renormalization group

The idea behind the density matrix renormalization group (DMRG) is to find the ground state by variationally optimizing the MPS in order to minimize the energy of state [89]. Let us outline the main steps of the algorithm. We start from a MPS in the right canonical form. One proceeds by finding the *two site wavefunction* tensor:

$$\text{---} \boxed{s_{i-1}} \text{---} \boxed{B^i} \text{---} \boxed{B^{i+1}} \text{---} = \text{---} \boxed{\Theta_2^i} \text{---} \quad (4.21)$$

which minimizes the overlap $\langle \psi | H | \psi \rangle$. This optimal two site wavefunction is obtained by finding the ground state of the so called *two site effective Hamiltonian* at site i , $H_{\text{eff},2}^i$, given by:

$$H_{\text{eff},2}^i = \begin{array}{c} \boxed{A^1} \cdots \boxed{A^{i-1}} \quad \quad \quad \boxed{B^{i+2}} \cdots \boxed{B^N} \\ | \quad \quad \quad | \quad \quad \quad | \quad \quad \quad | \\ \boxed{W^1} \cdots \boxed{W^{i-1}} \quad \boxed{W^i} \quad \boxed{W^{i+1}} \quad \boxed{W^{i+2}} \cdots \boxed{W^N} \\ | \quad \quad \quad | \quad \quad \quad | \quad \quad \quad | \\ \boxed{A^1} \cdots \boxed{A^{i-1}} \quad \quad \quad \boxed{B^{i+2}} \cdots \boxed{B^N} \end{array} \quad (4.22)$$

This step can be efficiently performed using the Lanczos Algorithm [90, 91]. Then we perform a SVD on the new two site wavefunction tensor according to Eq. (4.3). We obtain the updated tensors A^i, s^i and B^{i+1} which can be then used to construct the effective Hamiltonian $H_{\text{eff},2}^{i+1}$ on the next site. At the end of this sweep (a left-right sweep), the MPS is in the left canonical form. By doing a right-left sweep, we get once again a MPS in the right canonical form. After a sufficient number of sweeps, the MPS is a good approximation of the ground state.

4.2.2 Time evolving block decimation

The TEBD algorithm [85, 87] is a powerful and simple tool to simulate the short time dynamics of one-dimensional systems with short range interactions. It is applicable to both the Schrödinger and Heisenberg picture.

The key idea of the algorithm is to employ a Trotter decomposition of the time evolution operator in such a way that only local time evolution operators occur. For example a nearest-neighbor Hamiltonian is written as a sum over terms which involve only two neighboring sites: $\hat{H} = \sum_i h_{i,i+1}$ where $h_{i,i+1}$ is the part of \hat{H} containing the interaction between sites i and $i+1$. Since only nearest neighbor terms do not commute, we decompose the Hamiltonian into a part acting on the even bonds and a part acting on the odd bonds as $\hat{H} = H_{\text{even}} + H_{\text{odd}}$ where $H_{\text{even}} = \prod_j h_{2j,2j+1}$ and $H_{\text{odd}} = \prod_j h_{2j+1,2j+2}$. In this way all the terms contained in H_{even} (resp. H_{odd}) commute with each other. We can now apply a Trotter decomposition at first order for simplicity, although the implementation of any order is possible within this scheme. We obtain for the time evolution operator:

$$\begin{aligned} U(dt) &= e^{-i(H_{\text{odd}}+H_{\text{even}})dt} \\ &\approx e^{-iH_{\text{odd}}dt} e^{-iH_{\text{even}}dt} + O(dt^2) \\ &= \prod_j e^{-ih_{2j,2j+1}dt} \prod_j e^{-ih_{2j+1,2j+2}dt} + O(dt^2). \end{aligned} \quad (4.23)$$

Each term of the products in the third line of equation (4.23) can be written as a unitary gate linking two adjacent sites. In order to evolve an MPS with a time step dt we apply a layer of gates as shown in Fig. 4.1. It is then possible to re-express the time evolved state as an MPS of higher bond-dimension.

After each application of a unitary gate, the MPS is optimized by applying a SVD and truncating the smallest singular values, as in equation (4.20). This approximation is only valid in a regime where the state is lowly entangled, limiting the use of the method to short times for

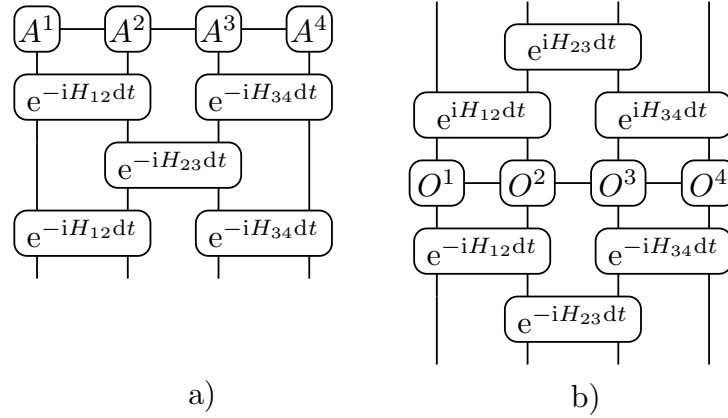


Figure 4.1 Schematic representation of the TEBD algorithm: a) Schrödinger representation, where A^i is the tensor at site i of the MPS corresponding to the state that we wish to evolve, H_{ij} denotes the gates of the Hamiltonian between sites i and j and dt is the time step; b) Heisenberg representation, where O^i is the tensor at site i of the MPO corresponding to the operator that we wish to evolve.

ergodic systems. Moreover the truncation process renders the time-evolution non unitary and does not preserve the norm of the state, the energy and other conserved quantities.

The TEBD algorithm is straightforwardly extended to the MPO-time evolution as illustrated on Fig. 4.1b, by noting that in contrast with the MPS case the (adjoint) unitary time evolution must be applied on the lower and upper legs of the MPO.

4.2.3 The time dependent variational principle using matrix-product states

The time dependent variational principle (TDVP) was first introduced by Dirac [92] for a general variational manifold. The general idea is to project the Schrödinger equation on the variational manifold of interest in such a way that the wave function after an infinitesimal time step does not leave the manifold, yielding an approximate tractable time evolution.

It has been recently formulated using MPS with a fixed bond dimension as the variational manifold [88,93] and is based on the concept of the tangent space of the MPS manifold [94]. The algorithm is very similar to the density matrix renormalization group (DMRG) [84,95] and offers several advantages with respect to the TEBD algorithm since it does not rely on truncation to keep the wave function in the manifold $\mathcal{M}_{\mathcal{MPS},\chi}$ of MPS with a given dimension χ . Moreover it is suitable to simulate Hamiltonians with long range interactions. To derive the TDVP algorithm, we start from an MPS wave function Eq. (4.24) as a variational ansatz. However, we make every tensor explicitly time dependent, i.e. $A^{[i]s_i} \rightarrow A^{[i]s_i}(t)$.

After inserting this ansatz into the Schrödinger equation, we find: $\frac{d|\psi[M]\rangle}{dt} = -i\hat{H}|\psi[M]\rangle$ where M denotes a point in the MPS manifold. The derivative of a MPS is given by:

$$\begin{aligned} \frac{d|\psi[M]\rangle}{dt} = & \sum_{p_1, p_2, \dots, p_N} \sum_{\mu_1, \mu_2, \dots, \mu_{N-1}} \partial_t M_{\mu_1}^{1, p_1} M_{\mu_1, \mu_2}^{2, p_2} \dots M_{\mu_{N-1}}^{N, p_N} + M_{\mu_1}^{1, p_1} \partial_t M_{\mu_1, \mu_2}^{2, p_2} \dots M_{\mu_{N-1}}^{N, p_N} + \dots \\ & + M_{\mu_1}^{1, p_1} M_{\mu_1, \mu_2}^{2, p_2} \dots \partial_t M_{\mu_{N-1}}^{N, p_N} |p_1, p_2, \dots, p_N\rangle, \quad (4.24) \end{aligned}$$

where $\partial_t M^{i,p_i}$ denotes the partial derivative of the tensor M^{i,p_i} . This can be expressed in the graphical notation:

$$\frac{d|\psi[M]\rangle}{dt} = \begin{array}{c} \boxed{\partial_t M^1} \cdots \boxed{M^i} \cdots \boxed{M^L} + \cdots + \boxed{M^1} \cdots \boxed{\partial_t M^i} \cdots \boxed{M^L} + \cdots \\ \vdots \qquad \qquad \qquad \vdots \qquad \qquad \qquad \vdots \qquad \qquad \qquad \vdots \qquad \qquad \qquad \vdots \\ \cdots + \boxed{M^1} \cdots \boxed{M^i} \cdots \boxed{\partial_t M^L} \end{array} \quad (4.25)$$

The set of tensors of the form (4.25) is called the *tangent space* of the MPS manifold at point M .

The goal of the TDVP approach is to find an expression for $\partial_t M^{i,p_i}$ and to integrate the resulting equation in order to time evolve the matrix-product state. Therefore we are looking for a solution of the form:

$$\sum_i \partial_t M^{i,p_i}(t) \partial_{M^{i,p_i}} |\psi(\{M^{k,p_k}(t)\})\rangle = -i P_T H |\psi(\{M^{k,p_k}(t)\})\rangle = -i |\theta[M]\rangle. \quad (4.26)$$

where P_T is the projector on the tangent plane of $|\psi(\{M^{k,p_k}(t)\})\rangle$. This projection is necessary to ensure that we obtain closed equations of motion in the tangent space so that the time evolved MPS is confined to $\mathcal{M}_{\mathcal{MPS},\mathcal{X}}$. The new equations of motion obtained this way can be elegantly integrated by means of a splitting method [88], as explained below.

The essential step in establishing the TDVP algorithm is to derive the projector. In order to do so, it is convenient to work in the mixed canonical form:

$$|\theta[B]\rangle = \sum_i \begin{array}{c} \boxed{A^1} \cdots \boxed{A^{i-1}} \boxed{T^i} \boxed{B^{i+1}} \cdots \boxed{B^L} \\ \vdots \qquad \qquad \qquad \vdots \qquad \qquad \qquad \vdots \qquad \qquad \qquad \vdots \end{array}$$

In order to find the projector on the tangent space, we need to determine the sets of tensors T^i 's. Therefore we are looking for the minimum of $\| |\theta[B]\rangle - |\gamma\rangle \|$:

$$|\tilde{\theta}\rangle = \min_{\{T^i\}} \langle \theta | \theta \rangle + \langle \gamma | \gamma \rangle - \langle \theta | \gamma \rangle - \langle \gamma | \theta \rangle \quad (4.27)$$

However, in the above expression, the term $\langle \theta | \theta \rangle$ contains L^2 terms. Indeed:

$$\langle \theta | \theta \rangle = \dots + \begin{array}{c} \cdots \boxed{T^{i-1}} \boxed{B^i} \boxed{B^{i+1}} \cdots \quad \cdots \boxed{A^{i-1}} \boxed{T^i} \boxed{B^{i+1}} \cdots \\ \vdots \qquad \qquad \qquad \vdots \qquad \qquad \qquad \vdots \qquad \qquad \qquad \vdots \\ \cdots \boxed{A^{i-1}} \boxed{\bar{T}^i} \boxed{B^{i+1}} \cdots \quad \cdots \boxed{A^{i-1}} \boxed{\bar{T}^i} \boxed{B^{i+1}} \cdots \\ \vdots \qquad \qquad \qquad \vdots \qquad \qquad \qquad \vdots \qquad \qquad \qquad \vdots \\ \cdots \boxed{A^{i-1}} \boxed{A^i} \boxed{T^{i+1}} \cdots \\ \vdots \qquad \qquad \qquad \vdots \qquad \qquad \qquad \vdots \\ \cdots \boxed{A^{i-1}} \boxed{\bar{T}^i} \boxed{B^{i+1}} \cdots \end{array} + \dots \quad (4.28)$$

In order to determine the projector, it is convenient to impose the condition:

$$\begin{array}{c} \boxed{T^i} \\ \vdots \\ \boxed{A^i} \end{array} = 0 \quad (4.29)$$

This is possible because of the *gauge freedom* of the tangent space. Namely, the transformation:

$$T^i \longrightarrow T^i + X^{i-1} B^i - A^i X^i, \quad (4.30)$$

where the X^i 's are matrices, does not change the wavefunction.

Let us show explicitly that starting from an arbitrary vector in the tangent space (represented by a set of A, B and T tensors), we can always find a set of matrices X^i 's which will satisfy the condition (4.29). Let us first solve the equation for the first site:

$$\sum_s A^{1,s\dagger} (T^{1,s} - A^{1,s} X^1) = \sum_s A^{1,s\dagger} T^{1,s} - \left(\sum_s A^{1,s\dagger} A^{1,s} \right) X^1 = 0. \quad (4.31)$$

Using the fact that $\sum_s A^{1,s\dagger} A^{1,s} = \mathbb{1}$, we obtain:

$$X^1 = \sum_s A^{1,s\dagger} T^{1,s} \quad (4.32)$$

Now let us suppose that X^1, \dots, X^{i-1} has been fixed. At site i , according to the gauge transformation (4.30), we need to solve the equation:

$$\sum_s A^{i,s\dagger} (T^{i,s} + X^{i-1} B^{i,s} - A^{i,s} X^i). \quad (4.33)$$

Hence we obtain:

$$X^i = \sum_s A^{i,s\dagger} T^{i,s} + A^{i,s\dagger} X^{i-1} B^{i,s} \quad (4.34)$$

Therefore one can indeed always satisfy the condition (4.29).

While minimizing (4.27), we need to impose the condition (4.29) as well as its conjugate. Therefore, we need to employ the Lagrange multiplier technique. Let us express the terms of (4.27) graphically:

$$\langle \theta[T] | \theta[T] \rangle = \sum_i \begin{array}{c} \dots - \boxed{A^{i-1}} - \boxed{T^i} - \boxed{B^{i+1}} - \dots \\ | \quad | \quad | \\ \dots - \boxed{\overline{A}^{i-1}} - \boxed{\overline{T}^i} - \boxed{\overline{B}^{i+1}} - \dots \end{array} = \sum_i \begin{array}{c} \boxed{T^i} \\ | \\ \boxed{\overline{T}^i} \end{array} \quad (4.35)$$

$$\begin{aligned} \langle \theta[B] | \gamma \rangle &= \sum_i \begin{array}{c} \boxed{\gamma} \\ | \\ \boxed{\overline{A}^1} - \dots - \boxed{\overline{A}^{i-1}} - \boxed{\overline{T}^i} - \boxed{B^{i+1}} - \dots - \boxed{B^N} \end{array} \\ &:= \begin{array}{c} \boxed{F_{|\gamma}^i} \\ | \\ \boxed{\overline{T}^i} \end{array} \end{aligned} \quad (4.36)$$

and

$$\langle \gamma | \theta[B] \rangle = \sum_i \text{tr} \begin{pmatrix} T^i \\ F_{|\gamma\rangle}^i \end{pmatrix} \quad (4.37)$$

If we call M^i and G^i the tensors containing all the Lagrange multipliers corresponding respectively to conditions (4.29) and its conjugate, we have the following Lagrangian:

$$\mathcal{L} = \sum_i \text{tr} \begin{pmatrix} T^i \\ \bar{T}^i \end{pmatrix} - \text{tr} \begin{pmatrix} F_{|\gamma\rangle}^i \\ \bar{T}^i \end{pmatrix} - \text{tr} \begin{pmatrix} T^i \\ F_{|\gamma\rangle}^i \end{pmatrix} - \text{tr} \begin{pmatrix} T^i \\ \bar{A}^i \end{pmatrix} M - \text{tr} \begin{pmatrix} A^i \\ \bar{T}^i \end{pmatrix} G \quad (4.38)$$

Now we need to solve:

$$\frac{\partial \mathcal{L}}{\partial \bar{T}^i} = 0 \quad (4.39)$$

$$= \text{tr} \begin{pmatrix} T^i \\ \cdot \end{pmatrix} - \text{tr} \begin{pmatrix} F_{|\gamma\rangle}^i \\ \cdot \end{pmatrix} - \text{tr} \begin{pmatrix} A^i \\ \cdot \end{pmatrix} G \quad (4.40)$$

We solve this equation by contracting with the \bar{A}^i tensor:

$$\text{tr} \begin{pmatrix} A^i \\ \bar{A}^i \end{pmatrix} G = G = \text{tr} \begin{pmatrix} F_{|\gamma\rangle}^i \\ \bar{A}^i \end{pmatrix} \quad (4.41)$$

where we have used the condition (4.29). Therefore:

$$\text{tr} \begin{pmatrix} T^i \\ \cdot \end{pmatrix} = \text{tr} \begin{pmatrix} F_{|\gamma\rangle}^i \\ \cdot \end{pmatrix} - \text{tr} \begin{pmatrix} A^i \\ F_{|\gamma\rangle}^i \\ \bar{A}^i \end{pmatrix} \quad (4.42)$$

Combining equation (4.25) and equation (4.26), it is not straightforward to relate the partial derivative $\partial_t M^i$ with the tensor T^i , because we worked in the mixed canonical form in the tangent space.

The equation (4.26) can be solved approximately by performing a Trotter decomposition. Indeed, one can time evolve A^i with the first term of (4.42) and s^i with the second term. One obtain:

$$\text{---} \left[\dot{\Theta}_1^i \right] \text{---} = -i \text{---} \left[F_{H|\phi}^i \right] \text{---} \quad (4.43)$$

where:

$$\text{---} \left[F_{H|\phi}^i \right] \text{---} = \begin{array}{c} \begin{array}{ccccccc} A^1 & \cdots & A^{i-1} & \Theta_1^i & B^{i+1} & \cdots & B^N \\ | & & | & | & | & & | \\ W^1 & \cdots & W^{i-1} & W^i & W^{i+1} & \cdots & W^N \\ | & & | & | & | & & | \\ \overline{A^1} & \cdots & \overline{A^{i-1}} & & \overline{B^{i+1}} & \cdots & \overline{B^N} \end{array} \\ \end{array} \quad (4.44)$$

In order to evolve the singular values, one writes:

$$\text{---} \left[A^i \right] \text{---} \left[\partial_t s^i \right] \text{---} = i \begin{array}{c} \left[A^i \right] \\ | \\ \left[F_{|\gamma\rangle}^i \right] \\ | \\ \left[\overline{A^i} \right] \end{array} \quad (4.45)$$

Contracting A^i with $\overline{A^i}$ yields identity due to the properties of the left canonical form, yielding:

$$\text{---} \left[\partial_t s^i \right] \text{---} = i \begin{array}{c} \left[F^i \right] \\ | \\ \left[\overline{A^i} \right] \end{array} \quad (4.46)$$

where:

$$\begin{array}{c} \left[F^i \right] \\ | \\ \left[\overline{A^i} \right] \end{array} = \begin{array}{c} \begin{array}{ccccccc} A^1 & \cdots & A^{i-1} & \Theta^i & B^{i+1} & \cdots & B^N \\ | & & | & | & | & & | \\ W^1 & \cdots & W^{i-1} & W^i & W^{i+1} & \cdots & W^N \\ | & & | & | & | & & | \\ \overline{A^1} & \cdots & \overline{A^{i-1}} & \overline{A^i} & \overline{B^{i+1}} & \cdots & \overline{B^N} \end{array} \\ \end{array} \quad (4.47)$$

It is useful to define the *one site effective Hamiltonian*:

$$H_{\text{eff},1}^i = \begin{array}{c} \boxed{A^1} \cdots \boxed{A^{i-1}} \quad \boxed{B^{i+1}} \cdots \boxed{B^N} \\ | \\ \boxed{W^1} \cdots \boxed{W^{i-1}} \quad \boxed{W^i} \quad \boxed{W^{i+1}} \cdots \boxed{W^N} \\ | \\ \boxed{\overline{A^1}} \cdots \boxed{\overline{A^{i-1}}} \quad \boxed{\overline{B^{i+1}}} \cdots \boxed{\overline{B^N}} \end{array} \quad (4.48)$$

as well as the *zero site effective Hamiltonian*:

$$H_{\text{eff},0}^i = \begin{array}{c} \boxed{A^1} \cdots \boxed{A^{i-1}} \quad \boxed{A^i} \quad \boxed{B^{i+1}} \cdots \boxed{B^N} \\ | \\ \boxed{W^1} \cdots \boxed{W^{i-1}} \quad \boxed{W^i} \quad \boxed{W^{i+1}} \cdots \boxed{W^N} \\ | \\ \boxed{\overline{A^1}} \cdots \boxed{\overline{A^{i-1}}} \quad \boxed{\overline{A^i}} \quad \boxed{\overline{B^{i+1}}} \cdots \boxed{\overline{B^N}} \end{array} \quad (4.49)$$

We are now ready to formulate the TDVP algorithm. We start from a MPS in the right canonical form, and perform a one site DMRG-like sweep. Instead of finding the ground state at each step of the sweep, we integrate the TDVP equations (4.46) and (4.43). To this aim, the one site wavefunction tensor is evolved according to $\Theta_1^i(t + dt/2) = \exp(-iH_{\text{eff},1}^i dt/2)\Theta_1^i(t)$ using the Lanczos algorithm [96]. Then we perform a SVD on the one site wavefunction. The U matrix will be reshaped to be $A^i(t + dt/2)$, the V matrix is absorbed into B^{i+1} and the s matrix is evolved according to $s(t + dt/2) = \exp(iH_{\text{eff},0}^i dt/2)s(t)$. At the end of this left-right sweep, the MPS is in the left canonical form and the wave function has been evolved by a time step $dt/2$. Then we perform a right-left sweep in order to obtain once again a wave-function in the right canonical form. The wave-function has been evolved by another time step $dt/2$. This scheme corresponds to a second order Trotterization of the time evolution.

5 Matrix-product state approaches to operator spreading in non-integrable systems

Most of the content of this chapter can also be found in a previous publication of the author [1]. Text and figures have been adjusted to fit into the context of the thesis.

5.1 Introduction

The question of quantum thermalization in closed systems receives currently a considerable amount of attention. This interest is partly due to the experimental progress leading to increasingly well isolated experimental realizations of quantum many-body systems in ultracold atomic gases in optical lattices [97]. Furthermore, we have seen in chapter 2 that this problem is central for the understanding of the foundations of statistical physics [18, 98–101]. While the eigenstate thermalization hypothesis (ETH) [18, 98–101] is a mathematical hypothesis explaining why local observables assume values consistent with the micro-canonical ensemble at long times [102], it can be useful to consider a more intuitive argument, namely that an ergodic system acts as its own bath. In general, the unitary dynamics of isolated quantum systems precludes reaching a maximally mixed state if the system is initialized in a pure state. However, when considering only a small subsystem of the total system, the usual notion of thermodynamic equilibrium is recovered, as the reduced density matrix becomes equal to the corresponding thermodynamic density matrix [103, 104], as the rest of the system serves as a heat bath. The mechanism for this thermalization process is the loss of local quantum information over time, which implies that the full wave function of the initial state cannot be reconstructed from local measurements at long times [105]. In consequence of this loss of local information, the system becomes increasingly entangled, until the state of a subsystem reaches a maximally mixed state consistent with global constraints [102, 106, 107]. A direct local probe of the loss of local quantum information can be constructed by studying the spreading of initially local Heisenberg operators $\hat{O}_i(t)$ which become increasingly nonlocal over the course of time. The locality can be quantified by probing the real space support of $\hat{O}_i(t)$ using the norm of the commutator with another local operator \hat{V}_j . This quantity is now best known as the out-of-time-order correlator (OTOC) which was introduced to study quantum chaos [108, 109], and to bound the spreading of information in systems with short ranged interactions [110].

Certain universal properties of the OTOC can be well understood in random unitary circuits [31–34] where it is governed by hydrodynamic equations of motion. In these systems, a light cone structure was identified with a broadening front arising from the diffusive nature of the hydrodynamic equations. This diffusive behaviour has been found in numerically exact calculations in a noisy spin system [111]. However, no exponential regime with a fixed Lyapunov

exponent was found so far in such systems, nor in Hamiltonian systems with a small local Hilbert space and continuous time [112].

While the OTOC is a powerful and universal theoretical tool, it is very difficult to calculate in practice for generic quantum many-body systems, due to its operator nature. In the last few years, several numerical methods for calculating the OTOC emerged: exact operator evolution in the Heisenberg picture [113], matrix-product operators (MPO) evolution in the Heisenberg picture [114, 115] and an exact wave function technique in the Schrödinger picture [112]. In this chapter, we will carefully compare these techniques and add two more MPS methods based on a stochastic sampling of the OTOC in the Schrödinger picture using both time evolving block decimation (TEBD) [85] and the time dependent variational principle (TDVP) using matrix-trix-product states (MPS) [88, 93], which is currently discussed as a candidate method to extract late time hydrodynamic properties of quantum systems [116, 117]. While exact Schrödinger evolution using quantum typicality is currently the best choice to obtain the exact OTOC for Hilbert space dimensions of up to 10^9 even at late times [112], MPS techniques have been recently presented as complementary approaches. In particular, MPO time evolution using TEBD can be used to extract the tails of the OTOC at very long distances (see section 5.4.2). Here, we investigate, how MPS based time evolution techniques such as TEBD and TDVP in the Schrödinger picture compare to the method of MPO evolution.

This chapter is structured as follows: in section 5.2, we explain why the OTOC quantifies the spreading of operators in non-integrable systems. In section 5.3, we describe the numerical approaches we choose to simulate them using matrix-product states. Next, in section 5.4 we compare the results obtained by the different methods, both for small and larger systems, and assess to which extent our results can be trusted despite the low amount of entanglement included in our MPS approximations.

5.2 Measures of operators spreading in closed quantum systems: the out-of-time-order correlator

5.2.1 the out-of-time-order correlator, a measure of the propagation of quantum information

In ergodic isolated quantum systems, local operators in the Heisenberg picture typically spread over the course of time in a sense that their supports in real space grows. Here we study this spreading in a non-integrable spin- $\frac{1}{2}$ chain of length L . In this case, the growth of the support means that the expansion of an operator $\hat{V}_i(t)$ in the operator basis of strings of local Pauli operators $\hat{\sigma}_i$, $i \in \{0, 1, 2, 3\}$ ($\hat{\sigma}_0 = \hat{1}$):

$$\hat{V}_i(t) = \sum_{\alpha_1 \dots \alpha_L \in \{0,1,2,3\}} v_{\alpha_1, \dots, \alpha_L} \hat{\sigma}_{\alpha_1} \otimes \hat{\sigma}_{\alpha_2} \otimes \dots \otimes \hat{\sigma}_{\alpha_L} \quad (5.1)$$

acquires increasingly long strings of non-identity Pauli operators [31, 33, 34]. The growing complexity stems from the increasing nonlocality of the time evolution operator $\hat{U}(t)$ and is also related to the growth of the *operator entanglement entropy* [118–120]. In order to define the latter quantity, it is useful to consider the operator as a state living in a larger Hilbert space. More

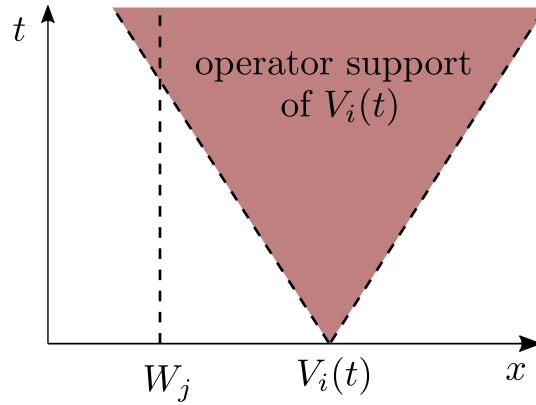


Figure 5.1 Schematic representation of the spreading of the operator support of an operator $V_i(t)$ initially at position $x = i$ as a function of time t . When the operator support reaches the position j , the quantity $\|[\hat{W}_j, \hat{V}_i(t)]\|_F^2$ starts to grow. The OTOC is therefore a measure of operator spreading in isolated quantum systems.

precisely, if we decompose an operator \hat{O} in terms of the elements of an orthonormal basis $\{|\phi_i\rangle\}$ as $\hat{O} = \sum_{ij} O_{ij} |\phi_i\rangle \langle \phi_j|$, we can then associate to this operator the state $|\phi_{\hat{O}}\rangle = \sum_{ij} O_{ij} |\phi_i\rangle \otimes |\phi_j\rangle$. The bipartite entanglement entropy of $|\phi_{\hat{O}}\rangle$ is called the operator entanglement entropy (assuming proper normalization). Note that the calculation of the entanglement of MPOs is identical to the MPS case: one has to find the singular values of the bond i of interest and as usual $S = -\sum_j s_j^2 \ln(s_j^2)$ where s_j are the singular values and S the entanglement.

The expansion in terms of Pauli string operators in Eq. (5.1) is a useful measure of operator spreading but is computationally impractical due to the arising of an exponentially large number of terms in the length of the chain. However, we note that in order to study the loss of locality of quantum information, the most interesting information is contained in how the length of Pauli strings grows over time. Therefore, we instead consider *commutators* of the operator $\hat{V}_i(t)$ with nontrivial ($\alpha \in \{x, y, z\}$) local Pauli operators (i.e. $\hat{\sigma}_{\alpha}^i = \hat{1} \otimes \dots \otimes \hat{1} \otimes \hat{\sigma}_{\alpha} \otimes \hat{1} \otimes \dots \otimes \hat{1}$):

$$[\hat{V}_i(t), \hat{\sigma}_{\alpha}^j] = \sum_{\alpha_1 \dots \alpha_L} v_{\alpha} [\hat{\sigma}_{\alpha_1} \otimes \hat{\sigma}_{\alpha_2} \otimes \dots \otimes \hat{\sigma}_{\alpha_L}, \hat{\sigma}_{\alpha}^j]. \quad (5.2)$$

This commutator is zero when the local Pauli operators $\hat{\sigma}_{\alpha_j}$ on site j are identities for all strings in the expansion $\hat{V}_i(t)$. Generically, when the operator support of $\hat{V}_i(t)$ reaches site j , its expansion in terms of Pauli strings will contain terms not commuting with $\hat{\sigma}_{\alpha}^j$. This commutator is therefore quantifying the operator spreading, as illustrated in Fig. 5.1.

However it is also an operator and is therefore usually reduced to its norm $\|[\hat{V}_i(t), \hat{\sigma}_{\alpha}^j]\|$. For computational simplicity, a standard choice for the norm is the normalized Frobenius norm given by $\|\hat{A}\|_F^2 = \frac{1}{N} \text{Tr} \hat{A}^{\dagger} \hat{A}$, leading to the definition

$$C_{ij}(t) = \frac{1}{2 \cdot Z} \|[\hat{W}_j, \hat{V}_i(t)]\|_F^2, \quad (5.3)$$

where Z is the dimension of the Hilbert space. We have chosen the normalization in order to ensure that $C_{ij}(t) \rightarrow 1$ at long times in the case where \hat{W}_j and \hat{V}_i are hermitian operators, which square to identity, such as Pauli operators.

5.2.2 The out-of-time-order correlator, a marker of quantum chaos

This quantity was originally proposed by Larkin and Ovchinnikov [108] in the context of quantum chaos. They showed that in chaotic systems with a semiclassical limit this norm of the commutator is connected to a Lyapunov exponent of the system and therefore effectively quantifies its chaoticity. Using this quantity they discussed a quantum analogue of classical chaos since in the semi-classical limit it quantifies the sensibility of classical trajectories to their initial conditions for the choice $\hat{W}_j = \hat{p}$ and $\hat{V}_i = \hat{x}$. This can be understood more intuitively by observing that the OTOC measures the effect of an initial perturbation on the value at later times of an operator located at some distance [109]. On the other hand, recent numerical studies of quantum systems with a small local Hilbert space and for 31 sites showed that there is no regime of exponential growth [112], a discrepancy to the semiclassical case [121], which has yet to be fully understood.

The link between the OTOC and locality of the Hamiltonian was made a few years later by Lieb and Robinson [110]. They realized that information in systems with short range interactions can only spread within a light-cone with only exponentially suppressed leaking. This is most effectively quantified by considering the spreading of initially local operators $\hat{V}_i(t)$ in the Heisenberg picture. More precisely:

$$\lim_{t \rightarrow \infty, |i-j| > vt} C_{ij} \exp[\mu(v)t] = 0, \quad (5.4)$$

for velocities $v > v_{LR}$, where v_{LR} is called the Lieb-Robinson velocity. The function $\mu(v)$ is now referred to as velocity dependent Lyapunov exponent [122].

The OTOC has been the subject of a renewed interest in the past few years due the establishment of a duality between some strongly correlated systems and black-holes and the proposal of exactly solvable models to illustrate it [123]. Moreover the spreading of operators is directly connected to the scrambling of local quantum information, since in chaotic systems at long times, initially local operators lose their locality and become completely scrambled [109].

5.3 Numerical considerations: calculating the out-of-time-order correlator with matrix-product states

If we restrict ourselves to hermitean unitary operators, which square to identity, such as Pauli operators, the OTOC C_{ij} can be expressed as:

$$C_{ij} = 1 - \frac{1}{2 \cdot Z} \text{Tr} \left(\hat{V}_i(t) \hat{W}_j \hat{V}_i(t) \hat{W}_j \right), \quad (5.5)$$

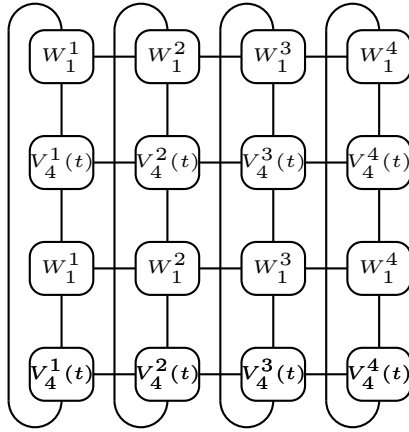


Figure 5.2 Example of trace calculation with MPOs following equation (5.5), using four sites. The tensor contraction gives the quantity $\text{Tr}(\hat{V}_4(t)\hat{W}_1\hat{V}_4(t)\hat{W}_1)$.

where $Z = \dim(\mathcal{H})$ is the dimension of the Hilbert space. The nontrivial part of the calculation of this quantity consists of determining the correlation function

$$\frac{1}{Z} \text{Tr}(\hat{V}_i(t)\hat{W}_j\hat{V}_i(t)\hat{W}_j), \quad (5.6)$$

which is exponentially expensive: for a spin- $\frac{1}{2}$ system of size L , $\hat{V}_i(t)$ is represented by a matrix in $\mathbb{C}^{2^L \times 2^L}$. Direct exact time evolution of the operator will therefore be very limited in system size [113].

Alternatively the trace can be stochastically evaluated with typical, randomly chosen wave functions due to quantum typicality. Although the time evolution will still be exponentially expensive, larger system sizes can be achieved since a state has only 2^L components. This has been achieved using exact Krylov space time evolution [112, 124–127]. Here, instead of operators, only wave functions are evolved in time by moving to the Schrödinger picture at the price of performing the time evolution forward and backwards in time, yielding an overall scaling of the method proportional to t_{\max}^2 . This is so far the most powerful numerically exact method to simulate the ergodic dynamics of small to intermediate system sizes up to arbitrary times and used here as a benchmark. For details of the method, see Refs. [112, 124].

Another approach is to use Heisenberg propagation of a matrix-product operator (MPO) representation [114, 115] of $\hat{V}_j(t)$ (see Fig. 4.1). To calculate $C_{i,j}$, one can use equation (5.5). We first evolve \hat{V}_j using the setup of Fig. 4.1b) with $O^j = \hat{V}$ and all the other operators O^k , $k \neq j$ set to identity. This way we obtain an MPO which tensors we denote as $V_j^l(t)$, the index l corresponding to the site of the tensor. We also write W_i as a MPO (which means that we place the operator \hat{W} on site i and identities operators on every other site). The calculation of the trace is then performed according to Fig. 5.2. This approach can seem to be limited to short times due to the linear growth of the operator entanglement entropy [118] implying the necessity of an exponentially large bond dimension for an exact representation of the Heisenberg operator.

It has been argued recently in Ref. [115] that this method is able to capture the early growth of the OTOC even with low bond dimension based on the following observation: first the spreading of quantum information is bounded by a light cone, implying that the operator entanglement

of bipartitions with a cut outside of the light cone is small, thus leading to a small required bond dimension. Therefore in the Heisenberg picture, only tensors inside the region where the entanglement is high will be truncated within the TEBD scheme. Finally, it is assumed that the effect of the truncation propagates as a light cone, meaning that the sites with low entanglement should not be affected immediately by the effect of a truncation far away from them. In numerical simulations, the convergence of the results with bond-dimension presented in Ref. [115] seems to support this reasoning. Our benchmarks for small systems (Fig. 5.5), our comparison of the contour lines of the OTOC obtained using MPO evolution to other methods (Fig. 5.9), as well as our analysis of the convergence with bond dimension (Fig. 5.12) also provide further support that MPO time evolution does indeed accurately capture the tail of the OTOC. We would like to note that this MPO technique has been applied in the past to calculate operator spreading in the one-dimensional Bose-Hubbard model in Ref. [114], where a discrepancy to the ballistic spreading at early times for small bond dimensions was pointed out, which was attributed to the truncation of the bond dimension.

Here, we propose a scheme based on the Schrödinger picture to MPS time evolution methods. The trace in Eq. (5.6) is sampled stochastically over random product states $|\sigma_1, \dots, \sigma_L\rangle$, which is reminiscent of minimally entangled typical thermal states (METTS) at infinite temperature [128] ($\beta = 0$). Additionally, we have the freedom to choose the basis such that the basis states are eigenstates of the operator \hat{W}_j , which we take for convenience to be $\hat{W}_j = \hat{\sigma}_j^z$:

$$\begin{aligned} \frac{1}{Z} \text{Tr} \left(\hat{V}_i(t) \hat{\sigma}_z \hat{V}_i(t) \hat{\sigma}_z \right) &\approx \\ &\approx \frac{1}{Z \cdot n_{\text{states}}} \sum_{\sigma}^{n_{\text{states}}} \langle \sigma | \hat{V}_i(t) \hat{\sigma}_j^z \hat{V}_i(t) | \sigma \rangle \sigma_j. \end{aligned} \quad (5.7)$$

This way, we only have to propagate one wave function (i.e. $|\sigma\rangle$) forward in time, apply \hat{V}_i , and propagate back to $t = 0$ for each initial state $|\sigma\rangle$. The average is performed over n_{states} initial states, which are sampled uniformly from the local σ_z product state basis (subject to sector constraints if required). From now on, we will restrict ourselves to the case $\hat{V}_i(t) = \hat{\sigma}_i^z(t)$. In order to evaluate equation (5.7), we use both the TEBD and the single site TDVP algorithms. In Ref. [88], a two-site implementation of the TDVP algorithm was proposed. However, in our case, this version of the algorithm would not be suitable for our purposes since it also relies on truncation to keep the bound dimension of the MPS fixed, hence yielding a non unitary time evolution and violating conservation of energy. However the single site algorithm does not allow to increase dynamically the bond dimension. In order to address this problem, we initialize our MPS as follows. First, we fill up the MPS with zeros in such a way that the product state, initially of bond dimension one, acquires the desired bond dimension χ . Second, we bring our inflated product state in canonical (isometric) form following the usual sweeping procedure [87]. This state is then a proper state and the single-site TDVP reproduces the correct time evolution. All the results obtained with the TEBD algorithm presented in this chapter were performed with a second order Trotter decomposition scheme. Unlike the TEBD algorithm, the TDVP algorithm conserves energy even when the exact time evolution cannot be captured by the MPS. Moreover all the conserved quantities, which do not cause an increase of bond dimension once applied to a MPS, are respected. In other words, a quantity \hat{O} commuting with the Hamiltonian is conserved by TDVP if for all states $|\phi\rangle$ expressible as a MPS of bond dimension χ we can still express $\hat{O}|\phi\rangle$ as a MPS of bond dimension χ . In the case where all conserved quantities leave the manifold

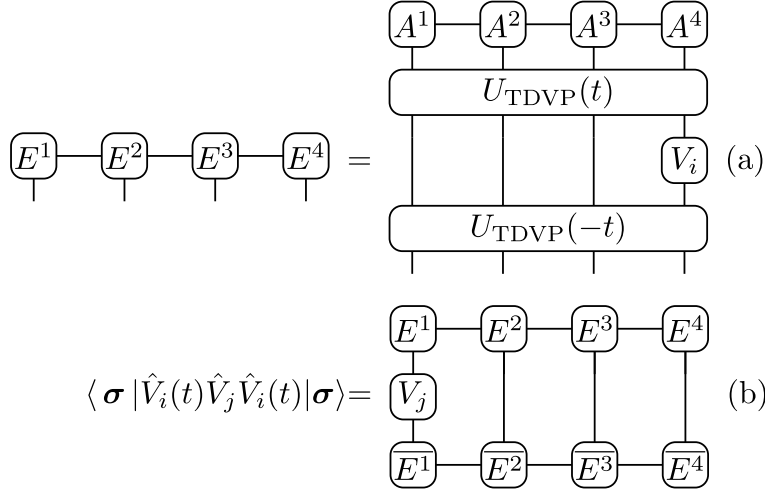


Figure 5.3 Example of calculation of time evolution necessary to obtain the OTOC with the MPS TDVP method using equation (5.7). (a) represents the time evolution $\hat{V}_i(t) |\sigma\rangle$, while the tensor contraction (b) represents the full out-of-order part of the correlator, up to the initial phase σ^z . These operation must be averaged stochastically to give the correct result.

$\mathcal{M}_{\mathcal{MPS}, \chi}$ invariant, TDVP appears well suited for the simulation of thermalization, since it is believed that at long times the dynamics of the system is driven by hydrodynamical equations of motion governed by conserved quantities [129–131]. Following this line of thought, TDVP has recently been applied successfully in the context of thermalization [116]. However the accuracy of results at long times is currently under debate [117]. It has also been used advantageously in disordered systems [132]. The TDVP algorithm provides a unitary time evolution. This feature will be of crucial importance when calculating OTOCs. In this work, we focus on short to intermediate times and will not consider the question of the relevance of TDVP in the context of hydrodynamics.

5.4 Results

We study a one dimensional quantum spin chain with short range interactions which has both integrable and non-integrable points as a function of the field angle: the tilted field Ising model. The Hamiltonian of the system is given by:

$$H = \sum_{i=1}^{L-1} J_z \hat{\sigma}_i^z \hat{\sigma}_{i+1}^z + \sum_{i=1}^L (h_x \hat{\sigma}_i^x + h_z \hat{\sigma}_i^z) \quad (5.8)$$

We consider this model at a strongly nonintegrable point, with no other conservation laws besides the global conservation of energy, which is exactly respected by our TDVP approach. Following Ref. [106], we use the following parameters throughout this article: $J_z = 1$, $h_x = (\sqrt{5} + 1)/4 = 0.8090$, $h_z = (\sqrt{5} + 5)/8 = 0.9045$.

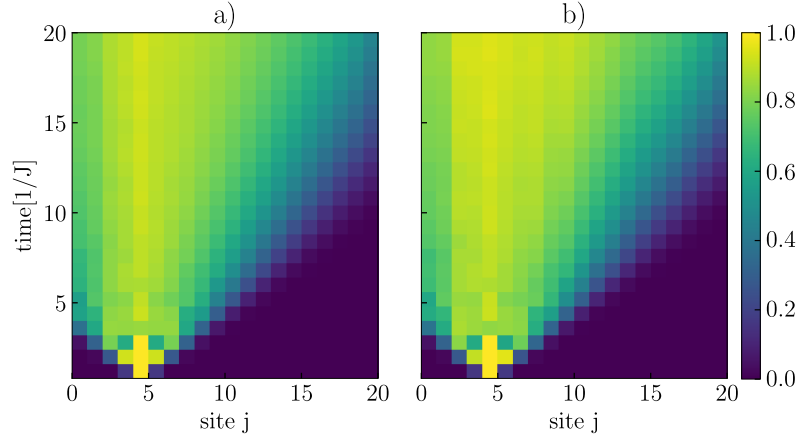


Figure 5.4 OTOCs for $L = 21$ obtained using a) ETE b) Schroedinger TDVP approach, sampling over 98 random product states and bond dimension $\chi = 64$.

5.4.1 Comparison of the methods with exact results

In order to explore the domain of validity of the different methods (MPS TDVP, MPS TEBD and MPO TEBD), we compare the results for the OTOC with exact results obtained by Krylov space based exact time evolution (ETE) for chains of $L = 21$ spins.

In Fig. 5.4, we show the exact results obtained using ETE on panel a) as well as the ones obtained using the MPS TDVP approach, using $\chi = 128$. A clear causality structure is observed, as explained in section 5.2.1 and illustrated on Fig. 5.1. We chose on purpose a relatively low bond dimension of $\chi = 64$ (this is to be compared with the full bond dimension needed for the MPS calculation to be exact: $\chi_{\max} = 1024$), in order to identify the possible errors arising from the approximation at hand. Despite the truncation occurring, the two light cones are barely distinguishable to the naked eye.

In order to gain more insight into the qualitative errors occurring for all the approaches considered, we present in Fig. 5.5 a detailed comparison for a system of size $L = 21$ of the OTOC $C_{4,j} = \frac{1}{2} \|\hat{\sigma}_4^z(t), \sigma_j^z\|_F^2$ obtained from the four methods compared in this article. All panels show the numerically exact result obtained from exact time evolution (ETE) as solid lines, panel a) shows the TDVP result for the OTOC obtained from stochastic sampling of the trace in Eq. (5.5) using 98 random product states, panel b) shows the same calculation but using TEBD time evolution instead. In panel c), we show TEBD MPO evolution results, using a direct evaluation of the trace. Here, all calculations were performed using a maximal bond dimension of $\chi = 64$. It is clear that at short times all three methods reproduce the exact result since there is no significant truncation occurring. Interestingly, the TDVP results stay close to the exact result for longer times than the OTOC obtained by TEBD.

Similarly to TDVP, the MPO evolution using TEBD captures very well the regime of low values of the OTOC. Nevertheless the growth and saturation regime is not correctly reproduced by any of the methods. With the Schrödinger approach the OTOC is systematically overestimated while it saturates to an unphysical value in the case of the Heisenberg approach.

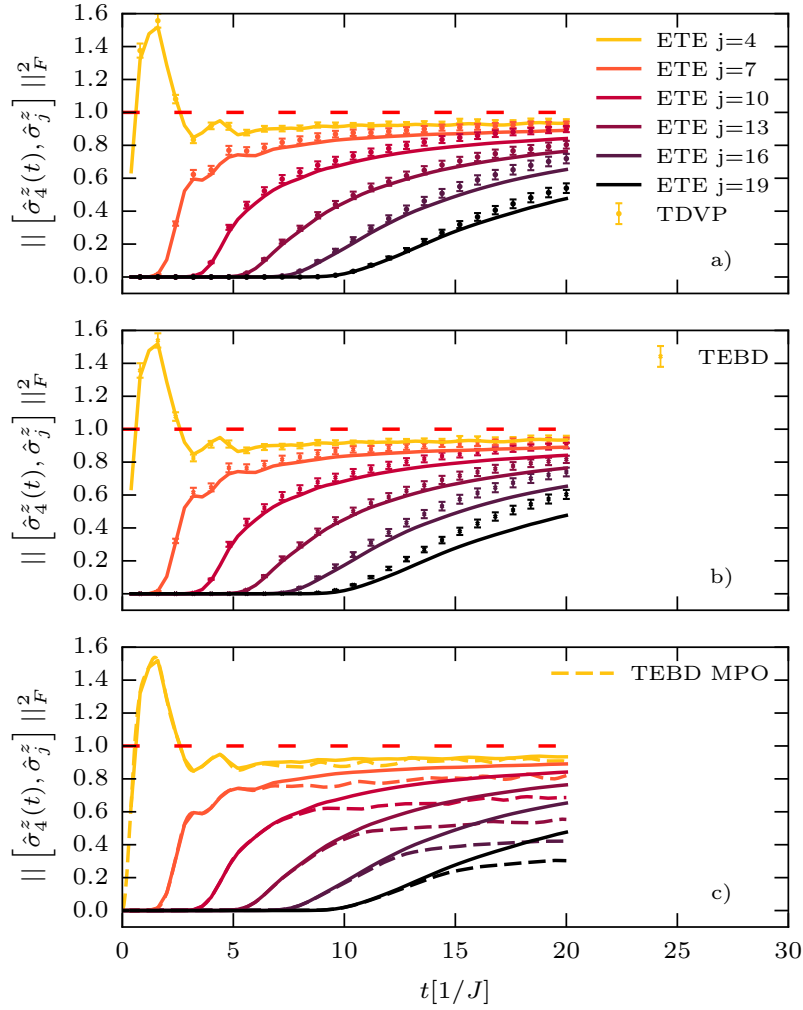


Figure 5.5 Fixed space cuts of the OTOC $C_{4,j} = \frac{1}{2} \|\ [\hat{\sigma}_4^z(t), \hat{\sigma}_j^z] \|^2_F$ obtained using different methods compared to exact time evolution (ETE). a) TDVP with wave function time evolution, where the trace in Eq. (5.5) is sampled using 98 random product states b) TEBD with wave function time evolution where the trace is sampled using 98 random states (the errorbars represent the error coming from the stochastic sampling) c) TEBD with operator time evolution (exact trace). All MPS calculations were performed with a time step $dt = 0.01$, bond dimension $\chi = 64$ and system size $L = 21$. The red dashed line is the theoretical upper bound for the long time limit for completely scrambled operators.

In order to make these statements more precise, we investigate the error of the different methods by considering the deviation from the exact result for $L = 21$. From Fig. 5.5, we see that the discrepancy from the exact result is the largest at long times and long distances, independently of the choice of the method. Therefore we illustrate the errors resulting from each of the three methods at the longest spatial distance in our system from the origin at $i = 4$ by the distance to the exact result $|C_{4,21}^{\text{exact}}(t) - C_{4,21}^{\text{MPS/MPO}}(t)|$ in Fig. 5.6. Here $C_{4,21}^{\text{MPS/MPO}}(t)$ stands for the OTOC calculated using either the MPS based methods with TEBD or TDVP time evolution or by the direct MPO based approach. We have checked that similar results are obtained for other distances.

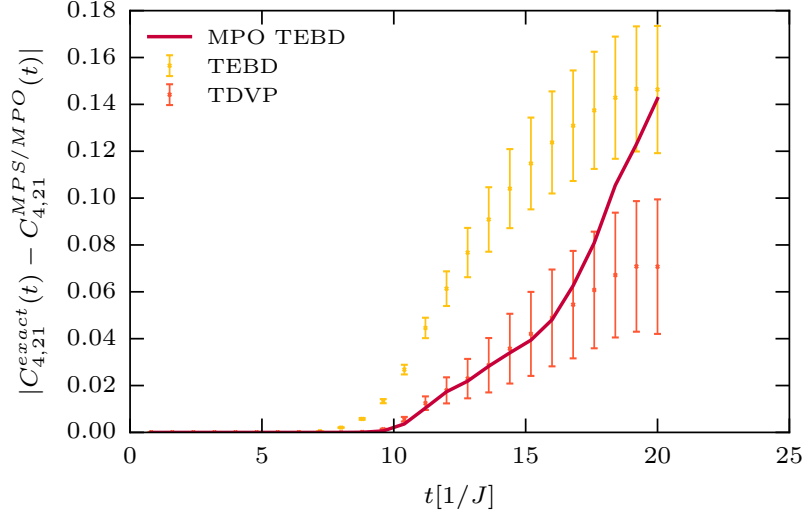


Figure 5.6 Deviation from the exact result using the three methods for the calculation of the OTOC for the longest distance from site $i = 4$ to $j = 21$ as a function of time. Based on the results shown in Fig. 5.5 (Bond dimension $\chi = 64$, time step $dt = 0.01$, system size $L = 21$ sites, the errorbars represent the error coming from the stochastic sampling).

These results are explained as follows. While TEBD in the Schrödinger picture suffers from the propagation of truncation errors since the wave function has to be propagated back to $t = 0$ after a measurement, TDVP profits from the preservation of unitarity by the method, leading to a significantly smaller error compared to TEBD MPS. As for the Heisenberg picture, the low value of operator entanglement at the front of the OTOC light cone allows the MPO TEBD approach to capture the low values of the OTOC as explained in section 5.3. The systematic underestimation of the OTOC saturation values is due to finite bond dimensions limiting the captured operator entanglement. We note that similar results have been obtained in disordered spin chains where it has been demonstrated that TDVP performs better than TEBD [133].

Convergence with bond dimension and comparison to exact results for TDVP MPS and TEBD MPS

In any MPS calculation, the convergence of the results with the bond dimension is an essential tool to assess the validity of the results. Here, we present an analysis of the convergence of the OTOC results calculated by our stochastic TDVP and TEBD methods based on MPS. We also analyze the convergence with the bond dimension of our TEBD MPO results.

In Fig. 5.7, for a system of size $L = 21$, we show the convergence of the OTOC $C_{4,j}(t)$ with bond dimension for the MPS time evolution methods that we compare in the main text (TDVP and TEBD). Since both methods rely on a stochastic sampling of the trace in Eq. (5.5), we eliminate the error induced by the stochastic sampling by selecting 5 random product states $|\psi_k\rangle$ and then calculating the approximate OTOC $C_{4,21}^{(5)} = 1 - \frac{1}{2^5} \sum_{k=1}^5 \langle \psi_k | \hat{\sigma}_4^z(t) \hat{\sigma}_j^z \hat{\sigma}_4^z(t) \hat{\sigma}_j^z | \psi_k \rangle$ with MPS TDVP, MPS TEBD and ETE for different bond dimensions (always using the same 5 product states). We plot the error given by the difference to the exact result for these 5 states

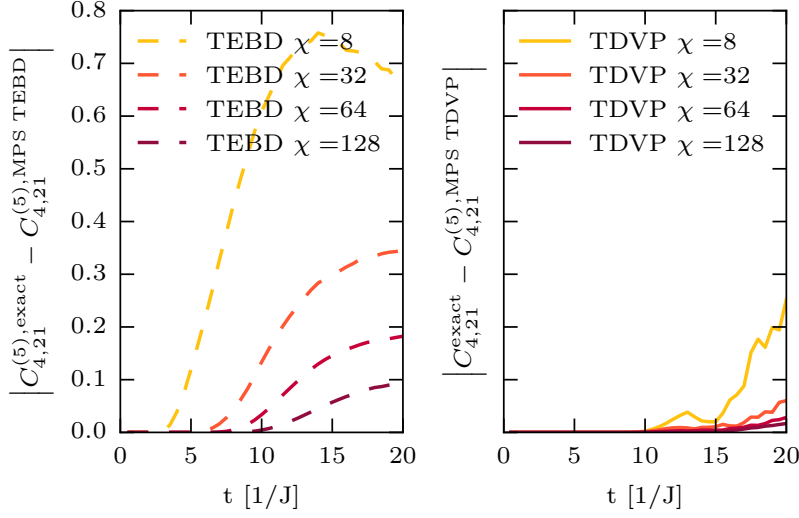


Figure 5.7 Comparison of the error $|C_{4,j}^{\text{exact}}(t) - C_{4,j}^{\text{TDVP MPS}}|$ for TDVP MPS and TEBD MPS $|C_{4,j}^{\text{exact}}(t) - C_{4,j}^{\text{TEBD MPS}}|$ for different bond dimension χ . The system sizes is $L = 21$, the time step is $dt = 0.01$.

($|C_{4,21}^{(5),\text{exact}} - C_{4,21}^{(5),\text{MPS}}|$) for different bond dimensions between $\chi = 16$ to $\chi = 128$ in Fig. 5.7. For clarity, we indicate the number of random product states included in this comparison in parentheses (here by (5)). We observe a clear convergence of the results from MPS TDVP. For MPS TEBD the error also decreases with the bond dimension, but stays always much larger than the one of TDVP. This underlines the advantage of the conservation of unitarity by TDVP time evolution.

5.4.2 Large systems and range of validity of the approximation

So far, we have presented results for systems small enough such that we could still compare to numerically exact results obtained by ETE. In what follows, we investigate the performance of these MPS and MPO methods for larger systems. We present in Fig. 5.8 the results for the OTOC $C_{4,j}(t) = \|\left[\hat{\sigma}_4^z(t), \sigma_j^z\right]\|_F^2$ as a function of time t and distance $j - 4$ for a system of size $L = 50$ sites with bond dimension $\chi = 64$ for both MPO TEBD and MPS TDVP. Again, we chose the position of the spreading operator $\hat{\sigma}_4^z(t)$ on the left of our chain with open boundaries instead of on the center, since this allows for a better resolution of the tails of the right part of the OTOC as discussed in Ref. [124].

For both methods, the time step dt has been decreased until convergence, and we found that a significantly smaller time step for TDVP of $dt = 0.005$ was required compared to the MPO TEBD time step of $dt = 0.01$, since the splitting methods of TDVP and TEBD differ. While in TEBD the exponential of the Hamiltonian is decomposed into two-site gates using a Trotter decomposition, in TDVP the update of every tensor requires the integration of coupled differential which are solved separately for every site i . In TEBD, only neighboring terms do not commute, while in TDVP the differential equations involving tensors $A_{kl}^{[i]s_i}(t)$ at site i depend on

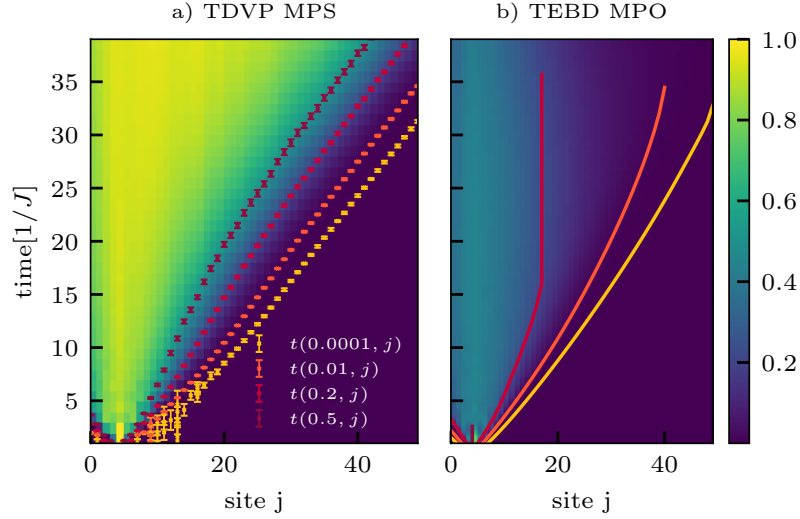


Figure 5.8 OTOC $C_{4,j}(t) = \frac{1}{2} \|\left[\hat{\sigma}_4^z(t), \sigma_j^z \right]\|_F^2$ as a function of distance and time for MPS TDVP with time step $dt = 0.005$, bond dimension $\chi = 64$ and averaged over 387 random states a) and MPO TEBD with time step $dt = 0.01$ and bond dimension $\chi = 128$ b), both for system size $L = 50$. The full lines and symbols correspond to contour lines obtained from the numerical solution of the equation $C_{4,j}(t) = \theta$ for various thresholds θ , where j is the position of the constant operator in the chain. The contour lines given by these solutions are denoted $t(\theta, j)$. The errorbars are representing the error coming from the stochastic sampling and are extracted using the bootstrap method.

the value of the tensors $A_{kl}^{[j]s_j}$ on all sites j . Therefore, a larger time step error can be expected in TDVP due to a more severe approximation in the splitting method.

For this reason, the dependence of the error on the time step is more important and must be checked carefully. Additionally, the stochastic sampling of the trace in Eq. (5.5) does not admit importance sampling and is therefore costly, practically limiting the bond dimensions considered here to $\chi = 64$. We evaluate the convergence in bond dimension of our results for both methods in section 5.4.2. We find that we achieve convergence for low values of the OTOC, which is consistent with the benchmarks shown in Fig. 5.5.

Here, we do not consider MPS TEBD results because of the inferior accuracy of this method already identified for smaller systems as discussed in the previous section.

The representation of the results in Fig. 5.8 from the two methods on the same colorscale illustrates the problem observed for smaller systems in Fig. 5.5 that MPO TEBD (right panel) underestimates the saturation value of the OTOC, in agreement with recent results of Ref. [133], while TDVP (left panel) reproduces the correct long time saturation value close to 1. Next, we consider contour lines (solid lines in Fig. 5.8) $t(\theta, j)$ of the OTOC obtained from numerical solutions of the equation $C_{4,j}(t) = \theta$ for various thresholds. For very low thresholds, these contours capture the behavior of the tail of the OTOC, where both methods yield consistent results even at long times. At larger thresholds, the obtained contours are strikingly different: while MPS TDVP yields approximately linear contour lines, close to a linear light cone, the results obtained with MPO TEBD deviate strongly and yield a significantly slower information spreading. Due to the problems identified for MPO TEBD closer to the saturation regime of the

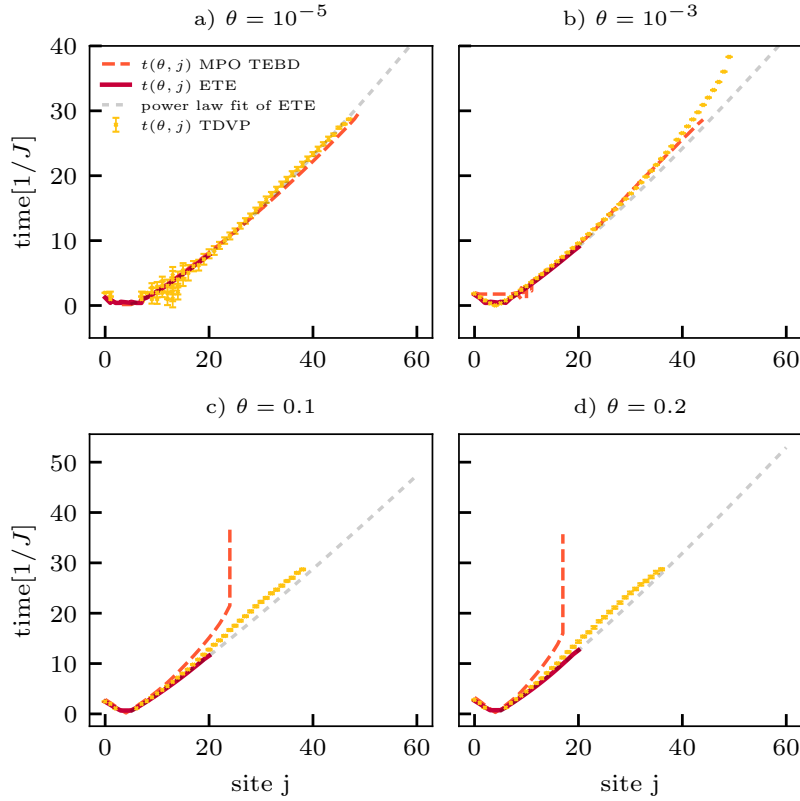


Figure 5.9 Contour lines obtained from the numerical solution of the equation $C_{4,j}(t) = \theta$ for various thresholds θ and methods, where j is the site. These solutions are denoted $t(\theta, j)$. The different methods used are MPO TEBD, MPS TDVP and ETE. We fit the ETE data between the sites 4 and 21 with a power law: $f(x) = \lambda(4 - x)^\mu$ with x the distance and the fitting parameters: a) $\lambda = 0.20$, $\mu = 1.32$, b) $\lambda = 0.31$, $\mu = 1.21$, c) $\lambda = 0.50$, $\mu = 1.12$, d) $\lambda = 0.52$, $\mu = 1.14$. The data comes from the same calculation as Fig. 5.8 (MPS TDVP: bond dimension $\chi = 64$, time step $dt = 0.005$, system size $L = 50$ sites, averaged over 387 random states; MPO TEBD: bond dimension $\chi = 128$, time step $dt = 0.01$, system size $L = 50$ sites). The errorbars are obtained in the same way than in Fig. 5.8 a).

OTOC as discussed in 5.4.1, we attribute this behavior to the error caused by the insufficient amount of operator entanglement included in our MPO approximation. The approximately ballistically spreading information front obtained with our MPS TDVP approach appears to be a qualitative improvement in comparison with MPO time evolution where the speed of information propagation seems to be underestimated. However, although qualitatively interesting, these results should not be trusted quantitatively at high thresholds since they are not converged in bond dimension in this region of space-time.

The results displayed in Fig. 5.8 can only be compared qualitatively, therefore we proceed by extracting the contours $t(\theta, j)$ of the OTOC for various values of the threshold and plot the results from MPS TDVP and MPO TEBD in the same figure panel for a direct quantitative comparison. In addition to the MPS results for $L = 50$ also the exact results for $L = 21$ are shown in Fig. 5.9. This is an important comparison, since results in other systems demonstrate that for short enough times, the OTOC does essentially not show any finite size effects [112, 124]. The contours obtained with ETE and MPS/MPO methods for different system sizes are therefore

expected to coincide for short times and the contours at low thresholds should not depend on system size.

For very small thresholds ($\theta = 10^{-5}$ and $\theta = 10^{-3}$), see Figs. 5.9a and 5.9b, the contours obtained with MPO TEBD and MPS TDVP indeed match the exact results, in accordance with results of Fig. 5.5, confirming our expectations. However, some differences start to appear at higher thresholds ($\theta = 0.1$ and $\theta = 0.2$), see Figs. 5.9a and 5.9b, which can be expected from our study of convergence in bond dimension (see section 5.4.2). We note that our MPS TDVP seems to yield a contour slightly closer to the exact result.

For small thresholds, it was previously observed in generic spin systems that the contours of the OTOC assume a power law shape with exponents close to unity [112]. Therefore, we attempt power law fits to our numerically exact contours from ETE, yielding excellent fits. The fits are shown as gray dashed lines in Fig. 5.9, and should be understood as an extrapolation of the shape of the light cone from the $L = 21$ results. For small thresholds ($\theta = 10^{-5}$), the MPS/MPO approaches reproduce the extrapolated contours with very high accuracy, confirming the power law fit from the smaller system size and consistency with the exact result. For $\theta = 10^{-3}$, the two approximated approaches are still in quite good agreement with the fit of the ETE, although some differences arise at later times. At higher thresholds, the difference is even more significant, since already short times results do not agree. This confirms our overall observation that the MPS approaches considered here reproduce the tail of the OTOC with good accuracy, while the growth and saturation regimes are not well captured.

Convergence with bond dimension for larger systems in TDVP MPS

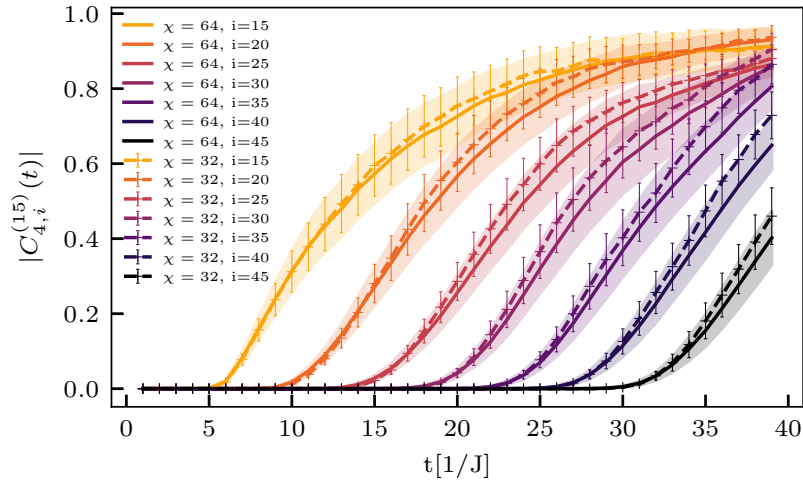


Figure 5.10 Convergence in bond-dimension of fixed space cuts of the OTOC $C_{4,j}^{(15)}(t) = 1 - \frac{1}{2^{15}} \sum_{k=1}^{15} \langle \psi_k | \hat{\sigma}_4^z(t) \sigma_j^z \sigma_4^z(t) \sigma_j^z | \psi_k \rangle$ obtained with Schrödinger TDVP with the same 15 randomly chosen initial product states $|\psi_k\rangle$ for bond dimension $\chi = 64$ and $\chi = 32$ for time step $dt = 0.01$, and system size $L = 50$.

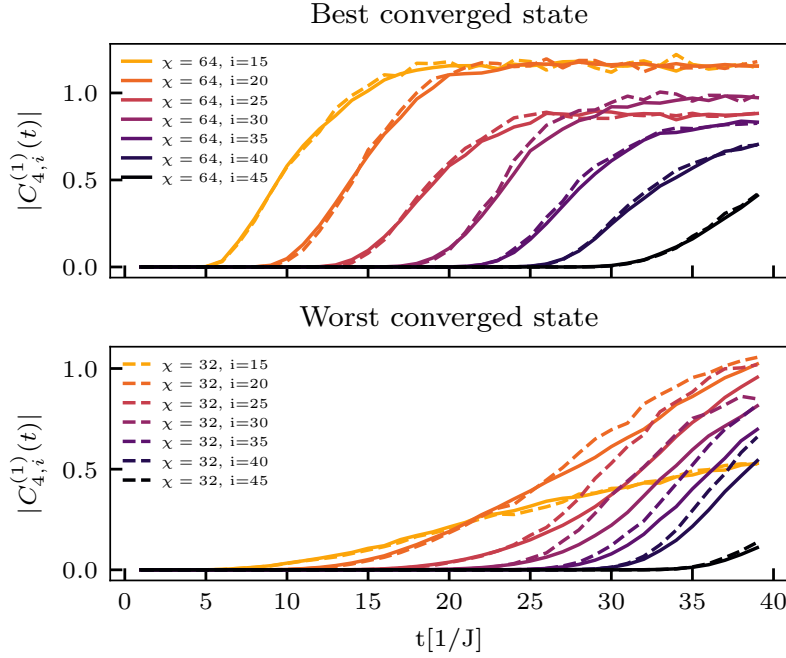


Figure 5.11 Convergence in bond-dimension of fixed space cuts of the OTOC $C_{4,j}^{(1)}(t)$ obtained with Schrödinger TDVP for only *one* random initial product state for bond dimension $\chi = 64$ and $\chi = 32$ and using a time step $dt = 0.01$ for a system of size $L = 50$. The worst and best converged initial states of the ones used in Fig. 5.10 are displayed in order to demonstrate the difference in convergence depending on the initial state.

For larger system sizes, it is difficult to obtain exact results for the OTOC as a benchmark. Therefore, a careful analysis of the dependence of the results on the bond dimension is crucial to identify the domain of validity of the methods. As we are unable to perform the simulation with a bond dimension sufficient to capture the growth entanglement which would manifest itself with the exact time evolution, we identify the regimes where increasing the bond dimension leaves the results invariant.

In the case of the TDVP MPS approach, we compare cuts $C_{4,j}^{(15)}(t)$ of the approximate OTOC using 15 random initial product states in the σ_z basis for several fixed distances. Note the same initial states are chosen for both bond dimensions in order to eliminate the importance of statistical errors in this comparison as explained above. For converged results within this approach, the mean and the error (calculated using bootstrap sampling) obtained for different bond dimension results should perfectly agree. In Fig. 5.10, we show the approximate OTOC $C_{4,j}^{(15)}(t)$ for $\chi = 32$ and $\chi = 64$ together with the errorbars of the OTOC (shaded region for $\chi = 64$ and errorbars for $\chi = 32$), yielding very good agreement of the results for low thresholds. At larger thresholds, the discrepancy between the two bond dimension results becomes significant as expected.

We find that the convergence in bond dimension depends significantly on the initial state and therefore we repeat this analysis for approximate OTOCs $C_{4,j}^{(1)}(t)$ using only single random product states and different bond dimensions in Fig. 5.11. From the 15 product states included in Fig. 5.10, we select the states with the best and worst convergence in bond dimensions to illustrate these state to state differences. Overall convergence is only achieved only for low values

of the OTOCs, confirming the observation that the tail of the OTOC is reproduced accurately, while values at larger thresholds are not converged.

Convergence with bond dimension for larger systems in TEBD MPO

In the case of the MPO TEBD approach, the study of the convergence in bond dimension is facilitated by the absence of stochastic sampling. The spacio-temporal dependency of the effect of bond dimension can be analyzed by directly looking at extracted contour lines $t(\theta, j)$ of the OTOC obtained from numerical solutions of the equation $C_{4,j}(t) = \theta$ for various thresholds and bond dimensions. We present the result of this approach in Fig. 5.12.

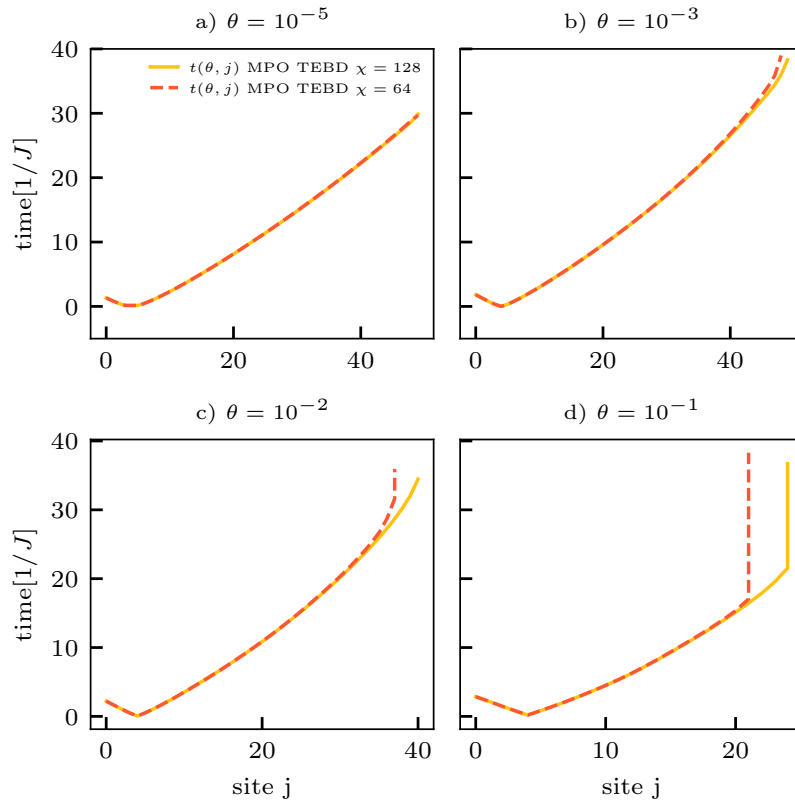


Figure 5.12 Convergence with bond dimension χ of the contours lines of the OTOCs calculated with MPO TEBD. We represent the numerical solution of the equation $C_{4,j}(t) = \theta$ for various thresholds θ and bond dimension ($\chi = 64$ and $\chi = 128$) for system size $L = 50$ sites and time step $dt = 0.01$. j is the site of the light cone for different thresholds θ (see Fig. 5.9).

The contours obtained with different bond dimension coincide very well for small thresholds (up to $\theta = 10^{-3}$). However a difference between $\chi = 64$ and $\chi = 128$ appears already for $\theta = 10^{-2}$ at times $t = 30$, which we attribute to the insufficient representation of the operator entanglement of the operator in an MPO with $\chi = 64$. The difference is even more striking for $\theta = 0.1$, where the results are not converged and do not show the expected asymptotic behavior of a linear light cone. The breakdown appears earlier for the lowest bond-dimension as expected.

5.4.3 Discussion

In the previous section, we provided numerical evidence that the two different methods shared the same area of validity, namely the region of space-time where the operator entanglement entropy is low. At first sight, this statement might seem intuitive, since MPS generally can represent relatively low entangled states which follow area law. However, the situation is different here, as during time evolution, operator entanglement deep into the light cone is very high. Furthermore, in the Schrödinger picture, the wave-function get rapidly entangled, as entanglement grows linearly in ergodic systems [31]. Therefore our results contain meaningful information about the propagation of errors in the methods at hand.

In Ref. [115], an argument is provided to show that the initial growth of the OTOC is correctly captured by the MPO evolution technique. The reasoning goes as follows: due to the Lieb-Robinson bound (5.4), the unitary time evolution acts as the identity operator in the region where the effect of the operator $V_i(t)$ did not yet propagate. When the effect of $V_i(t)$ starts to appear (at the intersection of the dotted line and of the cone in Fig. 5.1), the operator entanglement is still very low, and a very small bond-dimension is sufficient to capture the growth of the OTOC. While this argument is giving an elegant interpretation of the results, we note that it has been put into question [78]. Indeed, although it is clear that only a low bond-dimension is needed to faithfully represent the operator near the onset of the light-cone, it is hard to establish a priori that this region is unaffected by the severe truncation occurring deep inside the light-cone. For example, some non local effect could appear [114]. However, our careful numerical verifications indicate that this is the case in practice: the truncation errors propagate slowly enough so that they do not interfere with the boundary of the light cone.

In the case of the Schrödinger time evolution, the situation is slightly more complicated. When performing the forward time evolution, it is clear that the approximation made by the TDVP algorithm yields a state very different from the correct one. In particular, the entanglement entropy of this state is bounded by $\log(\chi)$. The next step (see Fig. 5.3), is to apply to operator σ_j^z , which can be seen as a perturbation, and perform the backward time evolution. Note that if we were to apply the identity operator instead, the backward time evolution would yield the correct result, namely the final state would be identical to the initial state, and the OTOC would be exactly zero everywhere. Our results indicate that far from the perturbation, at the other end of the chain, the unitary evolution is exactly canceled by its conjugate. For example, up to times 20, the OTOC at site 45 is vanishing (see Fig. 5.8, panel b). Finally, since the initial growth of the OTOC is correctly reproduced by our method, we conclude that the propagation of the perturbation is correctly captured by the TDVP approximation, even with low bond dimension.

We note the agreement for low threshold of the OTOC of the results obtained with both methods is a further evidence of the correctness of our results (see Fig. 5.9), since the approximations made in both cases are completely different.

5.5 Conclusion

We have compared different MPS approaches to study information scrambling in a generic spin chain based on both matrix-product states (MPS) and matrix-product operators (MPO) and

compared the results to an unbiased and numerically exact technique (ETE). For the calculation of the out-of-time-order correlators (OTOCs) in the Schrödinger picture based on MPS, we have shown that the use of a unitary time evolution method (TDVP) yields a significant improvement over the non-unitary truncation used in the time evolving block decimation (TEBD) algorithm. Furthermore we found that both MPO TEBD and MPS TDVP reproduce the tail of the OTOCs even at long times for low enough thresholds, while the growth and saturation regime suffers from truncation errors. The obtained shape of the light cone in large systems at low thresholds is in quantitative agreement with the ETE results at short times for smaller system size. Moreover they also match the extrapolated exact result even at late time. For larger thresholds, closer to the information front, a discrepancy from exact results is observed, which we attribute to insufficient convergence of both MPO TEBD and MPS TDVP results with bond dimension. However, our TDVP MPS approach still yields a qualitatively correct ballistic propagation of information in contrast with the results obtained with MPO TEBD where after significant truncation the spreading of information appears to halt, making the result unphysical. We also note that the asymptotic saturation value of the OTOC is correctly reproduced in our TDVP MPS approach, while strong truncation effects in the MPO TEBD approach lead to a severe underestimation of the saturation value.

We conclude that both MPS techniques in the Heisenberg and Schrödinger picture yield consistent results for the tails of the OTOC and their performance is comparable. However, the MPS TDVP approach comes at the price of introducing a stochastic sampling of the OTOC using random product states making it computationally much more expensive. An interesting future direction would be to apply our wave function approach to calculate the OTOCs in many-body localized system to evaluate whether the logarithmic growth of entanglement allow us to gather reliable results in a broader region of space-time and calculate the contours OTOCs at larger thresholds.

6 Probing diffusion in boundary-driven dissipative systems

6.1 Introduction

In the previous chapter we have explored the propagation of information in a quantum system using various matrix-product states (MPS) approaches. However, in general, these methods seem to be unable to reliably reach the long time limit [117]. Therefore, they fail to capture all characteristics of the dynamics of the system, such as transport coefficients of conserved quantities [117].

Transport properties are among the most experimentally studied characteristics of materials, allowing to classify various states of matter. In particular, identifying the possible universality classes emerging from transport in strongly interacting systems is the subject of very active research [134]. Many different quantities can be examined, such as heat [135], electric [136] and spin [137] conductivities. Although transport is described by phenomenological hydrodynamic theories at long times [35, 36], it is challenging to simulate starting from microscopic models. For example, transport coefficients can be obtained using the Green-Kubo formula, which requires the calculation of autocorrelation functions, and is usually limited to small system sizes [138]. Strongly interacting one-dimensional systems exhibit a large variety of transport properties of their conserved quantities, including ballistic, diffusive and subdiffusive transport. Generic non integrable systems are believed to exhibit diffusive transport [138, 139]. Spin transport can be probed experimentally on quantum magnets using various techniques such as muon spin relaxation [140, 141] or nuclear magnetic resonance [142]. Furthermore, transport has an important role to play in understanding the ergodic/many-body localization phase transition, as the critical point might be characterized by subdiffusive transport [137].

In this chapter, we explore the potential of a MPS-based approach originally proposed in Ref. [143], aiming at obtaining diffusion coefficients of one-dimensional systems. Namely, we simulate boundary-driven diffusive systems. We time evolve the system until it reaches the steady state, and deduce the diffusion coefficient from the current measured in this state. We compare our results to those of other methods, and conclude on the validity of the approach.

6.2 Probing transport properties using equilibrium steady states

6.2.1 The setup

Although we are ultimately interested in the transport properties of closed quantum system, we proceed by coupling our one dimensional chain with a bath acting only at the boundaries, such that it induces transport. The idea behind this procedure is that for a large enough system, at long times, the dynamics in the bulk will be approximately unitary, and the transport properties can be read directly from the current induced.

The non-unitary time evolution of the open system of interest is governed by a *master equation* of the form [144]:

$$\frac{d\rho}{dt} = \hat{\mathcal{L}}(\rho) = i[\rho, H] + \hat{\mathcal{L}}_B(\rho) = i[\rho, H] + \frac{\Gamma}{2} \sum_k [L_k \rho, L_k^\dagger] + [L_k, \rho L_k^\dagger], \quad (6.1)$$

where the superoperator $\hat{\mathcal{L}}$ is called the Lindbladian, and can be decomposed into unitary and a non-unitary part $\hat{\mathcal{L}}_B$ which generally involves Lindblad operators L_k . Note that in this chapter, we only consider baths acting at the boundaries of the system. It was conjectured in Ref. [143] that the steady states of such Lindbladians are unique and can be faithfully represented as a matrix-product operator (MPO) of low bond dimension. This claim was further justified in Ref. [145] using linear response theory (see also section 6.2.3).

By recasting the density matrix as a state $\rho \rightarrow |\rho\rangle$, the time evolution is then given by:

$$|\rho(t)\rangle = \exp(\hat{\mathcal{L}}t)|\rho(t=0)\rangle. \quad (6.2)$$

At the exception of the steady state which has eigenvalue 0, the eigenvalues of the superoperator $\hat{\mathcal{L}}$ have a negative real part. Therefore, when performing the time evolution under the master equation (6.2), at sufficiently long times, the state will reach the steady state ρ_∞ . This is analogous to an imaginary time evolution simulation in the unitary case, where ρ_∞ plays the role of the “ground state” of the Lindbladian.

The expectation of on operator \hat{O} with respect to the steady state is as usual as given by:

$$\langle \hat{O} \rangle_{\rho_\infty} = \text{Tr}(\rho_\infty \hat{O}). \quad (6.3)$$

6.2.2 Obtaining the diffusion coefficient from the non-equilibrium steady state

We are interested in the transport of a conserved quantity \hat{Q} of a Hamiltonian \hat{H} , i.e. $[\hat{H}, \hat{Q}] = 0$. We define the local charges q_i such that $\hat{Q} = \sum_i \hat{q}_i$. The current operator \hat{j}_i at site i is related to the local charges by:

$$\frac{d\hat{q}_i}{dt} = i[\hat{q}_i, \hat{H}] := \hat{j}_i - \hat{j}_{i-1}. \quad (6.4)$$

We expect that in the bulk of our system the expectation value of the current with respect to the steady state is independent of the site i where it is measured:

$$j := \langle \hat{j}_i \rangle_{\rho_\infty}. \quad (6.5)$$

In order to characterize the transport properties of our system, we relate the current to the driving field ϕ (which could be for example the magnetization density or chemical potential) [143, 145]:

$$j = f(\nabla\phi). \quad (6.6)$$

In the case of diffusion, the diffusion coefficient D is defined as [145]:

$$j = -D\nabla\phi. \quad (6.7)$$

In practice, in order to eliminate boundary effects, the the gradient can be expressed as [143]:

$$\nabla\phi = \frac{\phi(N - N_b) - \phi(N_b + 1)}{N - N_b}, \quad (6.8)$$

where $N_b \geq 1$ are the number of spins at the boundaries not taken into account.

6.2.3 Lindbladian perturbation theory and linear response theory

The usefulness of the method presented above rests on the assumption that the steady state can be expressed as a matrix-product operator with low bond dimension, as elaborated in the next section. In order to justify this hypothesis, one can use perturbation theory [145].

Let us start from a Lindbladian $\hat{\mathcal{L}}_0$ with unique steady state ρ_0 which is known exactly. We perturb $\hat{\mathcal{L}}_0$ and obtain:

$$\hat{\mathcal{L}} = \hat{\mathcal{L}}_0 + \mu\hat{\mathcal{L}}_1, \quad (6.9)$$

with μ is a small parameter quantifying the extend of the perturbation. We look for the steady state under the form:

$$\rho = \rho_0 + \mu\rho_1, \quad (6.10)$$

where the higher order terms can be discarded provided that μ is small enough. We have:

$$\hat{\mathcal{L}}\rho = \mu(\hat{\mathcal{L}}_1\rho_0 + \hat{\mathcal{L}}_0\rho_1) + O(\mu^2), \quad (6.11)$$

where we have kept only the linear order terms and used the fact that $\hat{\mathcal{L}}_0\rho_0 = 0$. Therefore:

$$\hat{\mathcal{L}}_1\rho_0 = -\hat{\mathcal{L}}_0\rho_1. \quad (6.12)$$

Note that one can formally write [145]:

$$\rho_1 = -\hat{\mathcal{L}}_0^{-1}\hat{\mathcal{L}}_1\rho_0 \quad (6.13)$$

which has a unique solution as long as $\hat{\mathcal{L}}_1\rho_0$ is orthogonal to ρ_0 .¹ We can now write the linear response equation for ρ_1 by starting from the Linblad equation for $\rho_0 + \mu\rho_1$:

$$\frac{d(\rho_0 + \mu\rho_1)}{dt} = \mu(\hat{\mathcal{L}}_1\rho_0 + \hat{\mathcal{L}}_0\rho_1). \quad (6.14)$$

¹Indeed, since by hypothesis ρ_0 is the only eigenstate of $\hat{\mathcal{L}}_0$ with zero eigenvalue, one can invert $\hat{\mathcal{L}}_0$ restricted to the subspace of vectors orthogonal to ρ_0 .

Using $\frac{d\rho_0}{dt} = 0$, we arrive to [145]:

$$\frac{d\rho_1}{dt} = (\hat{\mathcal{L}}_1\rho_0 + \hat{\mathcal{L}}_0\rho_1). \quad (6.15)$$

The solution of the above equation is given by [135, 145]:

$$\rho_1(t) = \int_0^t e^{\hat{\mathcal{L}}_0(t-\tau)} \hat{\mathcal{L}}_1\rho_0 d\tau. \quad (6.16)$$

The steady state of $\hat{\mathcal{L}}$ is therefore given by:

$$\rho_\infty = \rho_0 + \mu \int_0^\infty e^{\hat{\mathcal{L}}_0\tau} \hat{\mathcal{L}}_1\rho_0 d\tau = \rho_0 - \mu \int_0^\infty e^{\hat{\mathcal{L}}_0\tau} \hat{\mathcal{L}}_0\rho_1 d\tau. \quad (6.17)$$

Note that in the spin diffusion case that we consider section 6.4, the steady state of $\hat{\mathcal{L}}_0$ is proportional to the identity, i.e. $\rho_0 \propto \mathbb{1}$. Therefore, for traceless operators, only the correction term contributes to the expectation value. Since by assumption μ is small, the new steady state ρ_∞ should be lowly entangled and is expected to be well approximated by a MPO with relatively low bond dimension.

6.2.4 Matrix-product state implementation

In order to use MPS methods to simulate non-unitary dynamics, we represent the density matrix as a state: $\rho = \sum_{ij} \rho_{ij} |i\rangle\langle j| \rightarrow \sum_{ij} \rho_{ij} |i\rangle|j\rangle$. This is implemented in practice by representing the density matrix as a MPO, and transforming this MPO into a MPS by grouping together the physical indices of the : $W_{\mu_i, \mu_{i+1}}^{i, p_i q_i} \rightarrow W_{\mu_i, \mu_{i+1}}^{i, (p_i q_i)}$. We can then apply the standard time evolving block decimation (TEBD), explained in detail in section 4.2.2. Indeed, for a system with nearest neighbor interactions, the exponentiation of the Lindbladian factorizes into two site terms, allowing for the application of the usual Trotter decomposition. All the results presented in this chapter were obtained with time step $dt = 0.1$. The resulting scheme is illustrated in Fig. 6.1.

This method is expected to work when the targeted steady state is well described by linear response theory (see section 6.2.3). In this regime, the steady state is close to the infinite temperature density matrix, which is exactly represented as a MPO of bond dimension one. Therefore the steady state is expected to carry few operator entanglement and to be well approximated by a MPO with low bond dimension [143, 145].

In order to reach the steady state in reasonable time, following Ref. [146], we start by doing the time evolution with relatively low bond dimension, in order to arrive ‘‘in the neighborhood’’ of the steady state. We check that the truncation error during the time evolution stays relatively small (in practice, below 10^{-5}). We eventually reach the a fix point of the Linblad equation restricted to this MPS manifold with low bond dimension. The state thus obtained is already a good approximation of the steady state. Then we increase the bond dimension until we eventually reach convergence. As some light truncation occurs during the time evolution, the trace of the density matrix is not exactly conserved. This can be easily fixed by renormalizing the MPS. In practice, it is easier to compute the expectation value in the following way:

$$\langle \hat{O} \rangle_{\rho_\infty, \text{MPS}} = \frac{\text{Tr}(\rho_\infty \hat{O})}{\text{Tr} \rho_\infty} \quad (6.18)$$

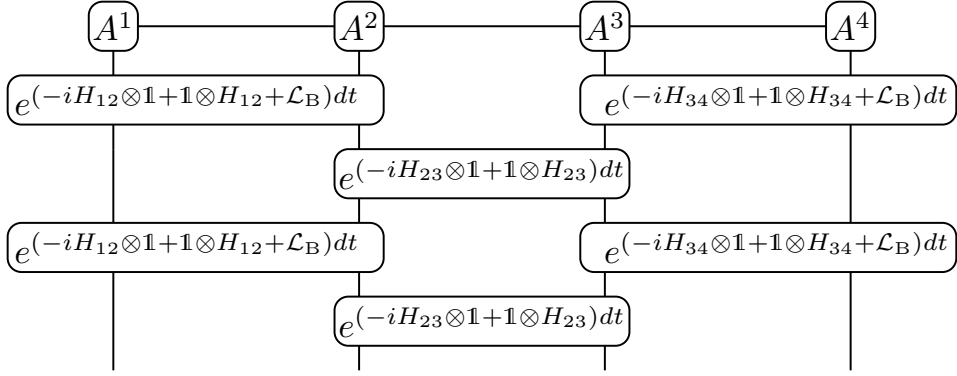


Figure 6.1 Example of two TEBD time steps applied to the density matrix expressed as a matrix-product state for a system size of 4 sites. The bath is coupled at most with the two left-most and right-most sites of the chain, while the time evolution is unitary in the bulk.

The trace of a density matrix expressed as a MPS is calculated by taking the expectation value $\langle \rho_{\text{MPS}} | \mathbb{1} \rangle$, where $|\mathbb{1}\rangle$ is the identity matrix expressed as a state.

6.3 Energy transport

6.3.1 Two spin bath

In order to induce energy current in our system, we couple the two left-most sites with a bath of temperature T_1 and the two right-most sites with another bath of temperature T_2 .

To this aim, we wish to construct a two sites Lindblad operator $\mathcal{L}_{B,T}$ which has for steady state [143, 147]:

$$\rho_{B,T} = \exp(-\beta h_{1,2}), \quad (6.19)$$

where $h_{1,2}$ is the Hamiltonian restricted to the two sites considered and $\beta = \frac{1}{k_B T}$. Furthermore, we wish $\mathcal{L}_{B,T}$ to have eigenvalues -1 associated with all its non steady eigenstates.

Note that if $T_1 = T_2 = T$, it has been shown numerically [148] that the steady state of the Lindbladian is very close to a thermal state with a temperature close to T , therefore carrying few operator entanglement. Introducing a temperature difference $\Delta T = T_2 - T_1$ is to be seen as a perturbation in the framework of linear response theory presented in section 6.2.3.

In order to find an expression for $\mathcal{L}_{B,T}$, we first diagonalize $\rho_{B,T}$:

$$\rho_{B,T} = V^\dagger d V, \quad (6.20)$$

where d is a diagonal matrix with diagonal elements d_0, d_1, d_2, d_3 . Next we look for the operator $\mathcal{L}_{B,T}^{\text{diag}}$ such that:

$$\mathcal{L}_{B,T}^{\text{diag}}(d) = 0. \quad (6.21)$$

To this aim, it is useful to introduce the Ω -basis. If we denote $\sigma^0 = \sigma^z$, $\sigma^1 = \sigma^z$, $\sigma^2 = \sigma^x$, $\sigma^3 = \sigma^y$, then all two sites superoperators can be expressed as a linear combination of the following operators ² [143, 147]:

$$\Omega^n = \frac{1}{4} \sigma^{n_1} \otimes \sigma^{n_2}, \quad n = n_1 + n_2. \quad (6.22)$$

We have:

$$d = C_0 \Omega^0 + C_1 \Omega^1 + C_4 \Omega^4 + C_5 \Omega^5, \quad (6.23)$$

with $C_0 = d_0 + d_1 + d_2 + d_3$, $C_1 = d_0 - d_1 + d_2 - d_3$, $C_4 = d_0 + d_1 - d_2 - d_3$, $C_5 = d_0 - d_1 - d_2 + d_3$. Then the only non zero elements of $\mathcal{L}_{B,T}^{\text{diag}}$ are given by:

$$(\mathcal{L}_{B,T}^{\text{diag}})_{m,m} = -1, \quad m = 1, \dots, 15, \quad (6.24)$$

$$(\mathcal{L}_{B,T}^{\text{diag}})_{j,0} = \frac{C_j}{C_0}, \quad j = 1, 4, 5. \quad (6.25)$$

In order to go back to the physical basis, it is useful to consider:

$$\text{Tr}(\rho_{B,T} \Omega^n) = \sum_m \rho_m \text{Tr}(\Omega^m \Omega^n) = \frac{1}{4} \rho_n = \sum_m C_m \text{Tr}(V^\dagger \Omega^m V \Omega^n), \quad (6.26)$$

where we have used the fact that $4\text{Tr}(\Omega^n \Omega^m) = \delta_{m,n}$. Therefore we have [143, 147]:

$$\mathcal{L}_{B,T} = R^\dagger \mathcal{L}_{B,T}^{\text{diag}} R, \quad R_{m,n} = 4\text{Tr}(V^\dagger \Omega^m V \Omega^n). \quad (6.27)$$

6.3.2 Diffusion in the tilted field Ising model

We consider the tilted field Ising model:

$$\hat{H} = \sum_i^{N-1} \hat{S}_i^z \hat{S}_{i+1}^z + g_x \sum_i^N \hat{S}_i^x + g_z \sum_i^N \hat{S}_i^z \quad (6.28)$$

with the following parameters: $g_x = 1.4$ and $g_z = 0.9045$. This is the model studied in the previous chapter. In addition to being strongly chaotic for these parameters, it has been shown to display energy diffusion for these parameters [106].

The energy current of this model is given by:

$$\hat{j}_i = h_x (\hat{S}_{i-1}^z \hat{S}_{i-1}^y - \hat{S}_i^y \hat{S}_{i+1}^z). \quad (6.29)$$

We show on Fig. 6.2 that the current as a function of system size behaves indeed diffusively, that is to say $j \propto \frac{1}{L}$.

The diffusion coefficient is then given by:

$$D = - \frac{\langle j \rangle (N - N_B)}{\epsilon_{1+N_B} - \epsilon_{N-N_B}} \quad (6.30)$$

²We choose the following convention: $n = 0 \rightarrow (n_1 = 0, n_2 = 0)$, $n = 1 \rightarrow (n_1 = 0, n_2 = 1) \dots$, $n = 4 \rightarrow (n_1 = 1, n_2 = 0) \dots$

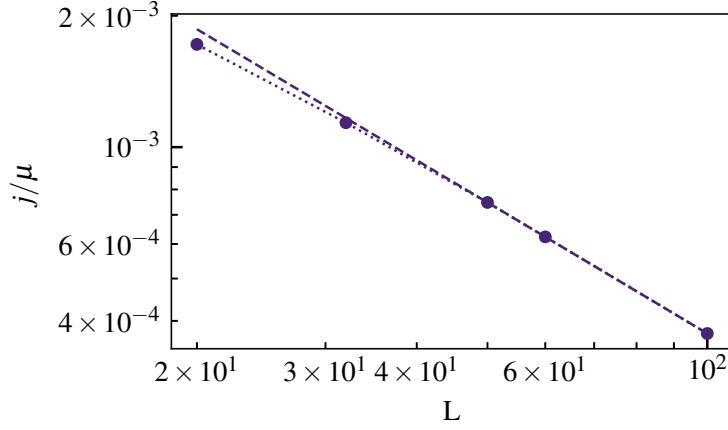


Figure 6.2 Energy current j as a function of system size L for the titled field Ising model (Eq. (6.28)) with $g_x = 1.4$ and $g_z = 0.9045$. The dotted line are the fits of $\log(L) = C + \log(j/\mu)^\alpha$, where we find $\alpha = -0.9975$, in accordance with the expectation of a diffusive behavior.

where ϵ_i denotes the local energy at site i and $i + 1$, i.e. $\epsilon_i = \langle h_{i,i+1} \rangle$.

This model has been investigated in Ref. [149], using the so-called *diffusion assisted operator evolution* (DAOE). In this work, the diffusion coefficient is extracted from the correlation functions $C(t) = \text{Tr}(q_i e^{i\mathcal{L}_{\text{unitary}}t} q_j) / Z$, where q_i are the charge operators, in this case the local energy $h_{i,i+1}$, $\mathcal{L}_{\text{unitary}}$ is the unitary Liouvillian operator and Z is the Hilbert space dimension. In general, this time evolution is impossible to carry out exactly, as entanglement would grow linearly. Nevertheless, only the Pauli strings of length one contribute to the correlation $C(t)$. DAOE proceeds by adding a diffusion term to $\mathcal{L}_{\text{unitary}}$ which decreases the weight of the long Pauli string, as they are unlikely to get shorter in time, and eventually contribute to $C(t)$. Using DAOE, the diffusion coefficient was estimated to $D_{\text{Ising}} = 1.4$. DAOE is believed to be a controlled method, as the coupling with the environment is progressively decreased until the results obtained converge toward a well defined value.

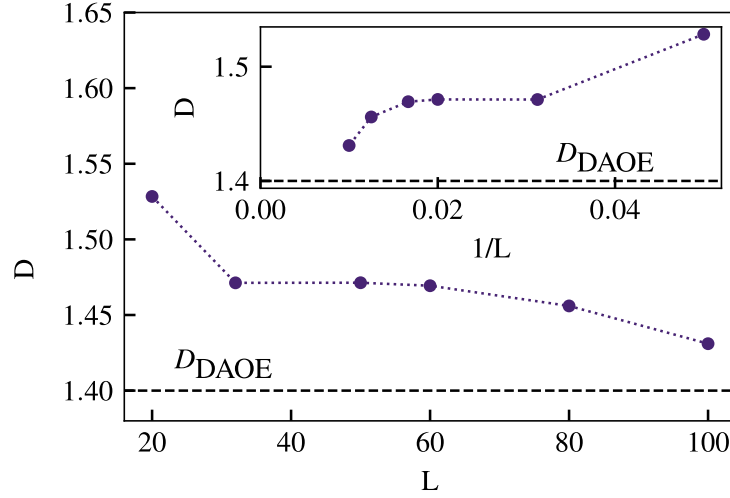


Figure 6.3 Obtained diffusion coefficient for the tilted field Ising model as function of system size. The 4 leftmost and rightmost sites has been excluded from the calculation in order to exclude the boundary effects. The dotted black line represents the diffusion coefficient obtained using the DOAE method. The results were obtained using bond dimension up to $\chi_{\max} = 700$. Inset: diffusion coefficient as a function of the inverse system size. Inset: diffusion coefficient as a function of $\frac{1}{L}$.

6.4 Spin transport

In order to probe spin transport in a chain of L sites, we wish to introduce a spin current throughout the system. To this aim, we pump charges at the boundaries by driving the system with the following Lindblad operators:

$$L_1 = \sqrt{1 + \mu} S_1^+, L_2 = \sqrt{1 - \mu} S_1^-, L_3 = \sqrt{1 - \mu} S_L^-, L_4 = \sqrt{1 + \mu} S_L^+ \quad (6.31)$$

where $S^+ = S^x + iS^y$ and $S^- = S^x - iS^y$ are the raising and lowering operators. For non-zero imbalance μ between the left and the right ends of the chain, the steady state corresponding to this driving will have a non-zero spin current. All the results presented in this chapter were obtained with $\mu = 0.01$.

Note that for $\mu = 0$, $\frac{\mathbb{1}_L}{2L}$ is a steady state of the Lindbladian. Indeed, the action of the baths on the Pauli matrices are: $\mathcal{L}_L(\sigma^x) = \mathcal{L}_R(\sigma^x) = -\Gamma\sigma^x$, $\mathcal{L}_L(\sigma^y) = \mathcal{L}_R(\sigma^y) = -\Gamma\sigma^y$, $\mathcal{L}_L(\sigma^z) = \mathcal{L}_R(\sigma^z) = -2\Gamma\sigma^z$ and $\mathcal{L}_L(\mathbb{1}) = -\mathcal{L}_L(\mathbb{1}) = 2\Gamma\mu\sigma^z$, where \mathcal{L}_L and \mathcal{L}_R are the left and right one spin bath respectively. The linear response of section 6.2.3 framework applies with $\mathcal{L}_0 = \mathcal{L}(\mu = 0)$ and $\mu\mathcal{L}_1 = \mathcal{L}(\mu = 0) - \mathcal{L}(\mu)$ [145]. Furthermore, provided that $\frac{\mathbb{1}_L}{2L}$ is the unique steady state of $\mathcal{L}_0 = \mathcal{L}(\mu = 0)$, $\mathcal{L}(\mu)$ admits a unique steady state which can be formally expressed using equation (6.13) since we have $\mathcal{L}_1(\mathbb{1}) = 0$.

In Ref. [145], under the assumptions that the dynamics in the bulk is unitary, and that some simple corrections are sufficient to describe the dynamics at the boundaries, a relationship was derived between the unitary diffusion coefficient D_{eq} (obtained from the Green-Kubo formalism) and the diffusion coefficient obtained with this method. Note that the diffusion coefficient is

calculated there without the finite size effect correction, i.e. $N_b = 0$ in equation (6.30), as they should be negligible in the thermodynamic limit. Furthermore, as $\langle S_L^z \rangle_{\rho_\infty} - \langle S_1^z \rangle_{\rho_\infty} \approx 2\mu$, the diffusion coefficient is simply expressed as $D = \langle j \rangle / 2N\mu$. Under these various assumptions, an analytical expression was derived:

$$D = \frac{D_{\text{eq}}}{1 + \frac{D_{\text{eq}}}{2\Gamma L}} \approx D_{\text{eq}} \left(1 - \frac{D_{\text{eq}}}{2\Gamma L} \right). \quad (6.32)$$

It was further postulated that in general, one should expect:

$$D = D_{\text{eq}} \left(1 - \frac{\alpha(\Gamma)}{L/l^*} \right), \quad (6.33)$$

where α is an unknown function and l^* is an hydrodynamical length-scale. One important prediction of equation (6.33) is that the deviations between D and D_{eq} should be suppressed in L , so that in the thermodynamic limit, they become identical.

Nevertheless, in practice we have only access to finite systems. In the next sections, we show the dependance of the results with the coupling with the bath Γ for the system sizes we are able to simulate in a reasonable computation time.

6.4.1 The integrable XXZ model

We investigate the integrable XXZ model:

$$\hat{H} = \sum_i \left(\hat{S}_i^x \hat{S}_{i+1}^x + \hat{S}_i^y \hat{S}_{i+1}^y + \Delta \hat{S}_i^z \hat{S}_{i+1}^z \right). \quad (6.34)$$

Starting from the continuity equation:

$$\frac{d\hat{S}_i^z}{dt} = i[\hat{S}_i^z, H] = \hat{j}_i - \hat{j}_{i-1} = \left(\hat{S}_i^x \hat{S}_{i+1}^y - \hat{S}_i^y \hat{S}_{i+1}^x \right) - \left(\hat{S}_{i-1}^x \hat{S}_i^y - \hat{S}_{i-1}^y \hat{S}_i^x \right), \quad (6.35)$$

we identify the current \hat{j}_i :

$$\hat{j}_i = \hat{S}_i^x \hat{S}_{i+1}^y - \hat{S}_i^y \hat{S}_{i+1}^x. \quad (6.36)$$

The diffusion coefficient is then given by:

$$D = -\frac{\langle j \rangle (N - N_b)}{\langle S_{1+N_b}^z \rangle - \langle S_{N-N_b}^z \rangle}. \quad (6.37)$$

It is worthwhile to consider the conversion between *spin units* and *Pauli units*. The model (6.34) often written in term of Pauli matrices [145]:

$$\hat{H}' = 4\hat{H} = \sum_i \left(\hat{\sigma}_i^x \hat{\sigma}_{i+1}^x + \hat{\sigma}_i^y \hat{\sigma}_{i+1}^y + \Delta \hat{\sigma}_i^z \hat{\sigma}_{i+1}^z \right). \quad (6.38)$$

The current is defined as:

$$i[\hat{\sigma}_i^z, \hat{H}'] = \hat{j}'_i - \hat{j}'_{i-1}, \quad (6.39)$$

and we obtain:

$$\hat{j}'_i = 2(\hat{\sigma}_i^x \hat{\sigma}_{i+1}^y - \hat{\sigma}_i^y \hat{\sigma}_{i+1}^x). \quad (6.40)$$

Therefore the diffusion coefficient D' expressed in *Pauli units* is related to the diffusion coefficient D in spin units by the following relation:

$$D' = -\frac{\langle j' \rangle (N - N_b)}{\langle \sigma_{1+N_B}^z \rangle - \langle \sigma_{N-N_B}^z \rangle} = -4 \frac{\langle j' \rangle (N - N_b)}{\langle S_{1+N_B}^z \rangle - \langle S_{N-N_B}^z \rangle} = 4D. \quad (6.41)$$

In Fig. 6.4, we present the current as a function of system size for different couplings with the environment Γ , at the point $\Delta = 1.5$, for which this chain is diffusive [145, 150]. Independently of the coupling with the bath Γ , the current obeys the power law $j \propto \frac{1}{L}$ characteristic of the diffusive behavior.

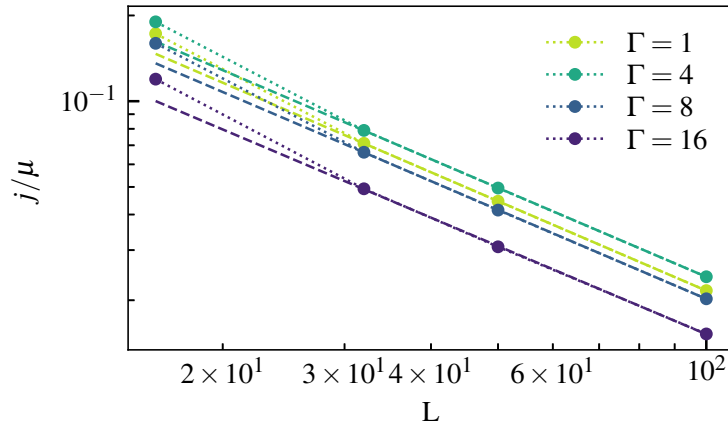


Figure 6.4 Steady state current j divided by the imbalance μ as a function of system size, for different couplings with the environment Γ . The dotted lines are the fits of $\log(L) = C + \log(j/\mu)^\alpha$, where we find $\alpha_{\Gamma=1} = -1.0447$, $\alpha_{\Gamma=16} = -1.0381$, $\alpha_{\Gamma=4} = -1.039$, $\alpha_{\Gamma=8} = -1.0287$ in accordance with the expectation of a diffusive behavior.

In Fig. 6.5, we show the diffusion coefficient as a function of system size for different coupling γ for $\Delta = 1.5$. As this system is integrable, its dynamics and in particular its transport properties can be tackled using the generalized hydrodynamic (GHD) approach [151, 152], which gives information about the long wave-length, long time dynamics of such systems [150]. It rests on the assumption that the system is described locally by a generalized Gibbs ensemble— an extension of the usual Gibbs ensemble which takes into account the extensively many conserved quantities of integrable systems. It also postulates that the parameters of this generalized Gibbs ensemble vary smoothly.

The diffusion coefficient obtained using this approach [150] for $\Delta = 1.5$ is $D = 0.95$. Using the simulation of boundary-dissipative systems, the estimate closest to this value we can find is $D = 0.58$ for $\Gamma = 4$, which is also consistent with the value found in Ref. [145] using the same MPS method. The significant difference between the analytics and the numerics can be explained by the fact that the bath we add to the system breaks integrability and therefore changes the dynamics of the system. We note however the strong dependence with γ , and the non monotonicity of $D(\Gamma)$, which seems to indicate that the assumptions used to derive Eq. (6.33) in Ref. [145] might not be always valid.

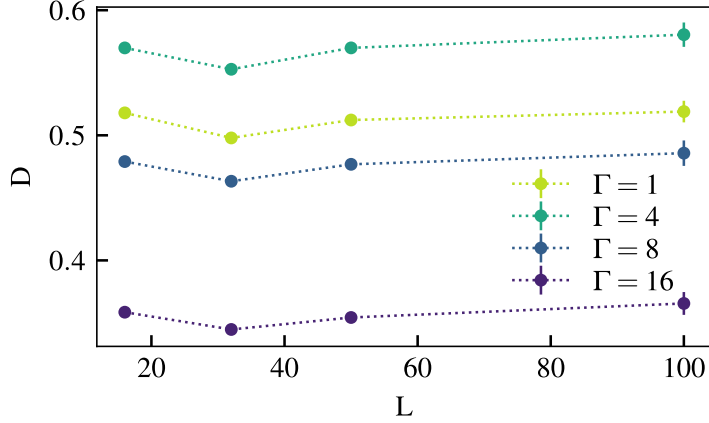


Figure 6.5 Diffusion coefficient as a function of the system size L for different system sizes. The results were obtained using bond dimension up to $\chi_{\max} = 220$. The length of error bar is given by the maximum difference between the diffusion coefficient obtained for the central site with the diffusion coefficient obtained for any other site. The prediction of the method are in clear disagreement with the theoretical predictions of Ref. [150]: $D = 0.95$.

6.4.2 The XX ladder

We study the XX ladder. The legs of the ladder are labeled by index $a = 1, 2$ while the rungs of the ladder are denoted by the usual site index $i = 1, \dots, L$. The Hamiltonian reads:

$$H = \sum_i \sum_a \left(\hat{S}_{i,a}^x \hat{S}_{i+1,a}^x + \hat{S}_{i,a}^y \hat{S}_{i+1,a}^y + J \sum_i \hat{S}_{i,1}^x \hat{S}_{i,2}^x + \hat{S}_{i,1}^y \hat{S}_{i,2}^y \right). \quad (6.42)$$

The local conserved quantity is in this case $\hat{S}_{i,1}^z + \hat{S}_{i,2}^z := \hat{q}_i^z$. The second sum of (6.42) commutes with \hat{q}_i^z , therefore we are left with:

$$\hat{J}_i = \sum_a \left(\hat{S}_{i,a}^x \hat{S}_{i+1,a}^y - \hat{S}_{i,a}^y \hat{S}_{i+1,a}^x \right). \quad (6.43)$$

In Fig. 6.6, we show the diffusion coefficient obtained as a function of system size for different coupling with the bath for different parameters J (the coupling between the rungs of the ladder). This model was investigated using Lanczos exact time evolution [138]. The diffusion coefficient was extracted using the Green-Kubo formula. The value found for $J = 1.0$ was 1.0 while for $J = 1.5$ it was 0.55. Using the DAOE method, very close estimates were found: for $J = 1.0$, $D_{\text{DAOE}} \approx 0.98$ [149] and for $J = 1.5$, $D_{\text{DAOE}} \approx 0.53$ [153]. In both cases, our simulations seem to asymptotically converge in system size towards a value close to these results.

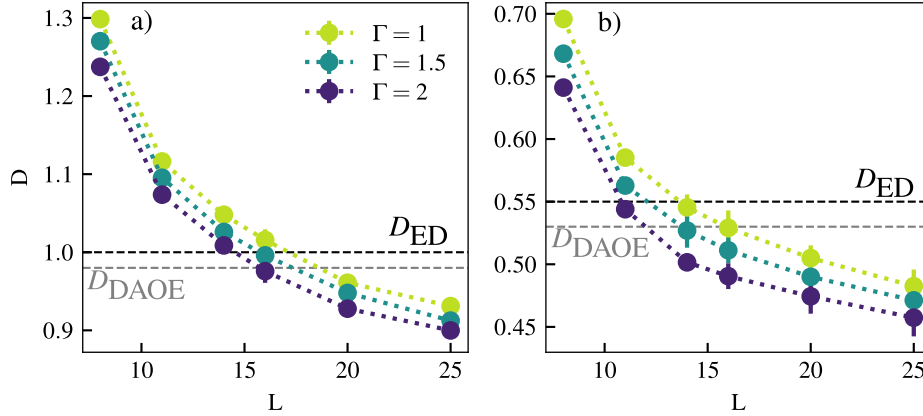


Figure 6.6 Obtained diffusion coefficient for the XX ladder as a function of system size, for different couplings with the environment Γ . The two leftmost and rightmost sites were excluded to avoid boundary effects. Panel a: $J=1.0$, Panel b: $J=1.5$. The black dotted line represents the diffusion coefficient obtained using exact methods in Ref. [138], while the gray dotted line corresponds to the value of D using DAOE [153]. The results were obtained using bond dimension up to $\chi_{\max} = 300$

6.5 Conclusion

We have examined different systems using the method introduced in Ref. [143], that we have compared with other approaches. We have seen that in the integrable case it yields results incompatible with theoretical calculations presented in Ref. [150]. In other models, it gives estimates of the diffusion coefficient D close to the one obtained with other numerical calculations, using completely different assumptions. However, we have shown that the diffusion coefficient obtained depends on the coupling with the environment. Although this dependence has been conjectured to vanish in the thermodynamic limit, one can in practice only access finite system sizes. Furthermore, the polynomial convergence time in system size [154] limits the extent of the simulations. While the precise dependence of D with respect to the couplings has been calculated exactly in one particular exactly solvable case, it would be desirable to obtain a more general relationship.

7 Identifying correlation clusters in many body localized systems

Most of the content of this chapter can also be found in a previous publication of the author [2]. Text and figures have been adjusted to fit into the context of the thesis.

7.1 Introduction

Initiated by the seminal work of Anderson [155], many-body localization (MBL) is now understood as a dynamical quantum phase of matter [24, 156]—defined by the properties of its highly excited many-body eigenstates. In particular, the entanglement of eigenstates in the MBL phase has been found to obey an area law even at finite energy densities [157–159] and to violate the eigenstate thermalization hypothesis [18, 19], due to the existence of quasi-local conserved quantities [56, 60, 159–161]. The concept of MBL has since proven central to the understanding of several aspects of non-equilibrium physics. For instance, MBL is essential to stabilise various emergent Floquet phases of matter, such as discrete time crystals [162, 163].

The study of MBL has been driven by large scale numerics and experimental advances in the control of isolated quantum systems. These efforts have identified characteristic properties of MBL, such as the unbounded logarithmic growth of entanglement following a global quench [61, 63, 164–167]—which distinguishes it from Anderson localization (AL) where the entanglement saturates—and the presence of an eigenstates transition to an ergodic phase at finite disorder strengths [54, 55, 168–171]. A slow growth of entanglement-related quantities has since been observed experimentally for small system sizes in Rydberg atomic systems and in superconducting circuits [172, 173]. However, extracting the entanglement entropy experimentally generically requires high fidelity measurements of a number of non-local observables that scale exponentially with system size. This makes experimental measurements of the entanglement entropy prohibitively difficult for large systems. In cold atom setups, large systems and long times can be reached, even in 2D, and clear signals of MBL has been detected in local measurements [25–27].

In spite of the recent progress, the MBL transition is still not fully understood. While we have powerful numerical and analytical techniques that allow us to investigate the slightly entangled eigenstates deep in the MBL phase [60, 160, 174–177], the transition to the ergodic phase is much harder to study. Phenomenological renormalization group (RG) approaches have emerged as promising theoretical description of the transition [68, 73–77]. Although the assumptions behind the various models differ, most of them describe the MBL transition in term of the proliferation of “thermal blocks” versus “insulating blocks”, i.e., regions of the spin chain that look locally thermal or fully localized, respectively. However, the interpretation of these approaches rest

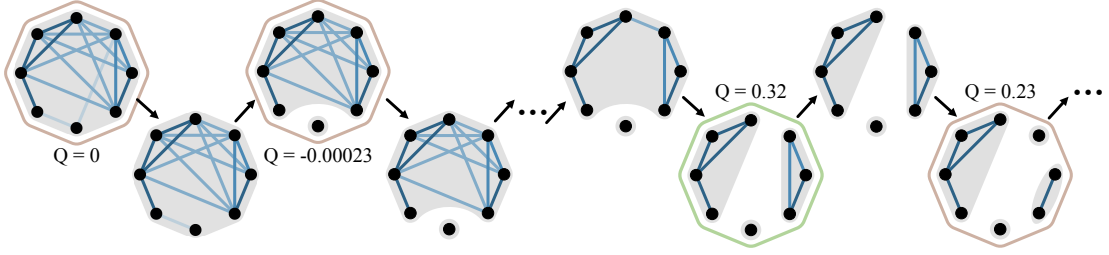


Figure 7.1 Schematic description of our graph theory approach using an example of the mutual information matrix M_{ij} . The full graph has zero modularity (see Eq. (7.13)). We then successively remove the weakest edges until the graph is broken into a larger number of clusters. These steps where a new clustering is obtained are saved and are indicated by a ring around them and the value of their modularity is given. In this example we find a very low modularity of $Q = -0.00023$ for the first clustering, indicating no community structure. The next new clustering occurs after removing several bonds (not all shown) and has a relatively high modularity of 0.32, which turns out to be the highest obtained for this example. We identify this clustering as the physical one and is indicated by a green ring in the figure. The next steps of the decomposition yields four clusters with a modularity of $Q = 0.23$, smaller than in the last step, indicating community structure of a lower quality. The rest of the procedure was not represented here, but the modularity was decreasing at each new step.

on phenomenological assumptions which could bias the results. Indeed, most models assume that each of these blocks is local, although the existence of sparse thermal blocks spanning the whole chain has also been suggested [76]. These RG studies suggest that the MBL transition is of Kosterlitz-Thouless (KT) type with a delocalization mechanism called *avalanche instability*, also sometimes referred as *quantum avalanche* [68, 69].

Since RG approaches provide a clear mechanism for the transition and allow for a prediction of a scaling behavior close to the transition, it is desirable to have a clear prescription in order to identify these “blocks” from states obtained numerically or experimentally. The first numerical validation of this picture in a microscopic model has been provided in Ref. [178], where it was proposed to identify these “blocks” by finding what they denote as *entanglement clusters*. These are clusters of spins that are more strongly entangled with each other than the rest of the system. A numerical investigation using exact diagonalization for small systems revealed that the average block size of these entanglement clusters is indeed consistent with the RG analysis of the transition. Entanglement entropy is paramount for this approach, but it is costly to calculate both numerically and from experimental measurements.

Motivated by that work, we propose an approach in which we identify these structures in MBL systems in a scalable way that is relevant for efficient matrix-product state (MPS) based simulations and accessible in experiments. We are focusing on the XXZ spin-chain in the presence of a disordered z -directed field defined by the Hamiltonian

$$\hat{H} = -J \sum_i \left[\hat{S}_i^x \hat{S}_{i+1}^x + \hat{S}_i^y \hat{S}_{i+1}^y + \Delta \hat{S}_i^z \hat{S}_{i+1}^z + h_i \hat{S}_i^z \right]. \quad (7.1)$$

The disordered field h_i is sampled uniformly from the interval $[-W, W]$, where $W \geq 0$ controls the strength of the disorder. We consider the Anderson insulator at $\Delta = 0$ as well as the Heisenberg model at $\Delta = 1$, which is believed to exhibit an MBL transition at W_C estimated between 2.7 and 3.8 [55, 168, 171, 179–181].

In this chapter, we present practical tools to efficiently identify the ergodic clusters within MBL eigenstates using pairwise correlations by applying methods originally developed in the context of graph theory [182–185]. We validate our approach in two ways: First, we show that the two site mutual information (TSMI) is a useful proxy for analysing the structure of MBL eigenstates. Second, we demonstrate in Sec. 7.7 that our clustering algorithm applied during time evolution—using the TSMI as well as the pairwise connected correlation functions in the σ_z basis—indicates the logarithmic spreading of entanglement.

7.2 From correlations to graph theory

The quantum mutual information of two subsystems A and B is a correlation measure defined as:

$$I(A; B) = S(A) + S(B) - S(A \cup B), \quad (7.2)$$

where $S(A) = -\text{Tr}[\rho_A \log(\rho_A)]$ is the von Neumann entanglement entropy for the subsystem A . The TSMI corresponds to the case where subsystems A and B each consist of a single site, and in this case we denote it $I(i; j)$ for two sites i and j . The TSMI captures the classical and quantum correlations between two sites, and has already been shown to be a relevant probe of localization [186]. In particular, spatial fluctuations in the TSMI grow logarithmically under non-equilibrium dynamics, mirroring the entanglement entropy [186]. Another useful quantity to study quantum correlations is the (connected) correlation function $C(\hat{O}_A, \hat{O}_B)$ of two operators \hat{O}_A and \hat{O}_B :

$$C(\hat{O}_A, \hat{O}_B) = \langle \hat{O}_A \hat{O}_B \rangle - \langle \hat{O}_A \rangle \langle \hat{O}_B \rangle \quad (7.3)$$

where $\langle \hat{O} \rangle$ denotes the expectation value of the operator \hat{O} . Although TSMI takes into account all pairwise correlations [187, 188], it is less accessible in experiments than certain correlation functions. In this chapter we introduce tools borrowed from the field of graph theory to extract what we call *correlation clusters*, in analogy to Ref. [178]. This provides an efficient method for studying of correlations in MBL systems. Graph theory has been used in the past to detect quantum phase transition in equilibrium settings [189–191]. Recently, another work identified the so called “ergodic bubbles” (i.e. regions of space where the expectation values of local operators look thermal) using neural networks techniques [192].

Our starting point is to construct a matrix M_{ij} containing the correlations between site i and j , and to interpret it as an adjacency matrix for a weighted graph as illustrated in Fig. 7.1. The vertices of this graph are the lattice sites of our system and the bonds connecting them are weighted by the matrix element M_{ij} between that pair. Our goal to find the correlation clusters in the state translates to finding “communities” within this graph. We consider $M_{ij} = I(i; j)$ in the case of eigenstates, to which we add $M_{ij} = C(\hat{\sigma}_i^z, \hat{\sigma}_j^z)$ for dynamics.

The task of finding communities has received considerable attention in the field of graph theory [182–185]. This is usually achieved by splitting the graph into disjoint sets of vertices which we refer to as *clusters*. A given decomposition of a graph into clusters is referred to as a *clustering*. The goal is to find a clustering that is optimal by some well-defined measure, in our case the *modularity*, which will be the subject of the next section.

7.3 The modularity, a quality measure of the partition of a graph

We would like to have a quantity enabling us to judge the quality of a graph clustering in order to compare different clusterings. The procedure by which we obtain a limited number a promising clusterings will be described in the next section. In order to achieve this, a naive trial would be evaluate the fraction of weighted edges connecting vertices belonging to the same community over the sum of all weights. If M is the adjacency matrix, and c_i the community in which vertex i belongs to, this ratio can be expressed as:

$$R = \frac{1}{2m} \sum_{ij} M_{ij} \delta(c_i, c_j) \quad (7.4)$$

where $m = \frac{1}{2} \sum_{ij} M_{ij}$ and $\delta(c_i, c_j)$ ensures that vertex i and j are in the same community. Although any good clustering of a given graph should yield a high value of R , this quantity can not be useful to gather information about the community structure. Indeed considering only one community containing all the vertices would result in a maximal value of $R = 1$ [182]. In order to overcome this limitation, the formula of R has been modified by following the idea that a random graph is not expected to present a community structure. A good measure of quality would be obtained when comparing the fraction of weights belonging to the same community to the one we would have if the weights had been assigned randomly. This translate into the following expression for the *modularity* [182, 184, 185] of a graph partition:

$$Q = \frac{1}{2m} \sum_{ij} (M_{ij} - P_{ij}) \delta(c_i, c_j) \quad (7.5)$$

where P_{ij} is the expected adjacency matrix of the random graph which shares the same structural properties as the original graph of interest without presenting the same community structure. This random graph is also sometimes called the “Null model”. In order to determine the matrix P , we must first specify a choice for the null model. Let us define the *degrees* k_i : $k_i = \sum_j M_{ij}$. Since the null model has to be similar to the original graph, we impose that the vertex of the random graph has to have the same *degrees* than the original one, that is to say:

$$\sum_j M_{ij} = \sum_j P_{ij} = k_i. \quad (7.6)$$

In other words, every vertex of the null model shares as much weight with the rest of the system than the graph of interest, although the connections between vertices are assigned randomly. On average, the vertex i and j will be connected by a edge of weight $P_{ij} = \frac{k_i k_j}{2m}$ [185], where $m = \frac{1}{2} \sum_{ij} M_{ij}$, yielding [184]:

$$Q = \frac{1}{2m} \sum_{ij} \left(M_{ij} - \frac{k_i k_j}{2m} \right) \delta(c_i, c_j), \quad (7.7)$$

where $\delta(c_i, c_j)$ is 1 if sites i and j are connected for the given clustering and 0 if they are not. We can see that this measure solves the issue initially encountered since the partition containing all vertices have a zero modularity. A value of modularity close to zero means that the partition is not better than a random one while a value close to one indicate a strong community structure.

7.4 Scaling of the modularity with system size

For a system where the optimal decomposition yields N clusters, the modularity can be written in the following way [193]:

$$Q = \sum_{i=1}^N \frac{e_i}{m} - \left(\frac{d_i}{2m} \right)^2 \quad (7.8)$$

where the sum runs over the clusters. In the formula above, d_i denotes the total degree of nodes in the cluster i : $d_i = \sum_j k_j \delta(c_j, c_i)$ in the notation of the main text, e_i is the number of edges in cluster i and m is, as in the main text, the total number of edges. Defining $\langle e \rangle = \frac{1}{N} \sum_i e_i$ and $\langle d \rangle = \frac{1}{N} \sum_i d_i$ we obtain:

$$Q = \sum_{i=1}^N \frac{\langle e \rangle}{m} - \frac{\langle d^2 \rangle}{(2m)^2} \quad (7.9)$$

We now introduce the quantity $\langle e^{out} \rangle$, which is the average weight going out of each cluster:

$$\langle e^{out} \rangle = \frac{1}{N} \sum_i \sum_j M_{i,j} (1 - \delta(c_i, c_j)). \quad (7.10)$$

Using the fact that $\langle d \rangle = \langle 2e \rangle + \langle e^{out} \rangle$ and $m = \frac{1}{2} N \langle d \rangle$, we obtain:

$$Q = \sum_{i=1}^N \frac{\langle e \rangle}{\frac{N}{2} (2\langle e \rangle + \langle e^{out} \rangle)} - \frac{\langle (2e + e^{out})^2 \rangle}{N^2 (2\langle e \rangle + \langle e^{out} \rangle)^2} \quad (7.11)$$

Finally, noting that the number of clusters N is proportional to the system size, we recover the scaling of the main text:

$$Q = \frac{\langle e \rangle}{\langle e \rangle + \langle e^{out} \rangle / 2} - \frac{1}{N} \frac{\langle (2e + e^{out})^2 \rangle}{(2\langle e \rangle + \langle e^{out} \rangle)^2} \quad (7.12)$$

7.5 Correlation clusters

7.5.1 A graph theory algorithm to obtain correlation clusters

Inspired by the well established Girvan-Newman approach [182, 184], we propose the following three steps procedure, shown schematically in Fig. 7.1, for finding the optimal clustering from the correlation matrix M_{ij} :

1. Successively remove the weakest bonds of the graph.
2. When the removal of a bond results in two parts of the graph becoming disconnected, we store the new clustering. This clustering corresponds to the set of clusters, where a cluster contains sites that are connected to each other.

3. Repeating steps 1 and 2 appropriately, we eventually end up with a completely disconnected graph, and have stored a sequence of different clusterings. For each of these stored clusterings we then compute the *modularity*:

$$Q = \frac{1}{2m} \sum_{ij} \left(M_{ij} - \frac{k_i k_j}{2m} \right) \delta(c_i, c_j), \quad (7.13)$$

where $k_i = \sum_j M_{ij}$, and $m = \frac{1}{2} \sum_{ij} M_{ij}$. The delta function $\delta(c_i, c_j)$ is 1 if sites i and j are connected for the given clustering and 0 if they are not. The modularity takes values $Q \in [-1/2, 1]$ and quantifies how good the clustering is, with close to 1 corresponding to a good clustering, or “community structure”. We select the correct clustering as the one with the highest modularity.

The first step differs from the original Girvan-Newman approach. While in our case, we are guided by the physical intuition that two correlation clusters are only connected by weak bonds, Girvan and Newman use a quantity called *edge-betweenness* to assess which bonds are most likely to link separated communities [183].

7.5.2 Comparison between “entanglement clusters” and “correlation clusters”

In Ref. [178], the authors introduce a procedure aimed at finding “entanglement clusters”. Their algorithm is based on the *normalized mutual information* of subsystem A and B defined as:

$$i(A; B) = \frac{I(A; B)}{\min(n_A, n_B)}, \quad (7.14)$$

where n_A and n_B are the number of sites contained in subsystems A and B respectively, and $I(A; B)$ is the mutual information defined in equation (7.2). The idea behind this algorithm is to successively split the system into bipartitions, in such a way that the normalized mutual information between the splitted parts is minimal at each step. Furthermore, only the “periodic partions” are considered: for example if one wishes to decompose the subsystem containing sites (2,3,5,8,9), the partitioning (9,2,3) (5,8) would be considered, while (3,8) (2,5,9) would not. An example of such a partitioning procedure is shown in Fig. 7.2. First, the normalized mutual information between all the bipartitions which respect the ordering of the spins (with periodic boundary conditions) is calculated. The bipartition displaying the lowest normalized mutual information is selected. The procedure then apply to each of the subsystem hence selected. This procedure reveals the structure of the state until all sites are isolated from each other. Nevertheless, in order to select the optimal “entanglement cluster”, the decomposition stops once the maximal normalized mutual information obtained is higher than the one found in the first step. In the example of Fig. 7.2, the procedure would stop after the first decomposition, yielding only two clusters. In Fig. 7.2, we show the clustering of a typical MBL eigenstate using the approach of Ref. [178] (left panel) and compare it to our approach (right panel). The similarities between the “entanglement clustering” and the “correlation clustering” are striking. The successive decompositions of the system are almost identical. A similar degree of similarity between both approaches for the MBL states was found in all the examples that we examined. Furthermore, in this particular example, both approaches select the same clustering as optimal. This is often the case, although some minor differences can be sometimes observed. In general, we find that a clustering with a high modularity corresponds to successive bipartitions with low

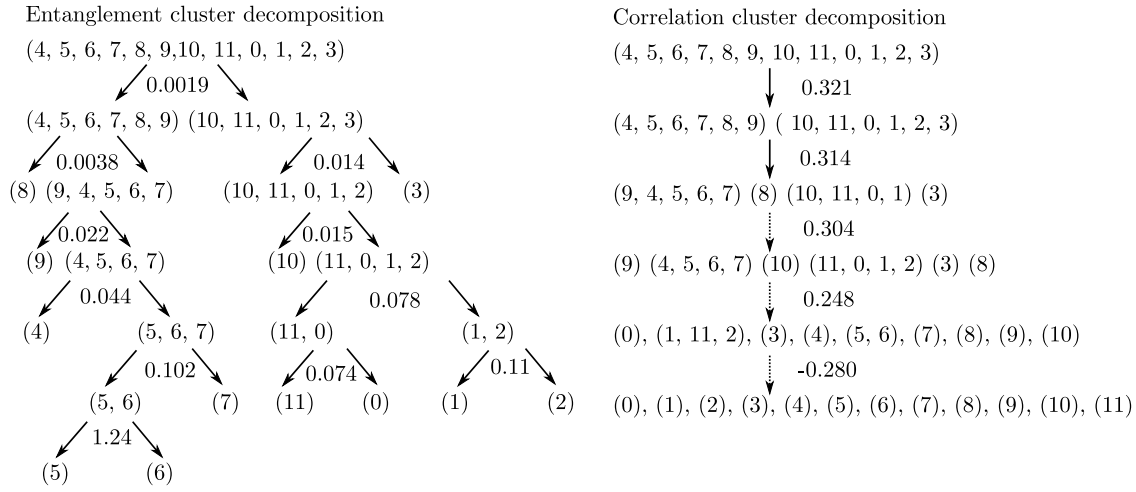


Figure 7.2 Comparison between a typical example of clustering obtained by applying the “entanglement clustering” procedure (left) and the “correlation clustering” (right) applied to the same state. The state chosen to apply these two procedures is an excited eigenstate of the Hamiltonian (7.1) for $L = 12$, $W = 5$ and $\Delta = 1$. On the left panel, we show the tree structure resulting from the entanglement clustering, where the sites belonging to the same cluster are listed between parentheses, while the internal mutual information can be read in the line below between the arrow. For example, the two first lines should be read as follows: the system containing sites (4, 5, 6, 7, 8, 9, 10, 11, 0, 1, 2, 3) splits up into the clusters (4, 5, 6, 7, 8, 9) and (10, 11, 0, 1, 2, 3), with associated normalized mutual information is equal to 0.0019. On the right panel, we show the dendrogram resulting from the correlation clustering procedure: the sites between parentheses belong to the same cluster, while the number on the left of the arrow corresponds to the modularity Q . A dotted arrow indicates that we have omitted to represent one or several intermediary steps.

normalized mutual information. Conversely, when a clustering involves bipartitions which split two parts with high normalized mutual information, the associated modularity is usually low. While so far we have only considered a particular example of decomposition, in the next section, we will look at the average number of clusters, and show that we find results similar to Ref. [178].

7.6 Correlation clusters in eigenstates

We will now focus on the clustering in mid-spectrum eigenstates for the Hamiltonian Eq. (7.1) for different values of the disorder strength. We analyse the structure of the optimal clustering for the eigenstates across the MBL-ergodic phase transition, using the TSMI to define the graph M_{ij} . It has been shown in earlier studies that the number of entanglement clusters can be taken as a relevant scaling parameters for the MBL transition [178]. In order to validate our graph clustering approach, we perform a similar scaling analysis. However, we can not directly apply our graph theory approach on the ergodic side of the phase transition. Indeed, if the system is ergodic, then we would expect the mutual information to be uniform on average between all pairs of sites [186]. In this case, the optimal clustering is a single cluster containing all sites. However, the algorithm presented in section 7.5.1 will instead choose a clustering with very low modularity. In order to analyze the phase transition, we need to first detect the ergodic states, and each time we do, bypass the graph theory algorithm. We present two different strategies to

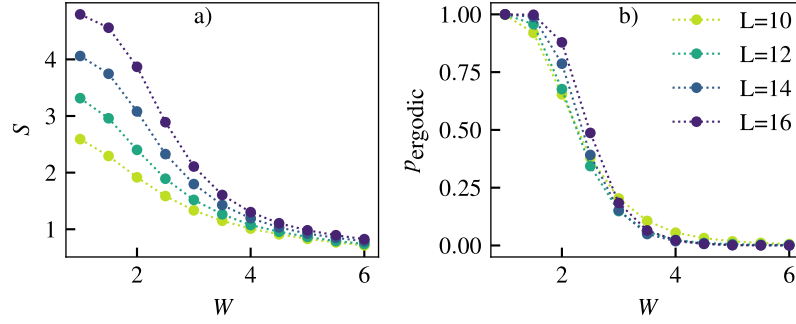


Figure 7.3 Detection of the ergodic/MBL phase transition using entanglement entropy: we measure the maximum entanglement entropy for each state obtained using full diagonalization of the XXZ Hamiltonian. We identify ergodic states when the maximum entanglement entropy is greater than 60% of the Page value. a) Average maximum entanglement as a function of disorder for different system sizes. b) Ratio of ergodic states detected p_{ergodic} as a function of disorder W .

achieve this: one based on bipartite entanglement entropy and the other entirely based on graph theory. Both approaches give the same results. In both cases, we select 50 eigenstates from the middle of the spectrum of 700 disorder configurations and then apply the algorithm outlined in the previous section to extract the average number of clusters in the optimal clustering, while applying the “ergodic filters” described in the two following sections.

7.6.1 Exploring the many-body localized phase transition based on graph theory and entanglement entropy

As we have seen in section 2.4, ergodic eigenstates are characterized by very high von Neumann entanglement entropy, following volume law. Deep into the ergodic phase, their maximum entanglement entropy (reached in the middle of the chain) is slightly lower than the Page value [47], due to finite size corrections [58, 194]. Therefore, detecting the ergodic eigenstates based on entanglement entropy is very natural. Based on this considerations, when the maximum entanglement entropy is greater than a significant fraction α of the Page value [47] (in practice $\alpha = 60\%$), we bypass our algorithm and select the whole system as a cluster. In Fig. 7.3, we show the average maximum of entanglement entropy in the chain, as well as the ratio of ergodic states detected following this scheme. At low disorder ($W = 1$), all the states are ergodic, while p_{ergodic} goes to zero for $W > 4$. In Fig. 7.4, we present the average number of clusters divided by system size n/L , obtained using the entanglement criterion that we just presented to detect the ergodic states exhibiting a single cluster. The critical disorder W_c is located at the crossing of the curves at $W = 3.8$, in agreement with Ref. [178] (see inset of Fig. 7.6). The data collapses convincingly with scaling $n/L = f((W - W_c)L^{1/\nu})$ with parameter $\nu = 1.26$, taken from Ref. [178]. It was pointed out that this scaling is consistent with theoretical studies, where a Harris-type bound on the exponents has been derived [80]. We find that the scaling does not depend on the fraction α of the Page value used to set the entanglement threshold. Note that although bipartite entanglement entropy is extremely challenging to measure in experiment, it is easily accessible both in ED calculations as well as in MPS calculations (see section 4.1.2 for details about obtaining bipartite entanglement using MPS).

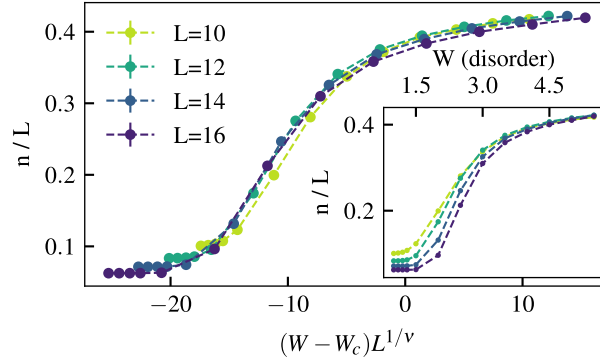


Figure 7.4 Scaling collapse of the average number of clusters n divided by system size as a function of the disorder obtained using our modified Girvan-Newman approach. For the collapse, the disorder strength was rescaled to take the form $(W - W_c)L^{1/\nu}$ with $W_c = 3.8$ and $\nu = 1.26$. An eigenstate with bipartite entanglement entropy in the middle of the chain bigger than 0.6 times the page value was considered to be ergodic and therefore was counted as one cluster, independently of the result of the graph theory approach. Inset: average number of clusters n divided by system size as a function of disorder strength W

7.6.2 Exploring the many-body localized phase transition based only on graph theory

We have confirmed in the last section the relevance of the graph theory approach for understanding the MBL phase transition. However, it is desirable to detect the phase transition purely from graph theory considerations. Since the quality of the community structure is low in the ergodic phase (see Fig. 7.5, panel a), and higher in the MBL phase, a first idea would be to choose a modularity threshold Q_{th} below which the state is considered ergodic. However, since our numerics are performed on finite system sizes up to $L = 16$, the modularity will be affected by finite size effects that we must take into account in Q_{th} . To understand these effects we consider states deep in the MBL phase where we can make statements about the optimal clustering. In particular, MBL eigenstates are simultaneous eigenstates of an extensive number of exponentially localized l -bits with a characteristic localization length [56]. This means that the structure of the clustering should be independent of systems size, so long as it is sufficiently large compared to the localization length. As explained in section 7.4, this actually results in a system size dependence of the modularity for similar clusterings. To account for this we use the system size dependent threshold

$$Q_{\text{th}}(L) = \alpha \left(1 - \frac{a}{L}\right), \quad (7.15)$$

where $\alpha \in [0, 1]$. In practice we obtain the coefficient a by fitting $Q(W = 6, L)$, where $W = 6$ is the maximum disorder strength considered in our scaling analysis and is located deep within the MBL phase. In the main text, we present results for the overall cutoff parameter $\alpha = 0.3$. We show in Appendix 8 that as long as α gives the correct clustering behavior deep in the MBL and ergodic phases, the scaling collapse is not sensitive to the specific choice of this coefficient. We decide to bypass the graph theory algorithm by setting a threshold Q_{th} below which the states yielding a modularity $Q < Q_{\text{th}}$ are considered as ergodic.

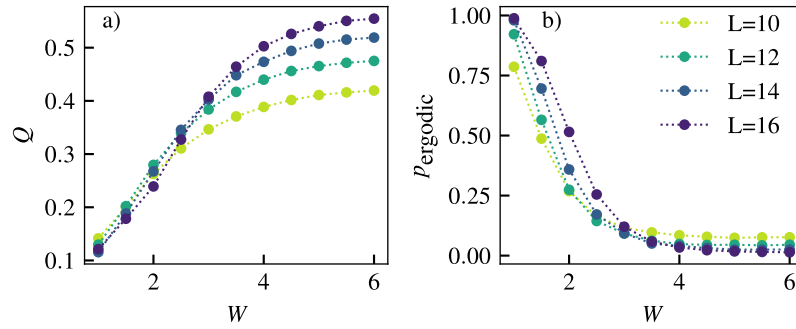


Figure 7.5 Detection of the ergodic/MBL phase transition using entanglement entropy: when $Q_{\text{th}} = \alpha(1 - a/L)$ with $\alpha = 0.3$ and $a = 3.59$, the state is considered as fully ergodic. a) Average modularity as a function of disorder for different system sizes. b) Ratio p_{ergodic} of the ergodic states as a function of disorder W .

We present in the panel a of Fig. 7.5 the modularity as a function of disorder. As expected, the modularity depends strongly on system size deep in the MBL phase, while it is almost system size independent in the ergodic phase. Furthermore, in panel b of Fig. 7.5, we show the ratio p_{ergodic} of the number of ergodic states divided by the total number of states calculated with ED. The behavior is almost the same as in the case of the entanglement criterion of the last section. The average number of correlation clusters n as a function of disorder is shown in Fig. 7.6 for different system sizes. As in the case of the entanglement criterion of the last section, we identify the critical disorder strength W_c at the crossing of the curves and obtain $W = 3.8$, in agreement with Ref. [178] (see inset of Fig. 7.6). The data collapses convincingly with the same scaling as before.

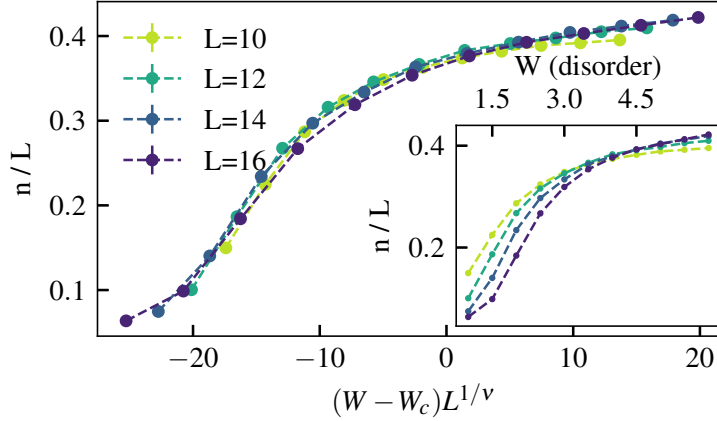


Figure 7.6 Scaling collapse of the average number of clusters n divided by system size as a function of the disorder obtained using our modified Girvan-Newman approach. For the collapse, the disorder strength was rescaled to take the form $(W - W_c)L^{1/\nu}$ with $W_c = 3.8$ and $\nu = 1.26$. When the modularity was lower than $Q_{\text{th}} = \alpha(1 - a/L)$ with $\alpha = 0.3$ and $a = 3.59$, the state was considered as fully ergodic and made of only one cluster. The coefficient a has been fitted to take into account the finite size effects at $W = 6$, according to the finite size scaling: $Q_L = q - \frac{a}{L}$ of the average modularity Q_L obtained for system size L . Inset: average number of clusters n divided by system size as a function of disorder strength W .

7.6.3 Variational methods for obtaining highly excited states of many-body localized Hamiltonians

We have seen in section 3.2.1 that all the eigenstates of a MBL Hamiltonian follow area law. Therefore, there exist a efficient representation of these states with a MPS of finite bond dimension.

In order to target directly the excited states, one approach consists in minimizing the variance, that is $(H - E_{\text{target}})^2$, which can be efficiently represented as a MPO, and where E_{target} is the eigenenergy of the eigenstate that we wish to obtain. This method has been applied with success in some cases [195], however in the MBL case, the exponentially small in system size level spacing renders this approach impractical. Indeed, taking the square of the Hamiltonian further reduces the level spacing.

Another straight forward idea is to modify the DMRG sweep by finding at each step the eigenstate of the effective Hamiltonian (4.22) closest to the energy E_{target} instead of the ground state. However, this approach fails dramatically [174], as the algorithm tends to select superpositions of several eigenstates in the nearby energy of E_{target} . The so-called *exact state DMRG* (ES-DMRG) [175] circumvents this problem. During the sweep n_{sweep} , at each site i , one finds the eigenstates which corresponding eigenvalue $E_i^{n_{\text{sweep}}}$ is the closest to the energy $E_{i-1}^{n_{\text{sweep}}}$ obtained at the last step of the algorithm. The algorithm progressively converges as all the energies $E_i^{n_{\text{sweep}}}$ tend to be equal to an energy of the Hamiltonian for n_{sweep} large enough.

However, this approach still relies on targeting energies, which due to the small level spacing, could easily lead to a superposition of states in nearby energies. *DMRG-X*, a conceptually related approach, aims at converging toward a 1-bit configuration instead of toward a given energy. One initiates the algorithm with a random product state. The convergence in 1-bit configuration is achieved by finding the eigenstate of the effective Hamiltonian maximizing the overlap:

$$\left(\begin{array}{c} \tilde{\Theta}_2^i \\ \Theta_2^i \end{array} \right) \quad (7.16)$$

where Θ_2^i is the two site wavefunction tensor of the current state of the algorithm while $\tilde{\Theta}_2^i$ is the eigenstate of the effective Hamiltonian $H_{\text{eff},2}^i$. Note that this algorithm is almost identical to ES-DMRG, at the exception that the overlap (7.16) is minimized instead of $|E_i^{n_{\text{sweep}}} - E_{i-1}^{n_{\text{sweep}}}|$. Although at each step the algorithm maximizes the “local overlap”, it does not necessarily converge towards the eigenstate which has the largest overlap with the initial state. In order to be able to use somewhat larger bond-dimensions, once the algorithm has sufficiently converged (meaning that the energy of the state does not change significantly between two different steps of the sweep), one can use a shift-inverse method to find a few eigenstates of the effective Hamiltonian around the targeted energy, and to select the eigenstate which minimizes the overlap (7.16). The effective Hamiltonian can be represented as a sparse matrix, avoiding a costly exact diagonalization.

Algorithm 1 The ES-DMRG algorithm

```

1:  $n_{\text{sweep}} = 0$ 
2:  $E^1 \leftarrow E_{\text{target}} + 10\epsilon_{\text{conv}}$ 
3:  $E^0 \leftarrow E_{\text{target}}$ 
4:  $E \leftarrow E_{\text{target}}$ 
5: while  $|E^{n_{\text{sweep}}} - E^{n_{\text{sweep}}-1}| > \epsilon_{\text{conv}}$  do
6:    $n_{\text{sweep}} \leftarrow n_{\text{sweep}} + 1$ 
7:   for  $i=1, 2, \dots, L-2, L-1, L-2, \dots, 2, 1$  do
8:     Get  $H_{\text{eff}}$ 
9:     Diagonalize  $H_{\text{eff}}$ , and find the eigenstate  $v_j$ ,  $H_{\text{eff}}v_j = e_j v_j$ , such that  $|e_j - E|$  is
10:    minimum ▷ Alternatively, apply the Lanczos algorithm to  $(H_{\text{eff}} - E)^2$ 
11:     $\Theta_{i,i+1}^2 \leftarrow v_j$  and  $E \leftarrow e_j$ 
12:    Perform SVD
13:   end for
14:    $E^{n_{\text{sweep}}} \leftarrow E$ 
15: end while

```

7.6.4 Structure of individual eigenstates obtained via matrix-product states

After focussing on the average number of clusters, we will now investigate the structure of individual eigenstates using the clustering algorithms. The TSMI matrix M_{ij} is shown in Fig. 7.7 for a single mid-spectrum eigenstate in an $L = 50$ system with disorder strength $W = 12$ —obtained using DMRG-X [174]—and compared against the bipartite von Neumann entanglement entropy for cuts along different bonds. Here we can see that the localized state is

Algorithm 2 The DMRG-X algorithm

```

1:  $\psi \leftarrow \psi_{\text{init}}$  ▷ Initialize the algorithm with a random product state  $\psi_{\text{init}}$ 
2:  $E \leftarrow \langle \psi_{\text{init}} | H | \psi_{\text{init}} \rangle$ 
3: while  $|\langle \psi | H^2 | \psi \rangle - \langle \psi | H | \psi \rangle^2| > \epsilon_{\text{conv}}$  do
4:   for  $i=1, 2, \dots, L-2, L-1, L-2, \dots, 2, 1$  do
5:     Get  $H_{\text{eff}}$ 
6:     Get  $\Theta_{i,i+1}^2$ 
7:     if  $E$  is still varying significantly then
8:       Diagonalize  $H_{\text{eff}}$ , and find the eigenstate  $v_j$ ,  $H_{\text{eff}}v_j = E_jv_j$ , such that  $|\langle v_j | \Theta_{i,i+1}^2 \rangle|^2$ 
9:       is maximum (see Eq. (7.16))
10:    else
11:      if The variation of  $E$  is smaller than a certain threshold then
12:        Apply a shift inverse Lanczos to  $H_{\text{eff}}$ , finding the  $n$  eigenstates closest to  $E$ ,
13:        and find the eigenstate  $v_j$ ,  $H_{\text{eff}}v_j = E_jv_j$ , such that  $|\langle v_j | \Theta_{i,i+1}^2 \rangle|^2$  is maximum
14:        (see Eq. (7.16))
15:      end if
16:    end if
17:     $E \leftarrow e_j$ 
18:     $\Theta_{i,i+1} \leftarrow v_j$ 
19:    Perform SVD
20:   end for
21: end while

```

decomposed into a sequence of small clusters (red boxes) and there are only weak off-diagonal (long-range) correlations in the matrix. However, we observe several examples of clusters that contain sites that are not nearest neighbors, a phenomenon which, following Ref. [178], we refer as “leapfrogging” (green and yellow boxes). Ideally, we would like to be able to average over many eigenstates obtained by MPS methods on the MBL side of the transition, and to therefore extrapolate its scaling. However, given the current state of algorithms, we find this goal impossible to achieve due to the bias in the sampling of the states [196].

A few comments are in order: First, the clustering algorithm is a numerically very inexpensive procedure which is easily scalable, since only two-sites correlations need to be computed, allowing us to apply it to state in the MPS form.

Second, there is a clear agreement between the strong correlations and the increase in entanglement, as it can be seen by comparing the TSMI matrix with the bipartite von Neumann entanglement entropy (see Fig. 7.7). Indeed, two *local* communities are in general separated by a local minimum of bipartite entanglement entropy, but not all local minima of entanglement entropy signal a separation between two communities, as it is the case for example between sites 19 and 20 in Fig. 7.7. Moreover, entanglement entropy is unable to detect non-local clusters, i.e. “leapfrogging”, which we detect with our graph theory approach, for example at site 36 in Fig. 7.7. Therefore our approach give us different insights about the structure of the state than the one provided by the bipartite entanglement entropy alone. This brings us to our third point, namely that our approach does not rest on *a priori* physical assumptions, such as locality of the clusters for example. Indeed, the graph theory algorithm does not know about the spatial arrangements of the sites, since its only input is the TSMI matrix. However we note that in all

cases we considered, the clusters were still relatively local and did not extend throughout the system, in accordance with the results of Ref. [178].

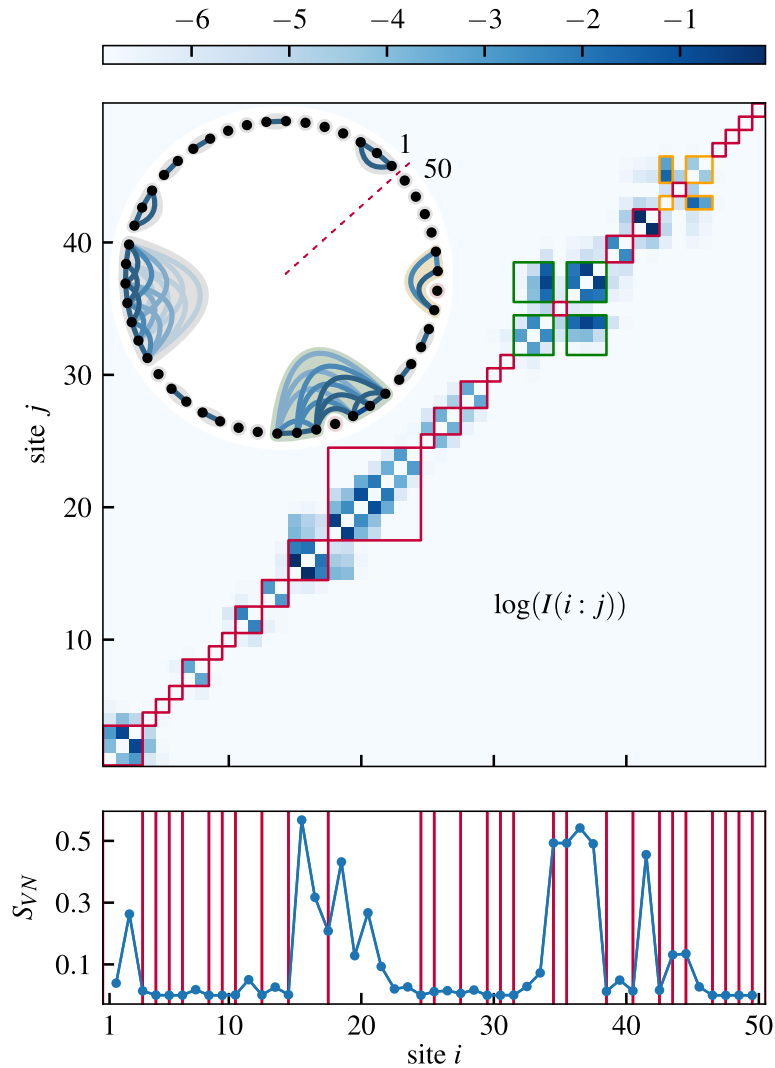


Figure 7.7 Example of the mutual information matrix and the associated communities (correlation clusters) of an eigenstate of a MBL hamiltonian obtained using the DMRG-X algorithm [174]. This disorder strength is $W = 12$, the system size is $L = 50$. On the top panel, we plot the mutual information matrix. We draw boxes around the matrix elements belonging to the same “correlation cluster”. We use a red box when a cluster is connected (i.e. no leapfrogging), while we use orange and green boxes for the two disconnected clusters. On the bottom panel, we present the bipartite entanglement entropy as a function of sites. The boundary between two clusters is signaled by a vertical red line. Inset we show the graph corresponding to the optimal clustering. The dashed red line separates the first and last site of the chain.

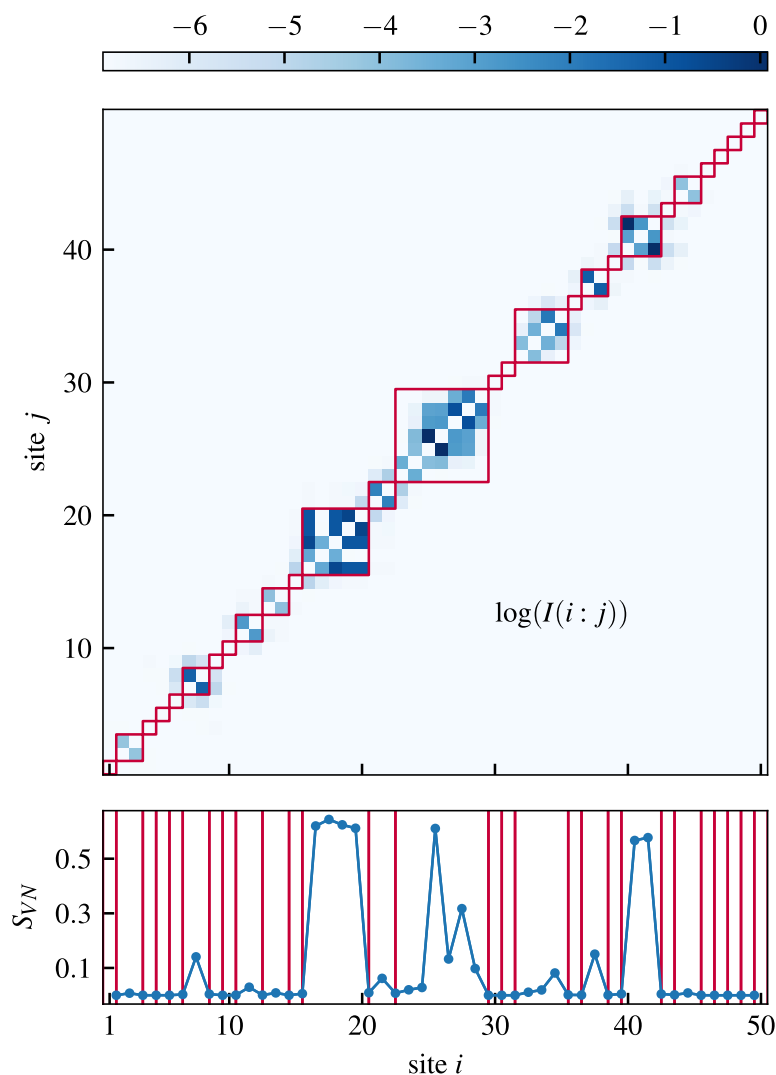


Figure 7.8 Example of the mutual information matrix and the associated communities (correlation clusters) of an eigenstate of a MBL hamiltonian obtained using the DMRG-X algorithm [174]. This disorder strength is $W = 12$, the system size is $L = 50$, as in Fig. 7.7. This state is typical of the results we obtained using MPS methods: all the clusters are local. As before, clusters are separated by local minima of bipartite entropy. However, we see once again a local minimum of entanglement entropy between sites 26 and 27, with still a quite high entanglement, which does not indicate the a cluster separation.

7.7 Non-equilibrium dynamics

7.7.1 Setup

We now turn to the behavior under non-equilibrium dynamics in the localized phase and compare AL and MBL systems. We now consider a global quantum quench protocol, starting from an initial Néel state $|\cdots \uparrow\downarrow\uparrow\downarrow \cdots\rangle$, and time evolve using the Hamiltonian Eq. (7.1) with $\Delta = 1$ (MBL) or $\Delta = 0$ (AL), with periodic boundary conditions. We can then analyse the correlations

as a function of time and identify the time dependence of the correlation clusters. We compare results obtained using the TSMI, $M_{ij} = I(i : j)$, and the correlation functions, $M_{ij} = C(\hat{\sigma}_i^z, \hat{\sigma}_j^z)$.

7.7.2 A configuration example

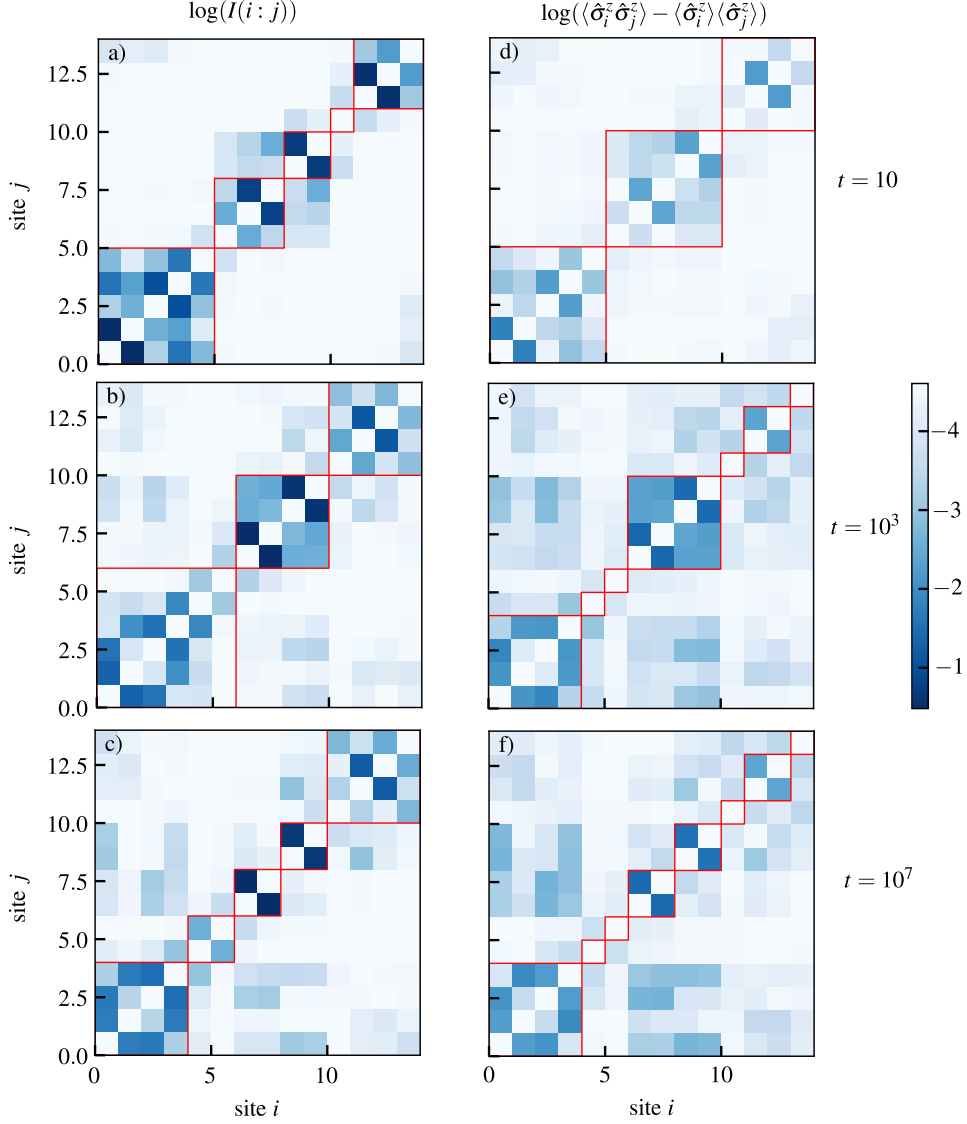


Figure 7.9 Cluster decomposition for different times obtained for an initial Neel state, time evolved with the Hamiltonian (7.1) with periodic boundary conditions for disorder strength $W = 8$ and $L = 14$. Panels a and d $t = 10$; panels b and e $t = 10^3$; panels c and f $t = 10^7$. Panels a, b and c: $M_{ij} = I(i : j)$. Panels d, e and f: $M_{ij} = C(\hat{\sigma}_i^z, \hat{\sigma}_j^z)$.

We first look at the behavior of a single characteristic disorder realisation. In Fig. 7.9 shows snapshots of the evolution of the clustering during the time evolution, both using the correlation functions in the σ^z basis and the TSMI. We present $t = 10$, $t = 10^3$ and $t = 10^7$. At short times, correlations start to build up locally, resulting in the formation of three large clusters. At intermediary times these blocks start to break up as correlation become more non local. Inter

cluster correlations (corresponding to “off-diagonal” elements on the correlation matrix) are more important resulting in a decrease of modularity. At long times, this process continues to unfold, with a further fragmentation of the cluster structure. However we note that, despite longer range correlations, a clear cluster structure is present, and the correlations are not completely scrambled. The remaining clusters are strongly reminiscent of the cluster structure at early times. Moreover, the inter-cluster interactions is more pronounced in the case of the correlation functions than in the case of the TSMI.

7.7.3 Disorder average graph theory quantities

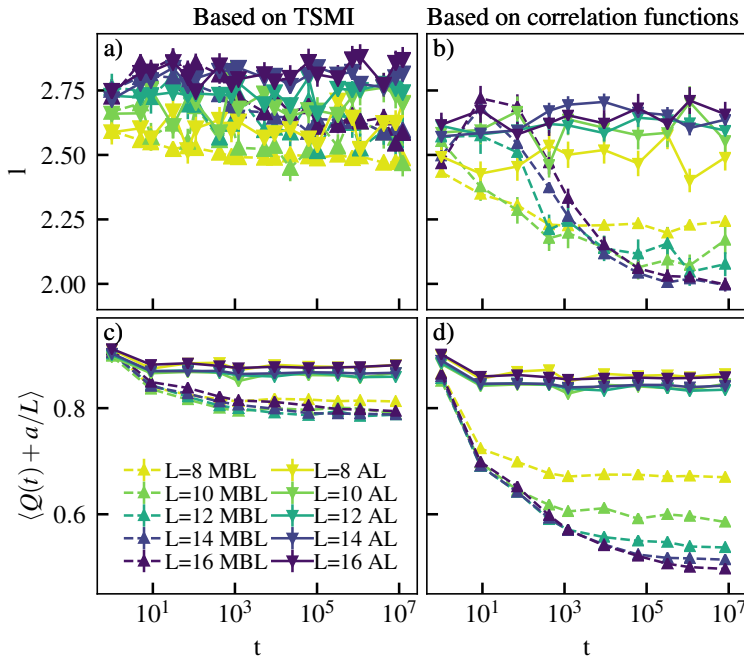


Figure 7.10 Average length of the clusters (panels a) and b)) and average modularity (panels c) and d)) as a function of time for different system sizes, with disorder strength $W = 8$, for both an Anderson localized (AL) ($\Delta = 0$) and MBL Hamiltonian ($\Delta = 1$). We start from a Néel state, simulate a quench using exact time evolution (ETE) and apply our graph theory approach to the TSMI matrix (panels a) and c)) and to the pairwise correlation functions in the σ_z basis (panels b) and d)). The fitting parameters are the following: panel c) MBL: $a = 3.69$, AL: $a = 3.63$; panel d) MBL: $a = 3.76$, AL: $a = 3.77$.

Fig. 7.10 a and b show the numerical results for the average cluster length l as a function of time. When using $M_{ij} = I(i : j)$, l stays approximately constant throughout time, both in the interacting and non interacting cases. In contrast, when using $M_{ij} = C(\hat{\sigma}_i^z, \hat{\sigma}_j^z)$, l decreases in the MBL case while it stays constant in the AL case.

In order to understand these results better and to be able to distinguish further MBL from AL using graph theory, we show the numerical results for the average modularity as a function of time on Fig. 7.10 panels b) and d). The offset of the modularity has been shifted so that the

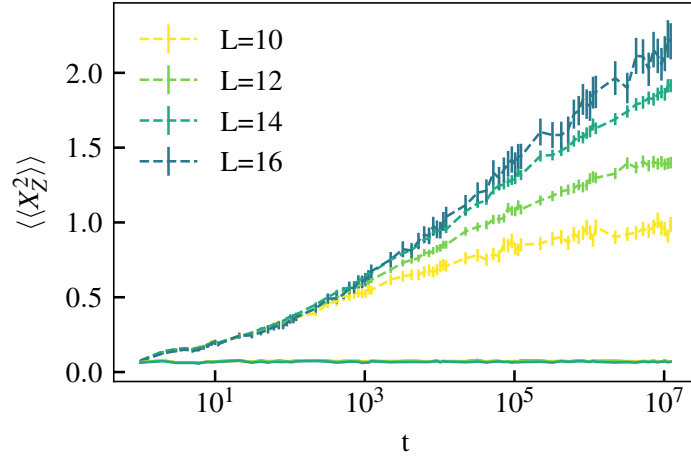


Figure 7.11 $\langle\langle X_Z \rangle\rangle$ for $W = 8$ for various system sizes. The MBL case is shown in dashed line while the AL case is plotted in full lines. All the curves for the AL case are superimposed. This demonstrate that the pairwise correlations in the σ_z basis are sufficient to probe the logarithmic propagation of information.

values for different system sizes coincide at short times. Indeed it is shown in section 7.4 that the modularity scales with the system size as $Q \sim q - aL^{-1}$ for comparable clusters. The value of a is found by fitting the data at short times and we find it to be roughly the same for both AL and MBL. In the non interacting case, the modularity Q stays constant throughout the time evolution. On the contrary, Q decreases in the interacting case.

7.7.4 Information propagation using pairwise correlation in the σ_z basis

In Ref. [186], it was shown that one can use the TSMI to detect the MBL phase. More precisely, one has to monitor the following quantity during a global quench:

$$\langle\langle X_I^2 \rangle\rangle = \sum_j j^2 I_j(t) - \left(\sum_j j I_j(t) \right)^2 \quad (7.17)$$

where $I_j(t) = I(0; j)(t)$. The MBL phase is characterized by a logarithmic growth of $\langle\langle X_I^2 \rangle\rangle$, since this quantity measures the spreading of information in the system. This is explained by the fact that two separate portions of the system need a time exponential with their distance to get entangled.

To demonstrate this, we perform ETE with the Hamiltonian (7.1) with open boundary conditions and calculate the following disorder averaged quantity:

$$\langle\langle \hat{X}_Z^2 \rangle\rangle = \sum_j j^2 C(\hat{\sigma}_0^z, \hat{\sigma}_j^z, t) - \left(\sum_j j C(\hat{\sigma}_0^z, \hat{\sigma}_j^z, t) \right)^2. \quad (7.18)$$

This quantity also exhibits logarithmic growth.

7.7.5 Interpretation

These observations can be explained as follows: at very short times (of the order of $\frac{1}{J}$), correlation clusters appear similarly for both AL and MBL. Due to dephasing in the MBL case, these clusters interact exponentially slowly with separation between them, leading to a slow decrease of the modularity until it reaches a minimum set by the system size. Over time, the correlations induced by this long-range dephasing will build up until they are comparable to the weakest correlations within a given cluster. At this point, those most weakly correlated sites in the cluster will be excluded in favour of forming a stronger, smaller cluster, as can be seen in the example presented in Fig. 7.9 in the appendix. This leads to a decrease of the average cluster length as a function of time in the interacting case, which is more pronounced with the pairwise correlations in the σ^z basis. This is consistent with the fact that at early times, the average length of the clusters are identical for MBL and AL, while at later times, due to the dephasing of the l-bits, it becomes smaller for MBL. Nonetheless, due to the presence of l-bits in the MBL system, for the system sizes and timescales accessible to us, these clusters are robust, as the modularity stays relatively high and the clustering at long times is still reminiscent of the structure found at early times.

The effect induced by the dephasing of the l-bits are more pronounced with the correlation functions than for the TSMI. This difference of behavior stems from the lack of transport in MBL [197], which implies that off-diagonal correlation functions cannot build up beyond the localization length. Thus, for our charge conserving model, only the σ^z component contributes to the growth of the TSMI at long times. Numerical evidence for the spreading of correlation functions in the σ_z basis is presented in appendix 7.7.4. As a consequence, when using the TSMI, the information contained in the σ^z correlation functions is washed out by all the other correlations, which necessarily decay for sufficiently large distances. This leads to more robust clusters which interact less strongly with each other. This is in line with findings of previous works [198–200], which have shown that quantities based on these correlators, in particular certain types quantum Fisher information, can probe the logarithmic growth of entanglement in MBL systems.

These findings show that it is advantageous to consider the σ^z component in this context. In particular, the diagonal σ^z correlations are accessible in existing quantum gas microscope experiments [25, 201, 202] and thus our technique can be directly be applied in such settings.

7.8 Conclusion

In this chapter, we have shown how to efficiently investigate the structure of MBL states using pairwise correlation functions and TSMI. We focused on two applications. First, we provide new numerical techniques for probing the structure of MBL eigenstates, scalable to large systems, particularly relevant for states obtained by MPS methods. Second, we show that our approach can provide a characterization of dynamics in the MBL phase. We have demonstrated that our clustering procedure yields results physically consistent with previously known results. When looking at the eigenstates, the scaling of the length of the clusters found in previous works [178] has been recovered. When looking at the dynamics, our results were consistent with the dephasing process between distant l-bits which is observed in other quantities such as the entanglement entropy or the quantum Fisher information. Moreover, we found that the quality of the clustering

at late times was still high, a fact which underlines the relevance of the clustering in the time evolution of MBL systems, for it is the persistence of these relatively well separated clusters which prevents full thermalization of the state and keeps the saturation of entanglement entropy well below the Page value.

More broadly, we have demonstrated the possibility of probing the structure of quantum states based solely on pairwise correlations using a graph theory approach. Our approach is well suited to experiments, where correlations in the diagonal σ^z basis are typically easy to measure. Furthermore, our approach is agnostic to the structure or dimensionality of the underlying Hamiltonian or dynamics. It would therefore be exciting to test this approach in the task of distinguishing MBL systems from Anderson localized in experiments in both one and two dimensional setups.

8 Summary and outlook

In this thesis, we have explored different strategies to simulate out-of-equilibrium quantum many-body systems on classical computers. We have seen that the large entanglement generated by the dynamics is a hurdle to the study of such systems, but it is not the only one.

We started this thesis by giving an overview of some aspects of the current understanding of out-of-equilibrium physics in one dimension. First, we have seen in chapter 2 that the excited eigenstates of ergodic Hamiltonians behave like random vectors in the Hilbert space, a fact that can be understood from random matrix theory and which implies that they are highly entangled. In chapter 3, we discussed many-body localization (MBL). In particular, we highlighted how the emergence of quasi-local conserved quantities, called the *local integral of motions* or *l-bits*, allows these systems to escape thermalization in one dimension, and causes all eigenstates to follow area law. In chapter 4, we reviewed some of the most common matrix-product state (MPS) methods used for obtaining eigenstates and for performing time evolution.

In chapter 5, we used various MPS methods to simulate the propagation of information in an isolated ergodic system. We circumvented the problem of the large amount of entanglement generated during quantum time evolution by using on one hand the time dependent variational principle (TDVP) with MPS algorithm, which conserves the energy and the unitarity of time evolution, thus providing a useful low entangled approximation, and on the other hand by using MPO time evolution. By comparing our results to large scale exact time evolution simulations, we were able to provide convincing evidence that both of these methods were able to capture the low operator entanglement regime of the out-of-time-order correlators (OTOCs). These results demonstrate the possibility to calculate these quantities at longer time and with larger system sizes than normally possible with MPS.

In chapter 6, we were able to give an estimate of the diffusion coefficient of some non integrable one dimensional models. To do so, we induced a current by introducing some dissipation at the boundaries. Although open quantum systems are generally even more challenging to simulate than closed ones, we were able to reach steady states which carry few operator entanglement. The method takes advantage of the fact that at long times, the density matrix of thermalizing systems usually carries little operator entanglement, as is exemplified by the infinite temperature density matrix which is a product operator. Our benchmarks show that the simulation of boundary dissipative systems can be useful to understand diffusion physics. It is particularly interesting to compare these results with the dissipation assisted operator evolution (DAOE) method, since both techniques can probe similar system sizes and rest on completely different approximations and assumptions.

Finally, in chapter 7, we explored the connexion between graph theory and quantum information in MBL systems. For these kind of systems which do not exhibit thermalization, the

amount of entanglement contained in the eigenstates is not an insurmountable obstacle, as they admit a faithful MPS representation with relatively low bond dimension. However, calculating multipartite entanglement remains challenging, and we devised a strategy based on the pairwise correlations in order to identify correlation clusters in the states. Furthermore, the logarithmically slow growth of entanglement—one of the hallmarks of MBL—is notably difficult to measure in experiments. Our approach allows for the characterization of MBL dynamics directly from the accessible pairwise correlations, circumventing the difficulty of calculating the entanglement entropy and is directly relevant for currently available experimental devices. In particular, we propose to use existing quantum gas microscopes to directly study the dynamics of correlation clusters in cold atom systems.

Despite the progress being made in the last few years, out-of-equilibrium many-body physics is still a relatively new area of research and it is likely that many interesting phenomena are still to be discovered. The recent progress in experiments open exciting new possibilities [25–27, 203–205] and are motivating an increasingly large body of theoretical works. Furthermore, quantum dynamics could well be among of the first applications of digital quantum computers, which are emerging nowadays as a promising new technology. Indeed, quantum time evolution is relatively straightforward as it can be achieved by the application of unitary gates, precisely the task for which these quantum computers are designed [173, 206].

The work presented in this thesis suggests some promising research directions. While we are able to describe the onset of information propagation, it would be desirable to formulate a numerical approach able to systematically reach the hydrodynamic regime of ergodic systems, starting from the microscopic degrees of freedom. Since we were able to simulate some aspects of ergodic systems with some reasonable classical computation resources in chapters 5 and 6, this program seems all the more feasible. This direction is the subject of active research, leading in recent years to an increasing number of new promising numerical methods [149, 207–209].

Furthermore, while MBL eigenstates are slightly entangled, they remain difficult to capture with MPS due to the exponentially small many-body level spacing in the middle of the spectrum. Finding a truly reliable MPS algorithm able to resolve individual states is still a significant challenge. It would allow for the simulation of the MBL phase for much larger system sizes, hence yielding information about the influence of finite size effects. Furthermore, one could also approach the ergodic/MBL critical point from the MBL side.

Acknowledgments

First of all, I would like to thank Prof. Frank Pollmann for supervising me during this PhD and for providing me with all the support, advices and encouragements that I needed to move forward. The teachings I gathered from his guidance will follow me throughout the rest of my career, and allowed me to become a better physicist. I would like to give special thanks to Prof. Michael Knap for co-examining my thesis and to Prof. Johannes Knolle for taking the time to be my IMPRS co-supervisor.

I would like to thank my colleagues with whom I had the pleasure of working. To begin with, I would like to thank David Luitz. He welcomed me into the group and helped me throughout my first project, sharing his extensive experience in large scale numerics along the way. I am also very grateful to Adam Smith for helping me exploring the intricacies of MBL physics, and the many stimulating discussions we had during our collaboration. Exploring diffusion in spin chain is not an easy task, but it can be pleasant when working with the right people. Therefore I would like to thank Tibor Rakovszky for all our discussions, inside and outside our work together; in particular, exchanging with him about quantum chaos helped to refine my understanding of the subject. I am also grateful for the help of Curt Von Keyserlingk, for his never fading interest in my results and the new physics they could contain. It was also a great pleasure to work with Ewan McCulloch and Izabella Lovas, who always made herself available to share her seemingly unlimited knowledge about theoretical condensed matter physics.

The years during which my PhD took place were spanned by many scientific and unscientific exchanges which were an integral part of the experience. First of all, I would like to thank Johannes Hauschild, whose patience and availability is always exceptional. His work on TeNPy, the open source tensor network library, is extremely valuable to us all, and his assistance in all numerical matters was very helpful. I am grateful that I could meet Ruben Verresen, who helped me teach topological phases of matter, and shared his insights on this subject. I would also like to thank ShengHsuan for his advices about finding a position at the end of my PhD. I am also grateful for the discussions we had with Giueseppe de Tomasi about MBL physics. I would also like to thank Claudine Voelcker for her patience and her help in all administrative matters. I have many fond memories of the time I spent with all the members of the group, so special thanks to Pablo Sala, Johannes Feldmeier, Julian Bibo, Markus Drescher and Alvis Bastianello.

On the personal level, I would like to dearly thank all my family members. Without their support and encouragements, I would never have been able to pursue my studies so far. Finally, I am grateful to Elisabeth for sharing my life during the last five years, and for always being there for me when I needed her. Thanking her enough for all the beautiful memories we have together would require a thesis of its own.

Appendix

A. Scaling with different modularity thresholds

In the main text, we present the scaling collapse of the number of clusters divided by system size. When the modularity obtained for one clustering is smaller than $Q_{\text{th}}(L) = \alpha(1 - a/L)$, we bypass our algorithm and consider that the state is fully ergodic and therefore made of a single cluster. In Figs. 8.1 and 8.2, we show that the scaling collapse is not sensitive to the value of the coefficient α , as long as α is such that the modularity of almost all eigenstates deep in the ergodic (resp. MBL) phase is below (resp. above) $Q_{\text{th}}(L)$.

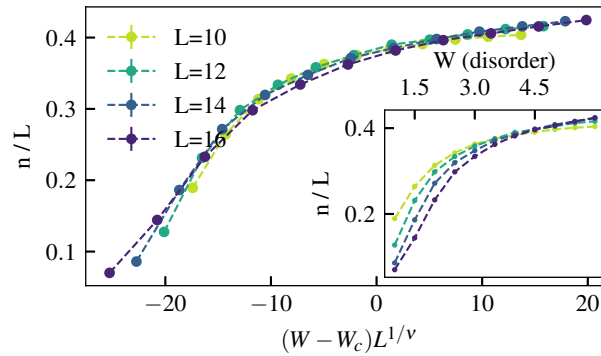


Figure 8.1 Scaling collapse of the average number of clusters n divided by system size as a function of the disorder obtained using our modified Girvan-Newman approach and $\alpha = 0.25$. The parameters used for the scaling collapse are the same as in the main text. Inset: average number of clusters n divided by system size as a function of disorder strength W .

B. Scaling collapse of the number of clusters using the pairwise correlation functions in the σ^z basis

In the main text, we present in Fig. 7.6 a scaling collapse of the averaged number of clusters divided by system size for which we used the TSMI of the eigenstates as the adjacency matrix in our graph theory approach. We show in Fig. 8.3 that the same approach using the pairwise correlation functions in the σ^z basis yields the same scaling collapse. In order to ensure that all states deep in the MBL phase are identified as such, we need to choose a smaller coefficient α for Q_{th} (see Eq. (7.15)). Here we choose $\alpha = 0.15$.

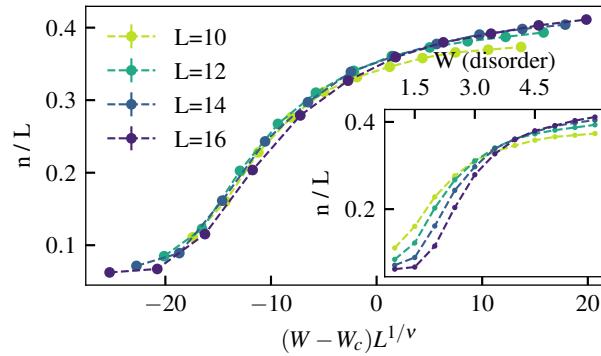


Figure 8.2 Scaling collapse of the average number of clusters n divided by system size as a function of the disorder obtained using our modified Girvan-Newman approach and $\alpha = 0.4$. The parameters used for the scaling collapse are the same as in the main text. Inset: average number of clusters n divided by system size as a function of disorder strength W .

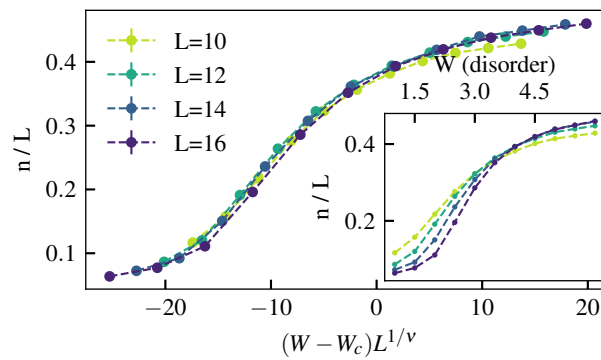


Figure 8.3 Scaling collapse of the average number of clusters n divided by system size as a function of the disorder obtained using our modified Girvan-Newman approach applied to the pairwise correlation functions in the σ^z basis, $\alpha = 0.15$ and $a = 3.01$. The parameters used for the scaling collapse are the same as in the main text. Inset: average number of clusters n divided by system size as a function of disorder strength W .

List of Figures

3.1	Ergodic eigenstates in the middle of the spectrum are highly entangled as they follow volume law (panel a), while all eigenstates of MBL Hamiltonian follow area law (panel b).	17
3.2	Schematic representation of the strong randomness RG scheme applied on MBL state close to the transition. During the first step, where $\Lambda = 1$, the smallest I block is thermalized by two larger T blocks. At the second step ($\Lambda = 2$) the only remaining I block is thermalized as well. At the end of the procedure, one obtain a fully thermal state.	22
4.1	Schematic representation of the TEBD algorithm: a) Schrödinger representation, where A^i is the tensor at site i of the MPS corresponding to the state that we wish to evolve, H_{ij} denotes the gates of the Hamiltonian between sites i and j and dt is the time step; b) Heisenberg representation, where O^i is the tensor at site i of the MPO corresponding to the operator that we wish to evolve.	30
5.1	Schematic representation of the spreading of the operator support of an operator $V_i(t)$ initially at position $x = i$ as a function of time t . When the operator support reaches the position j , the quantity $\ [\hat{W}_j, \hat{V}_i(t)]\ _F^2$ starts to grow. The OTOC is therefore a measure of operator spreading in isolated quantum systems.	39
5.2	Example of trace calculation with MPOs following equation (5.5), using four sites. The tensor contraction gives the quantity $\text{Tr}(\hat{V}_4(t)\hat{W}_1\hat{V}_4(t)\hat{W}_1)$	41
5.3	Example of calculation of time evolution necessary to obtain the OTOC with the MPS TDVP method using equation (5.7). (a) represents the time evolution $\hat{V}_i(t) \sigma\rangle$, while the tensor contraction (b) represents the full out-of-order part of the correlator, up to the initial phase σ^z . These operation must be averaged stochastically to give the correct result.	43
5.4	OTOCs for $L = 21$ obtained using a) ETE b) Schroedinger TDVP approach, sampling over 98 random product states and bond dimension $\chi = 64$	44
5.5	Fixed space cuts of the OTOC $C_{4,j} = \frac{1}{2}\ [\hat{\sigma}_4^z(t), \sigma_j^z]\ _F^2$ obtained using different methods compared to exact time evolution (ETE). a) TDVP with wave function time evolution, where the trace in Eq. (5.5) is sampled using 98 random product states b) TEBD with wave function time evolution where the trace is sampled using 98 random states (the errorbars represent the error coming from the stochastic sampling) c) TEBD with operator time evolution (exact trace). All MPS calculations were performed with a time step $dt = 0.01$, bond dimension $\chi = 64$ and system size $L = 21$. The red dashed line is the theoretical upper bound for the long time limit for completely scrambled operators.	45

- 5.6 Deviation from the exact result using the three methods for the calculation of the OTOC for the longest distance from site $i = 4$ to $j = 21$ as a function of time. Based on the results shown in Fig. 5.5 (Bond dimension $\chi = 64$, time step $dt = 0.01$, system size $L = 21$ sites, the errorbars represent the error coming from the stochastic sampling). 46
- 5.7 Comparison of the error $|C_{4,j}^{\text{exact}}(t) - C_{4,j}^{\text{TDVP MPS}}|$ for TDVP MPS and TEBD MPS $|C_{4,j}^{\text{exact}}(t) - C_{4,j}^{\text{TEBD MPS}}|$ for different bond dimension χ . The system sizes is $L = 21$, the time step is $dt = 0.01$ 47
- 5.8 OTOC $C_{4,j}(t) = \frac{1}{2} \|\hat{\sigma}_4^z(t) \sigma_j^z\|_F^2$ as a function of distance and time for MPS TDVP with time step $dt = 0.005$, bond dimension $\chi = 64$ and averaged over 387 random states a) and MPO TEBD with time step $dt = 0.01$ and bond dimension $\chi = 128$ b), both for system size $L = 50$. The full lines and symbols correspond to contour lines obtained from the numerical solution of the equation $C_{4,j}(t) = \theta$ for various thresholds θ , where j is the position of the constant operator in the chain. The contour lines given by these solutions are denoted $t(\theta, j)$. The errorbars are representing the error coming from the stochastic sampling and are extracted using the bootstrap method. 48
- 5.9 Contour lines obtained from the numerical solution of the equation $C_{4,j}(t) = \theta$ for various thresholds θ and methods, where j is the site. These solutions are denoted $t(\theta, j)$. The different methods used are MPO TEBD, MPS TDVP and ETE. We fit the ETE data between the sites 4 and 21 with a power law: $f(x) = \lambda(4 - x)^\mu$ with x the distance and the fitting parameters: a) $\lambda = 0.20$, $\mu = 1.32$, b) $\lambda = 0.31$, $\mu = 1.21$, c) $\lambda = 0.50$, $\mu = 1.12$, d) $\lambda = 0.52$, $\mu = 1.14$. The data comes from the same calculation as Fig. 5.8 (MPS TDVP: bond dimension $\chi = 64$, time step $dt = 0.005$, system size $L = 50$ sites, averaged over 387 random states; MPO TEBD: bond dimension $\chi = 128$, time step $dt = 0.01$, system size $L = 50$ sites). The errorbars are obtained in the same way than in Fig. 5.8 a). 49
- 5.10 Convergence in bond-dimension of fixed space cuts of the OTOC $C_{4,j}^{(15)}(t) = 1 - \frac{1}{2^{15}} \sum_{k=1}^{15} \langle \psi_k | \hat{\sigma}_4^z(t) \sigma_j^z \sigma_4^z(t) \sigma_j^z | \psi_k \rangle$ obtained with Schrödinger TDVP with the same 15 randomly chosen initial product states $|\psi_k\rangle$ for bond dimension $\chi = 64$ and $\chi = 32$ for time step $dt = 0.01$, and system size $L = 50$ 50
- 5.11 Convergence in bond-dimension of fixed space cuts of the OTOC $C_{4,j}^{(1)}(t)$ obtained with Schrödinger TDVP for only *one* random initial product state for bond dimension $\chi = 64$ and $\chi = 32$ and using a time step $dt = 0.01$ for a system of size $L = 50$. The worst and best converged initial states of the ones used in Fig. 5.10 are displayed in order to demonstrate the difference in convergence depending on the initial state. 51
- 5.12 Convergence with bond dimension χ of the contours lines of the OTOCs calculated with MPO TEBD. We represent the numerical solution of the equation $C_{4,j}(t) = \theta$ for various thresholds θ and bond dimension ($\chi = 64$ and $\chi = 128$) for system size $L = 50$ sites and time step $dt = 0.01$. j is the site of the light cone for different thresholds θ (see Fig. 5.9). 52
- 6.1 Example of two TEBD time steps applied to the density matrix expressed as a matrix-product state for a system size of 4 sites. The bath is coupled at most with the two left-most and right-most sites of the chain, while the time evolution is unitary in the bulk. 59

- 6.2 Energy current j as a function of system size L for the tilted field Ising model (Eq. (6.28)) with $g_x = 1.4$ and $g_z = 0.9045$. The dotted line are the fits of $\log(L) = C + \log(j/\mu)^\alpha$, where we find $\alpha = -0.9975$, in accordance with the expectation of a diffusive behavior. 61
- 6.3 Obtained diffusion coefficient for the tilted field Ising model as function of system size. The 4 leftmost and rightmost sites has been excluded from the calculation in order to exclude the boundary effects. The dotted black line represents the diffusion coefficient obtained using the DOAE method. The results were obtained using bond dimension up to $\chi_{\max} = 700$. Inset: diffusion coefficient as a function of the inverse system size. Inset: diffusion coefficient as a function of $\frac{1}{L}$ 62
- 6.4 Steady state current j divided by the imbalance μ as a function of system size, for different couplings with the environment Γ . The dotted line are the fits of $\log(L) = C + \log(j/\mu)^\alpha$, where we find $\alpha_{\Gamma=1} = -1.0447$ $\alpha_{\Gamma=16} = -1.0381$, $\alpha_{\Gamma=4} = -1.039$, $\alpha_{\Gamma=4} = -1.0287$ in accordance with the expectation of a diffusive behavior. 64
- 6.5 Diffusion coefficient as a function of the system size L for different system sizes. The results were obtained using bond dimension up to $\chi_{\max} = 220$. The length of error bar is given by the maximum difference between the diffusion coefficient obtained for the central site with the diffusion coefficient obtained for any other site. The prediction of the method are in clear disagreement with the theoretical predictions of Ref. [150]: $D = 0.95$ 65
- 6.6 Obtained diffusion coefficient for the XX ladder as a function of system size, for different couplings with the environment Γ . The two leftmost and rightmost sites where excluded to avoid boundary effects. Panel a: $J=1.0$, Panel b: $J=1.5$. The black dotted line represents the diffusion coefficient obtained using exact methods in Ref. [138], while the gray dotted line correspond to the value of D using DAOE [153]. The results were obtained using bond dimension up to $\chi_{\max} = 300$ 66
- 7.1 Schematic description of our graph theory approach using an example of the mutual information matrix M_{ij} . The full graph has zero modularity (see Eq. (7.13)). We then successively remove the weakest edges until the graph is broken into a larger number of clusters. These steps where a new clustering is obtained are saved and are indicated by a ring around them and the value of their modularity is given. In this example we find a very low modularity of $Q = -0.00023$ for the first clustering, indicating no community structure. The next new clustering occurs after removing several bonds (not all shown) and has a relatively high modularity of 0.32, which turns out to be the highest obtained for this example. We identify this clustering as the physical one and is indicated by a green ring in the figure. The next steps of the decomposition yields four clusters with a modularity of $Q = 0.23$, smaller than in the last step, indicating community structure of a lower quality. The rest of the procedure was not represented here, but the modularity was decreasing at each new step. 68

- 7.2 Comparison between a typical example of clustering obtained by applying the “entanglement clustering” procedure (left) and the “correlation clustering” (right) applied to the same state. The state chosen to apply these two procedures is an excited eigenstate of the Hamiltonian (7.1) for $L = 12$, $W = 5$ and $\Delta = 1$. On the left panel, we show the tree structure resulting from the entanglement clustering, where the sites belonging to the same cluster are listed between parentheses, while the internal mutual information can be read in the line below between the arrow. For example, the two first lines should be read as follows: the system containing sites (4, 5, 6, 7, 8, 9, 10, 11, 0, 1, 2, 3) splits up into the clusters (4, 5, 6, 7, 8, 9) and (10, 11, 0, 1, 2, 3), with associated normalized mutual information is equal to 0.0019. On the right panel, we show the dendrogram resulting from the correlation clustering procedure: the sites between parentheses belong to the same cluster, while the number on the left of the arrow corresponds to the modularity Q . A dotted arrow indicates that we have omitted to represent one or several intermediary steps. 73
- 7.3 Detection of the ergodic/MBL phase transition using entanglement entropy: we measure the maximum entanglement entropy for each state obtained using full diagonalization of the XXZ Hamiltonian. We identify ergodic states when the maximum entanglement entropy is greater than 60% of the page value. a) Average maximum entanglement as a function of disorder for different system sizes. b) Ratio of ergodic states detected p_{ergodic} as a function of disorder W . . . 74
- 7.4 Scaling collapse of the average number of clusters n divided by system size as a function of the disorder obtained using our modified Girvan-Newman approach. For the collapse, the disorder strength was rescaled to take the form $(W - W_c)L^{1/\nu}$ with $W_c = 3.8$ and $\nu = 1.26$. An eigenstate with bipartite entanglement entropy in the middle of the chain bigger than 0.6 times the page value was considered to be ergodic and therefore was counted as one cluster, independently of the result of the graph theory approach. Inset: average number of clusters n divided by system size as a function of disorder strength W 75
- 7.5 Detection of the ergodic/MBL phase transition using entanglement entropy: when $Q_{\text{th}} = \alpha(1 - a/L)$ with $\alpha = 0.3$ and $a = 3.59$, the state is considered as fully ergodic. a) Average modularity as a function of disorder for different system sizes. b) Ratio p_{ergodic} of the ergodic states as a function of disorder W . . 76
- 7.6 Scaling collapse of the average number of clusters n divided by system size as a function of the disorder obtained using our modified Girvan-Newman approach. For the collapse, the disorder strength was rescaled to take the form $(W - W_c)L^{1/\nu}$ with $W_c = 3.8$ and $\nu = 1.26$. When the modularity was lower than $Q_{\text{th}} = \alpha(1 - a/L)$ with $\alpha = 0.3$ and $a = 3.59$, the state was considered as fully ergodic and made of only one cluster. The coefficient a has been fitted to take into account the finite size effects at $W = 6$, according to the finite size scaling: $Q_L = q - \frac{a}{L}$ of the average modularity Q_L obtained for system size L . Inset: average number of clusters n divided by system size as a function of disorder strength W 77

- 7.7 Example of the mutual information matrix and the associated communities (correlation clusters) of an eigenstate of a MBL hamiltonian obtained using the DMRG-X algorithm [174]. This disorder strength is $W = 12$, the system size is $L = 50$. On the top panel, we plot the mutual information matrix. We draw boxes around the matrix elements belonging to the same “correlation cluster”. We use a red box when a cluster is connected (i.e. no leapfrogging), while we use orange and green boxes for the two disconnected clusters. On the bottom panel, we present the bipartite entanglement entropy as a function of sites. The boundary between two clusters is signaled by a vertical red line. Inset we show the graph corresponding to the optimal clustering. The dashed red line separates the first and last site of the chain. 80
- 7.8 Example of the mutual information matrix and the associated communities (correlation clusters) of an eigenstate of a MBL hamiltonian obtained using the DMRG-X algorithm [174]. This disorder strength is $W = 12$, the system size is $L = 50$, as in Fig. 7.7. This state is typical of the results we obtained using MPS methods: all the clusters are local. As before, clusters are separated by local minima of bipartite entropy. However, we see once again a local minimum of entanglement entropy between sites 26 and 27, with still a quite high entanglement, which does not indicate the a cluster separation. 81
- 7.9 Cluster decomposition for different times obtained for an initial Neel state, time evolved with the Hamiltonian (7.1) with periodic boundary conditions for disorder strength $W = 8$ and $L = 14$. Panels a and d $t = 10$; panels b and e $t = 10^3$; panels c and f $t = 10^7$. Panels a, b and c: $M_{ij} = I(i : j)$. Panels d, e and f: $M_{ij} = C(\hat{\sigma}_i^z, \hat{\sigma}_j^z)$ 82
- 7.10 Average length of the clusters (panels a) and b)) and average modularity (panels c) and d)) as a function of time for different system sizes, with disorder strength $W = 8$, for both an Anderson localized (AL) ($\Delta = 0$) and MBL Hamiltonian ($\Delta = 1$). We start from a Néel state, simulate a quench using exact time evolution (ETE) and apply our graph theory approach to the TSMI matrix (panels a) and c)) and to the pairwise correlation functions in the σ_z basis (panels b) and d)). The fitting parameters are the following: panel c) MBL: $a = 3.69$, AL: $a = 3.63$; panel d) MBL: $a = 3.76$, AL: $a = 3.77$ 83
- 7.11 $\langle\langle X_Z \rangle\rangle$ for $W = 8$ for various system sizes. The MBL case is shown in dashed line while the AL case is plotted in full lines. All the curves for the AL case are superimposed. This demonstrate that the pairwise correlations in the σ_z basis are sufficient to probe the logarithmic propagation of information. 84
- 8.1 Scaling collapse of the average number of clusters n divided by system size as a function of the disorder obtained using our modified Girvan-Newman approach and $\alpha = 0.25$. The parameters used for the scaling collapse are the same as in the main text. Inset: average number of clusters n divided by system size as a function of disorder strength W 91
- 8.2 Scaling collapse of the average number of clusters n divided by system size as a function of the disorder obtained using our modified Girvan-Newman approach and $\alpha = 0.4$. The parameters used for the scaling collapse are the same as in the main text. Inset: average number of clusters n divided by system size as a function of disorder strength W 92

- 8.3 Scaling collapse of the average number of clusters n divided by system size as a function of the disorder obtained using our modified Girvan-Newman approach applied to the pairwise correlation functions in the σ^z basis, $\alpha = 0.15$ and $a = 3.01$. The parameters used for the scaling collapse are the same as in the main text. Inset: average number of clusters n divided by system size as a function of disorder strength W 92

Bibliography

Refs. [1, 2] can be found in the [List of Publications](#).

- [3] P. W. Anderson. “More is different.” *Science* **177**, pp. 393, 1972. doi:[10.1126/science.177.4047.393](https://doi.org/10.1126/science.177.4047.393).
- [4] S. R. White. “Density matrix formulation for quantum renormalization groups.” *Phys. Rev. Lett.* **69**, pp. 2863, 1992. doi:[10.1103/PhysRevLett.69.2863](https://doi.org/10.1103/PhysRevLett.69.2863).
- [5] M. B. Hastings. “An area law for one-dimensional quantum systems.” *Journal of Statistical Mechanics: Theory and Experiment* **2007**, pp. P08024, 2007. doi:[10.1088/1742-5468/2007/08/p08024](https://doi.org/10.1088/1742-5468/2007/08/p08024).
- [6] F. D. M. Haldane. “Nonlinear field theory of large-spin heisenberg antiferromagnets: Semiclassically quantized solitons of the one-dimensional easy-axis néel state.” *Phys. Rev. Lett.* **50**, pp. 1153, 1983. doi:[10.1103/PhysRevLett.50.1153](https://doi.org/10.1103/PhysRevLett.50.1153).
- [7] M. H. Anderson, J. R. Ensher, M. R. Matthews, C. E. Wieman, and E. A. Cornell. “Observation of bose-einstein condensation in a dilute atomic vapor.” *Science* **269**, pp. 198, 1995. doi:[10.1126/science.269.5221.198](https://doi.org/10.1126/science.269.5221.198).
- [8] K. B. Davis, M. O. Mewes, M. R. Andrews, N. J. van Druten, D. S. Durfee, D. M. Kurn, and W. Ketterle. “Bose-einstein condensation in a gas of sodium atoms.” *Phys. Rev. Lett.* **75**, pp. 3969, 1995. doi:[10.1103/PhysRevLett.75.3969](https://doi.org/10.1103/PhysRevLett.75.3969).
- [9] R. Blatt and C. F. Roos. “Quantum simulations with trapped ions.” *Nature Physics* **8**, pp. 277, 2012. doi:[10.1038/nphys2252](https://doi.org/10.1038/nphys2252).
- [10] I. Bloch, J. Dalibard, and S. Nascimbène. “Quantum simulations with ultracold quantum gases.” *Nature Physics* **8**, pp. 267, 2012. doi:[10.1038/nphys2259](https://doi.org/10.1038/nphys2259).
- [11] C. Gross and I. Bloch. “Quantum simulations with ultracold atoms in optical lattices.” *Science* **357**, pp. 995, 2017. doi:[10.1126/science.aal3837](https://doi.org/10.1126/science.aal3837).
- [12] A. A. Houck, H. E. Türeci, and J. Koch. “On-chip quantum simulation with superconducting circuits.” *Nature Physics* **8**, pp. 292, 2012. doi:[10.1038/nphys2251](https://doi.org/10.1038/nphys2251).
- [13] M. Aidelsburger, M. Lohse, C. Schweizer, M. Atala, J. T. Barreiro, S. Nascimbène, N. R. Cooper, I. Bloch, and N. Goldman. “Measuring the chern number of hofstadter bands with ultracold bosonic atoms.” *Nature Physics* **11**, pp. 162, 2015. doi:[10.1038/nphys3171](https://doi.org/10.1038/nphys3171).
- [14] M. Greiner, O. Mandel, T. Esslinger, T. W. Hänsch, and I. Bloch. “Quantum phase transition from a superfluid to a mott insulator in a gas of ultracold atoms.” *Nature* **415**,

- pp. 39, 2002. doi:[10.1038/415039a](https://doi.org/10.1038/415039a).
- [15] N. Navon, S. Nascimbène, F. Chevy, and C. Salomon. “The equation of state of a low-temperature fermi gas with tunable interactions.” *Science* **328**, pp. 729, 2010. doi:[10.1126/science.1187582](https://doi.org/10.1126/science.1187582).
- [16] J. M. Deutsch. “Eigenstate thermalization hypothesis.” *Reports on Progress in Physics* **81**, p. 082001, 2018. doi:[10.1088/1361-6633/aac9f1](https://doi.org/10.1088/1361-6633/aac9f1).
- [17] J. v. Neumann. “Beweis des ergodensatzes und desh-theorems in der neuen mechanik.” *Zeitschrift für Physik* **57**, pp. 30, 1929. doi:[10.1007/BF01339852](https://doi.org/10.1007/BF01339852).
- [18] J. M. Deutsch. “Quantum statistical mechanics in a closed system.” *Phys. Rev. A* **43**, pp. 2046, 1991. doi:[10.1103/PhysRevA.43.2046](https://doi.org/10.1103/PhysRevA.43.2046).
- [19] M. Srednicki. “Chaos and quantum thermalization.” *Phys. Rev. E* **50**, pp. 888, 1994. doi:[10.1103/PhysRevE.50.888](https://doi.org/10.1103/PhysRevE.50.888).
- [20] C. Rylands and N. Andrei. “Nonequilibrium aspects of integrable models.” *Annual Review of Condensed Matter Physics* **11**, pp. 147, 2020. doi:[10.1146/annurev-conmatphys-031119-050630](https://doi.org/10.1146/annurev-conmatphys-031119-050630).
- [21] M. Gring, M. Kuhnert, T. Langen, T. Kitagawa, B. Rauer, M. Schreitl, I. Mazets, D. A. Smith, E. Demler, and J. Schmiedmayer. “Relaxation and prethermalization in an isolated quantum system.” *Science* **337**, pp. 1318, 2012. doi:[10.1126/science.1224953](https://doi.org/10.1126/science.1224953).
- [22] Y. Tang, W. Kao, K.-Y. Li, S. Seo, K. Mallayya, M. Rigol, S. Gopalakrishnan, and B. L. Lev. “Thermalization near integrability in a dipolar quantum newton’s cradle.” *Phys. Rev. X* **8**, p. 021030, 2018. doi:[10.1103/PhysRevX.8.021030](https://doi.org/10.1103/PhysRevX.8.021030).
- [23] P. W. Anderson. “Absence of Diffusion in Certain Random Lattices.” *Physical Review* **109**, pp. 1492, 1958. doi:[10.1103/PhysRev.109.1492](https://doi.org/10.1103/PhysRev.109.1492).
- [24] D. Basko, I. Aleiner, and B. Altshuler. “Metal–insulator transition in a weakly interacting many-electron system with localized single-particle states.” *Annals of Physics* **321**, pp. 1126, 2006. doi:<https://doi.org/10.1016/j.aop.2005.11.014>.
- [25] M. Schreiber, S. S. Hodgman, P. Bordia, H. P. Lüschen, M. H. Fischer, R. Vosk, E. Altman, U. Schneider, and I. Bloch. “Observation of many-body localization of interacting fermions in a quasirandom optical lattice.” *Science (80-.)*. **349**, pp. 842, 2015. doi:[10.1126/science.aaa7432](https://doi.org/10.1126/science.aaa7432).
- [26] J.-y. Choi, S. Hild, J. Zeiher, P. Schauss, A. Rubio-Abadal, T. Yefsah, V. Khemani, D. A. Huse, I. Bloch, and C. Gross. “Exploring the many-body localization transition in two dimensions.” *Science (80-.)*. **352**, pp. 1547, 2016. doi:[10.1126/science.aaf8834](https://doi.org/10.1126/science.aaf8834).
- [27] P. Bordia, H. Lüschen, S. Scherg, S. Gopalakrishnan, M. Knap, U. Schneider, and I. Bloch. “Probing Slow Relaxation and Many-Body Localization in Two-Dimensional Quasiperiodic Systems.” *Phys. Rev. X* **7**, p. 041047, 2017. doi:[10.1103/PhysRevX.7.041047](https://doi.org/10.1103/PhysRevX.7.041047).

- [28] J. Cardy. *Scaling and Renormalization in Statistical Physics*. Cambridge Lecture Notes in Physics. Cambridge University Press, 1996.
- [29] N. Y. Yao, C. R. Laumann, and A. Vishwanath. “Many-body localization protected quantum state transfer.” *arXiv e-prints* arXiv:1508.06995, 2015.
- [30] C. Berke, E. Varvelis, S. Trebst, A. Altland, and D. P. DiVincenzo. “Transmon platform for quantum computing challenged by chaotic fluctuations.”, 2021.
- [31] C. W. von Keyserlingk, T. Rakovszky, F. Pollmann, and S. L. Sondhi. “Operator hydrodynamics, otocs, and entanglement growth in systems without conservation laws.” *Phys. Rev. X* **8**, p. 021013, 2018. doi:[10.1103/PhysRevX.8.021013](https://doi.org/10.1103/PhysRevX.8.021013).
- [32] T. Rakovszky, F. Pollmann, and C. W. von Keyserlingk. “Diffusive hydrodynamics of out-of-time-ordered correlators with charge conservation.” *Phys. Rev. X* **8**, p. 031058, 2018. doi:[10.1103/PhysRevX.8.031058](https://doi.org/10.1103/PhysRevX.8.031058).
- [33] V. Khemani, A. Vishwanath, and D. A. Huse. “Operator spreading and the emergence of dissipative hydrodynamics under unitary evolution with conservation laws.” *Phys. Rev. X* **8**, p. 031057, 2018. doi:[10.1103/PhysRevX.8.031057](https://doi.org/10.1103/PhysRevX.8.031057).
- [34] A. Nahum, S. Vijay, and J. Haah. “Operator spreading in random unitary circuits.” *Phys. Rev. X* **8**, p. 021014, 2018. doi:[10.1103/PhysRevX.8.021014](https://doi.org/10.1103/PhysRevX.8.021014).
- [35] H. Liu and P. Glorioso. “Lectures on non-equilibrium effective field theories and fluctuating hydrodynamics.” In “Proceedings of Theoretical Advanced Study Institute Summer School 2017,” doi:[10.22323/1.305.0008](https://doi.org/10.22323/1.305.0008).
- [36] J. Lux, J. Müller, A. Mitra, and A. Rosch. “Hydrodynamic long-time tails after a quantum quench.” *Phys. Rev. A* **89**, p. 053608, 2014. doi:[10.1103/PhysRevA.89.053608](https://doi.org/10.1103/PhysRevA.89.053608).
- [37] A. Einstein, B. Podolsky, and N. Rosen. “Can quantum-mechanical description of physical reality be considered complete?” *Phys. Rev.* **47**, pp. 777, 1935. doi:[10.1103/PhysRev.47.777](https://doi.org/10.1103/PhysRev.47.777).
- [38] E. Schrödinger. “Energieaustausch nach der wellenmechanik.” *Annalen der Physik* **388**, pp. 956, 1927. doi:<https://doi.org/10.1002/andp.19273881504>.
- [39] J. von Neumann. “Proof of the ergodic theorem and the h-theorem in quantum mechanics.” *The European Physical Journal H* **35**, pp. 201, 2010. doi:[10.1140/epjh/e2010-00008-5](https://doi.org/10.1140/epjh/e2010-00008-5).
- [40] L. D’Alessio, Y. Kafri, A. Polkovnikov, and M. Rigol. “From quantum chaos and eigenstate thermalization to statistical mechanics and thermodynamics.” *Advances in Physics* **65**, pp. 239, 2016. doi:[10.1080/00018732.2016.1198134](https://doi.org/10.1080/00018732.2016.1198134).
- [41] E. P. Wigner. “Characteristic vectors of bordered matrices with infinite dimensions.” *Annals of Mathematics* **62**, pp. 548, 1955.
- [42] E. P. Wigner. “Characteristics vectors of bordered matrices with infinite dimensions ii.” *Annals of Mathematics* **65**, pp. 203, 1957.

- [43] E. P. Wigner. “On the distribution of the roots of certain symmetric matrices.” *Annals of Mathematics* **67**, pp. 325, 1958.
- [44] M. MEHTA. In “Random Matrices and the Statistical Theory of Energy Levels,” Academic Press, 1967. ISBN 978-1-4832-3258-4. doi:<https://doi.org/10.1016/C2013-0-12505-6>.
- [45] T. A. Brody, J. Flores, J. B. French, P. A. Mello, A. Pandey, and S. S. M. Wong. “Random-matrix physics: spectrum and strength fluctuations.” *Rev. Mod. Phys.* **53**, pp. 385, 1981. doi:[10.1103/RevModPhys.53.385](https://doi.org/10.1103/RevModPhys.53.385).
- [46] Y. Alhassid. “The statistical theory of quantum dots.” *Rev. Mod. Phys.* **72**, pp. 895, 2000. doi:[10.1103/RevModPhys.72.895](https://doi.org/10.1103/RevModPhys.72.895).
- [47] D. N. Page. “Average entropy of a subsystem.” *Phys. Rev. Lett.* **71**, pp. 1291, 1993. doi:[10.1103/PhysRevLett.71.1291](https://doi.org/10.1103/PhysRevLett.71.1291).
- [48] N. F. Mott and W. D. Twose. “The theory of impurity conduction.” *Advances in Physics* **10**, pp. 107, 1961. doi:[10.1080/00018736100101271](https://doi.org/10.1080/00018736100101271).
- [49] G. Stolz. “An introduction to the mathematics of anderson localization.” *Entropy and the quantum II. Contemp. Math* **552**, pp. 71, 2011.
- [50] I. Y. Gol’dshstein, S. A. Molchanov, and L. A. Pastur. “A pure point spectrum of the stochastic one-dimensional schrödinger operator.” *Functional Analysis and Its Applications* **11**, pp. 1, 1977. doi:[10.1007/BF01135526](https://doi.org/10.1007/BF01135526).
- [51] H. Kunz and B. Souillard. “Sur le spectre des opérateurs aux différences finies aléatoires.” *Communications in Mathematical Physics* **78**, pp. 201, 1980. doi:[10.1007/BF01942371](https://doi.org/10.1007/BF01942371).
- [52] D. J. Thouless. “A relation between the density of states and range of localization for one dimensional random systems.” *Journal of Physics C: Solid State Physics* **5**, pp. 77, 1972. doi:[10.1088/0022-3719/5/1/010](https://doi.org/10.1088/0022-3719/5/1/010).
- [53] P. Jordan and E. Wigner. “Über das paulische äquivalenzverbot.” *Zeitschrift für Physik* **47**, pp. 631, 1928.
- [54] V. Oganesyan and D. A. Huse. “Localization of interacting fermions at high temperature.” *Phys. Rev. B* **75**, p. 155111, 2007. doi:[10.1103/PhysRevB.75.155111](https://doi.org/10.1103/PhysRevB.75.155111).
- [55] A. Pal and D. A. Huse. “Many-body localization phase transition.” *Phys. Rev. B* **82**, p. 174411, 2010. doi:[10.1103/PhysRevB.82.174411](https://doi.org/10.1103/PhysRevB.82.174411).
- [56] M. Serbyn, Z. Papić, and D. A. Abanin. “Local conservation laws and the structure of the many-body localized states.” *Phys. Rev. Lett.* **111**, p. 127201, 2013. doi:[10.1103/PhysRevLett.111.127201](https://doi.org/10.1103/PhysRevLett.111.127201).
- [57] D. A. Abanin, E. Altman, I. Bloch, and M. Serbyn. “Colloquium: Many-body localization, thermalization, and entanglement.” *Rev. Mod. Phys.* **91**, p. 021001, 2019. doi:[10.1103/RevModPhys.91.021001](https://doi.org/10.1103/RevModPhys.91.021001).

- [58] X. Yu, D. J. Luitz, and B. K. Clark. “Bimodal entanglement entropy distribution in the many-body localization transition.” *Phys. Rev. B* **94**, p. 184202, 2016. doi:[10.1103/PhysRevB.94.184202](https://doi.org/10.1103/PhysRevB.94.184202).
- [59] D. A. Huse, R. Nandkishore, and V. Oganesyan. “Phenomenology of fully many-body-localized systems.” *Phys. Rev. B* **90**, p. 174202, 2014. doi:[10.1103/PhysRevB.90.174202](https://doi.org/10.1103/PhysRevB.90.174202).
- [60] J. Z. Imbrie. “On Many-Body Localization for Quantum Spin Chains.” *J. Stat. Phys.* **163**, pp. 998, 2016. doi:[10.1007/s10955-016-1508-x](https://doi.org/10.1007/s10955-016-1508-x).
- [61] M. Žnidarič, T. Prosen, and P. Prelovšek. “Many-body localization in the Heisenberg XXZ magnet in a random field.” *Phys. Rev. B* **77**, p. 064426, 2008. doi:[10.1103/PhysRevB.77.064426](https://doi.org/10.1103/PhysRevB.77.064426).
- [62] J. H. Bardarson, F. Pollmann, and J. E. Moore. “Unbounded growth of entanglement in models of many-body localization.” *Phys. Rev. Lett.* **109**, p. 017202, 2012. doi:[10.1103/PhysRevLett.109.017202](https://doi.org/10.1103/PhysRevLett.109.017202).
- [63] M. Serbyn, Z. Papić, and D. A. Abanin. “Universal slow growth of entanglement in interacting strongly disordered systems.” *Phys. Rev. Lett.* **110**, p. 260601, 2013. doi:[10.1103/PhysRevLett.110.260601](https://doi.org/10.1103/PhysRevLett.110.260601).
- [64] D. A. Abanin and Z. Papić. “Recent progress in many-body localization.” *Annalen der Physik* **529**, p. 1700169, 2017. doi:<https://doi.org/10.1002/andp.201700169>.
- [65] C. Dasgupta and S.-k. Ma. “Low-temperature properties of the random heisenberg anti-ferromagnetic chain.” *Phys. Rev. B* **22**, pp. 1305, 1980. doi:[10.1103/PhysRevB.22.1305](https://doi.org/10.1103/PhysRevB.22.1305).
- [66] F. Iglói and C. Monthus. “Strong disorder rg approach of random systems.” *Physics Reports* **412**, pp. 277, 2005. doi:<https://doi.org/10.1016/j.physrep.2005.02.006>.
- [67] D. Pekker, G. Refael, E. Altman, E. Demler, and V. Oganesyan. “Hilbert-glass transition: New universality of temperature-tuned many-body dynamical quantum criticality.” *Phys. Rev. X* **4**, p. 011052, 2014. doi:[10.1103/PhysRevX.4.011052](https://doi.org/10.1103/PhysRevX.4.011052).
- [68] A. Morningstar and D. A. Huse. “Renormalization-group study of the many-body localization transition in one dimension.” *Phys. Rev. B* **99**, p. 224205, 2019. doi:[10.1103/PhysRevB.99.224205](https://doi.org/10.1103/PhysRevB.99.224205).
- [69] P. T. Dumitrescu, A. Goremykina, S. A. Parameswaran, M. Serbyn, and R. Vasseur. “Kosterlitz-thouless scaling at many-body localization phase transitions.” *Phys. Rev. B* **99**, p. 094205, 2019. doi:[10.1103/PhysRevB.99.094205](https://doi.org/10.1103/PhysRevB.99.094205).
- [70] W. De Roeck and F. . “Stability and instability towards delocalization in many-body localization systems.” *Phys. Rev. B* **95**, p. 155129, 2017. doi:[10.1103/PhysRevB.95.155129](https://doi.org/10.1103/PhysRevB.95.155129).
- [71] R. Vosk, D. A. Huse, and E. Altman. “Theory of the many-body localization transition in one-dimensional systems.” *Phys. Rev. X* **5**, p. 031032, 2015. doi:[10.1103/PhysRevX.5.031032](https://doi.org/10.1103/PhysRevX.5.031032).

- [72] D. J. Luitz, F. m. c. Huveneers, and W. De Roeck. “How a small quantum bath can thermalize long localized chains.” *Phys. Rev. Lett.* **119**, p. 150602, 2017. doi:[10.1103/PhysRevLett.119.150602](https://doi.org/10.1103/PhysRevLett.119.150602).
- [73] A. C. Potter, R. Vasseur, and S. A. Parameswaran. “Universal properties of many-body delocalization transitions.” *Phys. Rev. X* **5**, p. 031033, 2015. doi:[10.1103/PhysRevX.5.031033](https://doi.org/10.1103/PhysRevX.5.031033).
- [74] L. Zhang, B. Zhao, T. Devakul, and D. A. Huse. “Many-body localization phase transition: A simplified strong-randomness approximate renormalization group.” *Phys. Rev. B* **93**, p. 224201, 2016. doi:[10.1103/PhysRevB.93.224201](https://doi.org/10.1103/PhysRevB.93.224201).
- [75] A. Goremykina, R. Vasseur, and M. Serbyn. “Analytically solvable renormalization group for the many-body localization transition.” *Phys. Rev. Lett.* **122**, p. 040601, 2019. doi:[10.1103/PhysRevLett.122.040601](https://doi.org/10.1103/PhysRevLett.122.040601).
- [76] V. Khemani, S. P. Lim, D. N. Sheng, and D. A. Huse. “Critical properties of the many-body localization transition.” *Phys. Rev. X* **7**, p. 021013, 2017. doi:[10.1103/PhysRevX.7.021013](https://doi.org/10.1103/PhysRevX.7.021013).
- [77] F. Huveneers. “Classical and quantum systems: transport due to rare events.” *Annalen der Physik* **529**, p. 1600384, 2017. doi:<https://doi.org/10.1002/andp.201600384>.
- [78] S. Gopalakrishnan and S. Parameswaran. “Dynamics and transport at the threshold of many-body localization.” *Physics Reports* **862**, pp. 1, 2020. doi:<https://doi.org/10.1016/j.physrep.2020.03.003>. Dynamics and transport at the threshold of many-body localization.
- [79] J. M. Kosterlitz and D. J. Thouless. “Ordering, metastability and phase transitions in two-dimensional systems.” *Journal of Physics C: Solid State Physics* **6**, pp. 1181, 1973. doi:[10.1088/0022-3719/6/7/010](https://doi.org/10.1088/0022-3719/6/7/010).
- [80] A. Chandran, C. R. Laumann, and V. Oganesyan. “Finite size scaling bounds on many-body localized phase transitions.” *arXiv e-prints* arXiv:1509.04285, 2015.
- [81] R. J. Baxter. “Dimers on a rectangular lattice.” *Journal of Mathematical Physics* **9**, pp. 650, 1968. doi:[10.1063/1.1664623](https://doi.org/10.1063/1.1664623).
- [82] I. Affleck, T. Kennedy, E. H. Lieb, and H. Tasaki. “Rigorous results on valence-bond ground states in antiferromagnets.” *Phys. Rev. Lett.* **59**, pp. 799, 1987. doi:[10.1103/PhysRevLett.59.799](https://doi.org/10.1103/PhysRevLett.59.799).
- [83] M. Fannes, B. Nachtergaele, and R. F. Werner. “Finitely correlated states on quantum spin chains.” *Comm. Math. Phys.* **144**, pp. 443, 1992.
- [84] S. Östlund and S. Rommer. “Thermodynamic limit of density matrix renormalization.” *Phys. Rev. Lett.* **75**, pp. 3537, 1995. doi:[10.1103/PhysRevLett.75.3537](https://doi.org/10.1103/PhysRevLett.75.3537).
- [85] G. Vidal. “Efficient classical simulation of slightly entangled quantum computations.” *Phys. Rev. Lett.* **91**, p. 147902, 2003. doi:[10.1103/PhysRevLett.91.147902](https://doi.org/10.1103/PhysRevLett.91.147902).

- [86] F. Verstraete, D. Porras, and J. I. Cirac. “Density matrix renormalization group and periodic boundary conditions: A quantum information perspective.” *Phys. Rev. Lett.* **93**, p. 227205, 2004. doi:[10.1103/PhysRevLett.93.227205](https://doi.org/10.1103/PhysRevLett.93.227205).
- [87] U. Schollwöck. “The density-matrix renormalization group in the age of matrix product states.” *Annals of Physics* **326**, pp. 96 , 2011. doi:<https://doi.org/10.1016/j.aop.2010.09.012>. January 2011 Special Issue.
- [88] J. Haegeman, C. Lubich, I. Oseledets, B. Vandereycken, and F. Verstraete. “Unifying time evolution and optimization with matrix product states.” *Phys. Rev. B* **94**, p. 165116, 2016. doi:[10.1103/PhysRevB.94.165116](https://doi.org/10.1103/PhysRevB.94.165116).
- [89] F. Verstraete, V. Murg, and J. Cirac. “Matrix product states, projected entangled pair states, and variational renormalization group methods for quantum spin systems.” *Advances in Physics* **57**, pp. 143, 2008. doi:[10.1080/14789940801912366](https://doi.org/10.1080/14789940801912366).
- [90] C. Lanczos. “An iteration method for the solution of the eigenvalue problem of linear differential and integral operators.” *J. Res. Nat. Bur. Stand.* **49**, 1950.
- [91] C. Paige. *The Computation of Eigenvalues and Eigenvectors of Very Large Sparse Matrices*. Ph.D. thesis, London University, 1971.
- [92] P. A. M. Dirac. “Note on exchange phenomena in the thomas atom.” *Mathematical Proceedings of the Cambridge Philosophical Society* **26**, p. 376–385, 1930. doi:[10.1017/S0305004100016108](https://doi.org/10.1017/S0305004100016108).
- [93] J. Haegeman, J. I. Cirac, T. J. Osborne, I. Pižorn, H. Verschelde, and F. Verstraete. “Time-dependent variational principle for quantum lattices.” *Phys. Rev. Lett.* **107**, p. 070601, 2011. doi:[10.1103/PhysRevLett.107.070601](https://doi.org/10.1103/PhysRevLett.107.070601).
- [94] J. Haegeman, T. J. Osborne, and F. Verstraete. “Post-matrix product state methods: To tangent space and beyond.” *Phys. Rev. B* **88**, p. 075133, 2013. doi:[10.1103/PhysRevB.88.075133](https://doi.org/10.1103/PhysRevB.88.075133).
- [95] J. Dukelsky, M. A. Martín-Delgado, T. Nishino, and G. Sierra. “Equivalence of the variational matrix product method and the density matrix renormalization group applied to spin chains.” *EPL (Europhysics Letters)* **43**, pp. 457, 1998. doi:[10.1209/epl/i1998-00381-x](https://doi.org/10.1209/epl/i1998-00381-x).
- [96] M. Hochbruck and C. Lubich. “On krylov subspace approximations to the matrix exponential operator.” *SIAM Journal on Numerical Analysis* **34**, pp. 1911, 1997. doi:[10.1137/S0036142995280572](https://doi.org/10.1137/S0036142995280572).
- [97] I. Bloch, J. Dalibard, and W. Zwerger. “Many-body physics with ultracold gases.” *Rev. Mod. Phys.* **80**, pp. 885, 2008. doi:[10.1103/RevModPhys.80.885](https://doi.org/10.1103/RevModPhys.80.885).
- [98] M. Srednicki. “Chaos and quantum thermalization.” *Phys. Rev. E* **50**, pp. 888, 1994. doi:[10.1103/PhysRevE.50.888](https://doi.org/10.1103/PhysRevE.50.888).
- [99] M. Rigol, V. Dunjko, and M. Olshanii. “Thermalization and its mechanism for generic isolated quantum systems.” *Nature* **452**, pp. 854 EP , 2008.

- [100] L. D'Alessio, Y. Kafri, A. Polkovnikov, and M. Rigol. "From quantum chaos and eigenstate thermalization to statistical mechanics and thermodynamics." *Advances in Physics* **65**, pp. 239, 2016. doi:[10.1080/00018732.2016.1198134](https://doi.org/10.1080/00018732.2016.1198134).
- [101] F. Borgonovi, F. M. Izrailev, L. F. Santos, and V. G. Zelevinsky. "Quantum chaos and thermalization in isolated systems of interacting particles." *Physics Reports* **626**, pp. 1, 2016. doi:[10.1016/j.physrep.2016.02.005](https://doi.org/10.1016/j.physrep.2016.02.005).
- [102] A. M. Kaufman, M. E. Tai, A. Lukin, M. Rispoli, R. Schittko, P. M. Preiss, and M. Greiner. "Quantum thermalization through entanglement in an isolated many-body system." *Science* **353**, pp. 794, 2016. doi:[10.1126/science.aaf6725](https://doi.org/10.1126/science.aaf6725).
- [103] J. R. Garrison and T. Grover. "Does a Single Eigenstate Encode the Full Hamiltonian?" *Phys. Rev. X* **8**, p. 021026, 2018. doi:[10.1103/PhysRevX.8.021026](https://doi.org/10.1103/PhysRevX.8.021026).
- [104] D. J. Luitz. "Long tail distributions near the many-body localization transition." *Phys. Rev. B* **93**, p. 134201, 2016. doi:[10.1103/PhysRevB.93.134201](https://doi.org/10.1103/PhysRevB.93.134201).
- [105] R. Nandkishore and D. A. Huse. "Many-body localization and thermalization in quantum statistical mechanics." *Annual Review of Condensed Matter Physics* **6**, pp. 15, 2015. doi:[10.1146/annurev-conmatphys-031214-014726](https://doi.org/10.1146/annurev-conmatphys-031214-014726).
- [106] H. Kim and D. A. Huse. "Ballistic spreading of entanglement in a diffusive nonintegrable system." *Phys. Rev. Lett.* **111**, p. 127205, 2013. doi:[10.1103/PhysRevLett.111.127205](https://doi.org/10.1103/PhysRevLett.111.127205).
- [107] D. J. Luitz, N. Laflorencie, and F. Alet. "Extended slow dynamical regime close to the many-body localization transition." *Phys. Rev. B* **93**, p. 060201, 2016. doi:[10.1103/PhysRevB.93.060201](https://doi.org/10.1103/PhysRevB.93.060201).
- [108] A. I. Larkin and Y. N. Ovchinnikov. "Quasiclassical method in the theory of superconductivity." *Jetp* **28**, p. 1200, 1969.
- [109] J. Maldacena, S. H. Shenker, and D. Stanford. "A bound on chaos." *Journal of High Energy Physics* **8**, 106, 2016. doi:[10.1007/JHEP08\(2016\)106](https://doi.org/10.1007/JHEP08(2016)106).
- [110] E. H. Lieb and D. W. Robinson. "The finite group velocity of quantum spin systems." *Communications in Mathematical Physics* **28**, pp. 251, 1972. doi:[10.1007/BF01645779](https://doi.org/10.1007/BF01645779).
- [111] M. Knap. "Entanglement production and information scrambling in a noisy spin system." *Phys. Rev. B* **98**, p. 184416, 2018. doi:[10.1103/PhysRevB.98.184416](https://doi.org/10.1103/PhysRevB.98.184416).
- [112] D. J. Luitz and Y. Bar Lev. "Information propagation in isolated quantum systems." *Phys. Rev. B* **96**, p. 020406, 2017. doi:[10.1103/PhysRevB.96.020406](https://doi.org/10.1103/PhysRevB.96.020406).
- [113] X. Chen, T. Zhou, D. A. Huse, and E. Fradkin. "Out-of-time-order correlations in many-body localized and thermal phases." *Ann. Phys. (Berlin)* **529**, p. 1600332, 2016. doi:[10.1002/andp.201600332](https://doi.org/10.1002/andp.201600332).
- [114] A. Bohrdt, C. B. Mendl, M. Endres, and M. Knap. "Scrambling and thermalization in a diffusive quantum many-body system." *New Journal of Physics* **19**, p. 063001, 2017.

- [115] S. Xu and B. Swingle. “Accessing scrambling using matrix product operators.” 2018.
- [116] E. Leviatan, F. Pollmann, J. H. Bardarson, and E. Altman. “Quantum thermalization dynamics with Matrix-Product States.” 2017.
- [117] B. Kloss, Y. B. Lev, and D. Reichman. “Time-dependent variational principle in matrix-product state manifolds: Pitfalls and potential.” *Phys. Rev. B* **97**, p. 024307, 2018. doi:[10.1103/PhysRevB.97.024307](https://doi.org/10.1103/PhysRevB.97.024307).
- [118] I. Pižorn and T. Prosen. “Operator space entanglement entropy in XY spin chains.” *Phys. Rev. B* **79**, p. 184416, 2009. doi:[10.1103/PhysRevB.79.184416](https://doi.org/10.1103/PhysRevB.79.184416).
- [119] T. Zhou and D. J. Luitz. “Operator entanglement entropy of the time evolution operator in chaotic systems.” *Phys. Rev. B* **95**, p. 094206, 2017. doi:[10.1103/PhysRevB.95.094206](https://doi.org/10.1103/PhysRevB.95.094206).
- [120] J. Dubail. “Entanglement scaling of operators: a conformal field theory approach, with a glimpse of simulability of long-time dynamics in $1 + 1d$.” *J. Phys. A: Math. Theor.* **50**, p. 234001, 2017. doi:[10.1088/1751-8121/aa6f38](https://doi.org/10.1088/1751-8121/aa6f38).
- [121] J. Rammensee, J. D. Urbina, and K. Richter. “Many-body quantum interference and the saturation of out-of-time-order correlators.” *Phys. Rev. Lett.* **121**, p. 124101, 2018. doi:[10.1103/PhysRevLett.121.124101](https://doi.org/10.1103/PhysRevLett.121.124101).
- [122] V. Khemani, D. A. Huse, and A. Nahum. “Velocity-dependent lyapunov exponents in many-body quantum, semiclassical, and classical chaos.” *Phys. Rev. B* **98**, p. 144304, 2018. doi:[10.1103/PhysRevB.98.144304](https://doi.org/10.1103/PhysRevB.98.144304).
- [123] A. Y. Kitaev. “A simple model of quantum holography, part I.” 2015.
- [124] D. J. Luitz and Y. Bar Lev. “Emergent locality in systems with power-law interactions.” *arXiv:1805.06895* 2018. ArXiv: 1805.06895.
- [125] T. J. Park and J. C. Light. “Unitary quantum time evolution by iterative lanczos reduction.” *The Journal of Chemical Physics* **85**, pp. 5870, 1986. doi:[10.1063/1.451548](https://doi.org/10.1063/1.451548).
- [126] S. R. Manmana, A. Muramatsu, and R. M. Noack. “Time evolution of one-dimensional Quantum Many Body Systems.” In A. Avella and F. Mancini (editors), “Lectures on the Physics of Highly Correlated Electron Systems IX,” volume 789 of *American Institute of Physics Conference Series*, pp. 269–278. 2005. doi:[10.1063/1.2080353](https://doi.org/10.1063/1.2080353).
- [127] C. Moler and C. Van Loan. “Nineteen dubious ways to compute the exponential of a matrix, twenty-five years later.” *SIAM Review* **45**, pp. 3, 2003. doi:[10.1137/S00361445024180](https://doi.org/10.1137/S00361445024180).
- [128] S. R. White. “Minimally Entangled Typical Quantum States at Finite Temperature.” *Phys. Rev. Lett.* **102**, p. 190601, 2009. doi:[10.1103/PhysRevLett.102.190601](https://doi.org/10.1103/PhysRevLett.102.190601).
- [129] P. Glorioso and H. Liu. “Lectures on non-equilibrium effective field theories and fluctuating hydrodynamics.” *ArXiv e-prints* 2018.
- [130] M. Blake, H. Lee, and H. Liu. “A quantum hydrodynamical description for scrambling and many-body chaos.” *Journal of High Energy Physics* **2018**, p. 127, 2018.

doi:[10.1007/JHEP10\(2018\)127](https://doi.org/10.1007/JHEP10(2018)127).

- [131] A. Lucas. “Constraints on hydrodynamics from many-body quantum chaos.” *ArXiv e-prints* 2017.
- [132] E. V. H. Doggen, F. Schindler, K. S. Tikhonov, A. D. Mirlin, T. Neupert, D. G. Polyakov, and I. V. Gornyi. “Many-body localization and delocalization in large quantum chains.” *Phys. Rev. B* **98**, p. 174202, 2018. doi:[10.1103/PhysRevB.98.174202](https://doi.org/10.1103/PhysRevB.98.174202).
- [133] S. Paeckel, T. Köhler, A. Swoboda, S. R. Manmana, U. Schollwöck, and C. Hubig. “Time-evolution methods for matrix-product states.” 2019.
- [134] J. De Nardis, M. Medenjak, C. Karrasch, and E. Ilievski. “Universality classes of spin transport in one-dimensional isotropic magnets: The onset of logarithmic anomalies.” *Phys. Rev. Lett.* **124**, p. 210605, 2020. doi:[10.1103/PhysRevLett.124.210605](https://doi.org/10.1103/PhysRevLett.124.210605).
- [135] M. Michel, J. Gemmer, and G. Mahler. “Heat conductivity in small quantum systems: Kubo formula in liouville space.” *The European Physical Journal B - Condensed Matter and Complex Systems* **42**, pp. 555, 2004. doi:[10.1140/epjb/e2005-00014-x](https://doi.org/10.1140/epjb/e2005-00014-x).
- [136] H. L. Stormer. “Nobel lecture: The fractional quantum hall effect.” *Rev. Mod. Phys.* **71**, pp. 875, 1999. doi:[10.1103/RevModPhys.71.875](https://doi.org/10.1103/RevModPhys.71.875).
- [137] M. Žnidarič, A. Scardicchio, and V. K. Varma. “Diffusive and subdiffusive spin transport in the ergodic phase of a many-body localizable system.” *Phys. Rev. Lett.* **117**, p. 040601, 2016. doi:[10.1103/PhysRevLett.117.040601](https://doi.org/10.1103/PhysRevLett.117.040601).
- [138] R. Steinigeweg, F. Heidrich-Meisner, J. Gemmer, K. Michielsen, and H. De Raedt. “Scaling of diffusion constants in the spin- $\frac{1}{2}$ xx ladder.” *Phys. Rev. B* **90**, p. 094417, 2014. doi:[10.1103/PhysRevB.90.094417](https://doi.org/10.1103/PhysRevB.90.094417).
- [139] F. Heidrich-Meisner, A. Honecker, D. C. Cabra, and W. Brenig. “Zero-frequency transport properties of one-dimensional spin- $\frac{1}{2}$ systems.” *Phys. Rev. B* **68**, p. 134436, 2003. doi:[10.1103/PhysRevB.68.134436](https://doi.org/10.1103/PhysRevB.68.134436).
- [140] H. Maeter, A. A. Zvyagin, H. Luetkens, G. Pasqua, Z. Shermadini, R. Saint-Martin, A. Revcolevschi, C. Hess, B. Büchner, and H.-H. Klauss. “Low temperature ballistic spin transport in the $S=1/2$ antiferromagnetic heisenberg chain compound SrCuO_2 .” *Journal of Physics: Condensed Matter* **25**, p. 365601, 2013. doi:[10.1088/0953-8984/25/36/365601](https://doi.org/10.1088/0953-8984/25/36/365601).
- [141] F. Xiao, J. S. Möller, T. Lancaster, R. C. Williams, F. L. Pratt, S. J. Blundell, D. Ceresoli, A. M. Barton, and J. L. Manson. “Spin diffusion in the low-dimensional molecular quantum heisenberg antiferromagnet $\text{Cu}(\text{pyz})(\text{NO}_3)_2$ detected with implanted muons.” *Phys. Rev. B* **91**, p. 144417, 2015. doi:[10.1103/PhysRevB.91.144417](https://doi.org/10.1103/PhysRevB.91.144417).
- [142] H. Kühne, A. A. Zvyagin, M. Günther, A. P. Reyes, P. L. Kuhns, M. M. Turnbull, C. P. Landee, and H.-H. Klauss. “Dynamics of a heisenberg spin chain in the quantum critical regime: Nmr experiment versus effective field theory.” *Phys. Rev. B* **83**, p. 100407, 2011. doi:[10.1103/PhysRevB.83.100407](https://doi.org/10.1103/PhysRevB.83.100407).

- [143] T. Prosen and M. Žnidarič. “Matrix product simulations of non-equilibrium steady states of quantum spin chains.” *Journal of Statistical Mechanics: Theory and Experiment* **2009**, p. P02035, 2009. doi:[10.1088/1742-5468/2009/02/p02035](https://doi.org/10.1088/1742-5468/2009/02/p02035).
- [144] G. Lindblad. “On the generators of quantum dynamical semigroups.” *Communications in Mathematical Physics* **48**, pp. 119, 1976.
- [145] M. Žnidarič. “Nonequilibrium steady-state kubo formula: Equality of transport coefficients.” *Phys. Rev. B* **99**, p. 035143, 2019. doi:[10.1103/PhysRevB.99.035143](https://doi.org/10.1103/PhysRevB.99.035143).
- [146] Y. Yoo, J. Lee, and B. Swingle. “Nonequilibrium steady state phases of the interacting aubry-andré-harper model.” *Phys. Rev. B* **102**, p. 195142, 2020. doi:[10.1103/PhysRevB.102.195142](https://doi.org/10.1103/PhysRevB.102.195142).
- [147] J. J. Mendoza-Arenas, S. R. Clark, and D. Jaksch. “Coexistence of energy diffusion and local thermalization in nonequilibrium xxz spin chains with integrability breaking.” *Phys. Rev. E* **91**, p. 042129, 2015. doi:[10.1103/PhysRevE.91.042129](https://doi.org/10.1103/PhysRevE.91.042129).
- [148] M. Žnidarič, T. c. v. Prosen, G. Benenti, G. Casati, and D. Rossini. “Thermalization and ergodicity in one-dimensional many-body open quantum systems.” *Phys. Rev. E* **81**, p. 051135, 2010. doi:[10.1103/PhysRevE.81.051135](https://doi.org/10.1103/PhysRevE.81.051135).
- [149] T. Rakovszky, C. W. von Keyserlingk, and F. Pollmann. “Dissipation-assisted operator evolution method for capturing hydrodynamic transport.” *arXiv e-prints* arXiv:2004.05177, 2020.
- [150] S. Gopalakrishnan and R. Vasseur. “Kinetic theory of spin diffusion and superdiffusion in xxz spin chains.” *Phys. Rev. Lett.* **122**, p. 127202, 2019. doi:[10.1103/PhysRevLett.122.127202](https://doi.org/10.1103/PhysRevLett.122.127202).
- [151] B. Bertini, M. Collura, J. De Nardis, and M. Fagotti. “Transport in out-of-equilibrium xxz chains: Exact profiles of charges and currents.” *Phys. Rev. Lett.* **117**, p. 207201, 2016. doi:[10.1103/PhysRevLett.117.207201](https://doi.org/10.1103/PhysRevLett.117.207201).
- [152] O. A. Castro-Alvaredo, B. Doyon, and T. Yoshimura. “Emergent hydrodynamics in integrable quantum systems out of equilibrium.” *Phys. Rev. X* **6**, p. 041065, 2016. doi:[10.1103/PhysRevX.6.041065](https://doi.org/10.1103/PhysRevX.6.041065).
- [153] T. Rakovszky. Unpublished, 2022.
- [154] T. Mori and T. Shirai. “Resolving a discrepancy between liouvillian gap and relaxation time in boundary-dissipated quantum many-body systems.” *Phys. Rev. Lett.* **125**, p. 230604, 2020. doi:[10.1103/PhysRevLett.125.230604](https://doi.org/10.1103/PhysRevLett.125.230604).
- [155] P. W. Anderson. “Absence of diffusion in certain random lattices.” *Phys. Rev.* **109**, pp. 1492, 1958. doi:[10.1103/PhysRev.109.1492](https://doi.org/10.1103/PhysRev.109.1492).
- [156] I. V. Gornyi, A. D. Mirlin, and D. G. Polyakov. “Interacting electrons in disordered wires: Anderson localization and low- t transport.” *Phys. Rev. Lett.* **95**, p. 206603, 2005. doi:[10.1103/PhysRevLett.95.206603](https://doi.org/10.1103/PhysRevLett.95.206603).

- [157] M. Serbyn, Z. Papić, and D. A. Abanin. “Local conservation laws and the structure of the many-body localized states.” *Phys. Rev. Lett.* **111**, p. 127201, 2013. doi:[10.1103/PhysRevLett.111.127201](https://doi.org/10.1103/PhysRevLett.111.127201).
- [158] J. A. Kjäll, J. H. Bardarson, and F. Pollmann. “Many-body localization in a disordered quantum ising chain.” *Phys. Rev. Lett.* **113**, p. 107204, 2014. doi:[10.1103/PhysRevLett.113.107204](https://doi.org/10.1103/PhysRevLett.113.107204).
- [159] B. Bauer and C. Nayak. “Area laws in a many-body localized state and its implications for topological order.” *Journal of Statistical Mechanics: Theory and Experiment* **2013**, p. P09005, 2013. doi:[10.1088/1742-5468/2013/09/p09005](https://doi.org/10.1088/1742-5468/2013/09/p09005).
- [160] V. Ros, M. Müller, and A. Scardicchio. “Integrals of motion in the many-body localized phase.” *Nuclear Physics B* **891**, pp. 420, 2015. doi:<https://doi.org/10.1016/j.nuclphysb.2014.12.014>.
- [161] J. Z. Imbrie, V. Ros, and A. Scardicchio. “Local integrals of motion in many-body localized systems.” *Annalen der Physik* **529**, p. 1600278, 2017. doi:<https://doi.org/10.1002/andp.201600278>.
- [162] J. Zhang, P. W. Hess, A. Kyprianidis, P. Becker, A. Lee, J. Smith, G. Pagano, I.-D. Potirniche, A. C. Potter, A. Vishwanath, N. Y. Yao, and C. Monroe. “Observation of a discrete time crystal.” *Nature* **543**, pp. 217, 2017. doi:[10.1038/nature21413](https://doi.org/10.1038/nature21413). arXiv:[1609.08684v1](https://arxiv.org/abs/1609.08684v1).
- [163] S. Choi, J. Choi, R. Landig, G. Kucsko, H. Zhou, J. Isoya, F. Jelezko, S. Onoda, H. Sumiya, V. Khemani, C. von Keyserlingk, N. Y. Yao, E. Demler, and M. D. Lukin. “Observation of discrete time-crystalline order in a disordered dipolar many-body system.” *Nature* **543**, pp. 221, 2017. doi:[10.1038/nature21426](https://doi.org/10.1038/nature21426). arXiv:[1610.08057](https://arxiv.org/abs/1610.08057).
- [164] G. D. Chiara, S. Montangero, P. Calabrese, and R. Fazio. “Entanglement entropy dynamics of heisenberg chains.” *Journal of Statistical Mechanics: Theory and Experiment* **2006**, pp. P03001, 2006. doi:[10.1088/1742-5468/2006/03/p03001](https://doi.org/10.1088/1742-5468/2006/03/p03001).
- [165] J. H. Bardarson, F. Pollmann, and J. E. Moore. “Unbounded growth of entanglement in models of many-body localization.” *Phys. Rev. Lett.* **109**, p. 017202, 2012. doi:[10.1103/PhysRevLett.109.017202](https://doi.org/10.1103/PhysRevLett.109.017202).
- [166] M. Žnidarič, T. c. v. Prosen, and P. Prelovšek. “Many-body localization in the heisenberg xxz magnet in a random field.” *Phys. Rev. B* **77**, p. 064426, 2008. doi:[10.1103/PhysRevB.77.064426](https://doi.org/10.1103/PhysRevB.77.064426).
- [167] A. Nandori, H. Kim, and D. A. Huse. “Entanglement spreading in a many-body localized system.” *Phys. Rev. B* **90**, p. 064201, 2014. doi:[10.1103/PhysRevB.90.064201](https://doi.org/10.1103/PhysRevB.90.064201).
- [168] D. J. Luitz, N. Laflorencie, and F. Alet. “Many-body localization edge in the random-field Heisenberg chain.” *Phys. Rev. B* **91**, p. 081103, 2015. doi:[10.1103/PhysRevB.91.081103](https://doi.org/10.1103/PhysRevB.91.081103). arXiv:[1411.0660v2](https://arxiv.org/abs/1411.0660v2).
- [169] T. C. Berkelbach and D. R. Reichman. “Conductivity of disordered quantum lattice models at infinite temperature: Many-body localization.” *Phys. Rev. B* **81**, p. 224429,

2010. doi:[10.1103/PhysRevB.81.224429](https://doi.org/10.1103/PhysRevB.81.224429).
- [170] F. Pietracaprina, G. Parisi, A. Mariano, S. Pascazio, and A. Scardicchio. “Entanglement critical length at the many-body localization transition.” *Journal of Statistical Mechanics: Theory and Experiment* **2017**, p. 113102, 2017. doi:[10.1088/1742-5468/aa9338](https://doi.org/10.1088/1742-5468/aa9338).
- [171] S. D. Geraedts, N. Regnault, and R. M. Nandkishore. “Characterizing the many-body localization transition using the entanglement spectrum.” **19**, p. 113021, 2017. doi:[10.1088/1367-2630/aa93a5](https://doi.org/10.1088/1367-2630/aa93a5).
- [172] A. Lukin, M. Rispoli, R. Schittko, M. E. Tai, A. M. Kaufman, S. Choi, V. Khemani, J. Léonard, and M. Greiner. “Probing entanglement in a many-body-localized system.” *Science* **364**, pp. 256, 2019. doi:[10.1126/science.aau0818](https://doi.org/10.1126/science.aau0818).
- [173] B. Chiaro, C. Neill, A. Bohrdt, M. Filippone, F. Arute, K. Arya, R. Babbush, D. Bacon, J. Bardin, R. Barends, S. Boixo, D. Buell, B. Burkett, Y. Chen, Z. Chen, R. Collins, A. Dunsworth, E. Farhi, A. Fowler, B. Foxen, C. Gidney, M. Giustina, M. Harrigan, T. Huang, S. Isakov, E. Jeffrey, Z. Jiang, D. Kafri, K. Kechedzhi, J. Kelly, P. Klimov, A. Korotkov, F. Kostritsa, D. Landhuis, E. Lucero, J. McClean, X. Mi, A. Megrant, M. Mohseni, J. Mutus, M. McEwen, O. Naaman, M. Neeley, M. Niu, A. Petukhov, C. Quintana, N. Rubin, D. Sank, K. Satzinger, A. Vainsencher, T. White, Z. Yao, P. Yeh, A. Zalcman, V. Smelyanskiy, H. Neven, S. Gopalakrishnan, D. Abanin, M. Knap, J. Martinis, and P. Roushan. “Growth and preservation of entanglement in a many-body localized system.” 2019. arXiv:[1910.06024](https://arxiv.org/abs/1910.06024).
- [174] V. Khemani, F. Pollmann, and S. L. Sondhi. “Obtaining Highly Excited Eigenstates of Many-Body Localized Hamiltonians by the Density Matrix Renormalization Group Approach.” *Phys. Rev. Lett.* **116**, 2016. doi:[10.1103/PhysRevLett.116.247204](https://doi.org/10.1103/PhysRevLett.116.247204). arXiv:[arXiv:1509.00483v2](https://arxiv.org/abs/1509.00483v2).
- [175] X. Yu, D. Pekker, and B. K. Clark. “Finding matrix product state representations of highly excited eigenstates of many-body localized hamiltonians.” *Phys. Rev. Lett.* **118**, p. 017201, 2017. doi:[10.1103/PhysRevLett.118.017201](https://doi.org/10.1103/PhysRevLett.118.017201).
- [176] S. P. Lim and D. N. Sheng. “Many-body localization and transition by density matrix renormalization group and exact diagonalization studies.” *Phys. Rev. B* **94**, p. 045111, 2016. doi:[10.1103/PhysRevB.94.045111](https://doi.org/10.1103/PhysRevB.94.045111).
- [177] M. Serbyn, A. A. Michailidis, D. A. Abanin, and Z. Papić. “Power-law entanglement spectrum in many-body localized phases.” *Phys. Rev. Lett.* **117**, p. 160601, 2016. doi:[10.1103/PhysRevLett.117.160601](https://doi.org/10.1103/PhysRevLett.117.160601).
- [178] L. Herviou, S. Bera, and J. H. Bardarson. “Multiscale entanglement clusters at the many-body localization phase transition.” *Phys. Rev. B* **99**, p. 134205, 2019. doi:[10.1103/PhysRevB.99.134205](https://doi.org/10.1103/PhysRevB.99.134205).
- [179] F. Pietracaprina, N. Macé, D. J. Luitz, and F. Alet. “Shift-invert diagonalization of large many-body localizing spin chains.” *SciPost Phys.* **5**, p. 45, 2018. doi:[10.21468/SciPostPhys.5.5.045](https://doi.org/10.21468/SciPostPhys.5.5.045).

- [180] M. Serbyn, Z. Papić, and D. A. Abanin. “Criterion for many-body localization-delocalization phase transition.” *Phys. Rev. X* **5**, p. 041047, 2015. doi:[10.1103/PhysRevX.5.041047](https://doi.org/10.1103/PhysRevX.5.041047).
- [181] A. D. Luca and A. Scardicchio. “Ergodicity breaking in a model showing many-body localization.” *EPL (Europhysics Letters)* **101**, p. 37003, 2013. doi:[10.1209/0295-5075/101/37003](https://doi.org/10.1209/0295-5075/101/37003).
- [182] M. E. J. Newman and M. Girvan. “Finding and evaluating community structure in networks.” *Phys. Rev. E* **69**, p. 026113, 2004. doi:[10.1103/PhysRevE.69.026113](https://doi.org/10.1103/PhysRevE.69.026113).
- [183] M. Girvan and M. E. J. Newman. “Community structure in social and biological networks.” *Proceedings of the National Academy of Sciences* **99**, pp. 7821, 2002. doi:[10.1073/pnas.122653799](https://doi.org/10.1073/pnas.122653799).
- [184] M. E. J. Newman. “Analysis of weighted networks.” *Phys. Rev. E* **70**, p. 056131, 2004. doi:[10.1103/PhysRevE.70.056131](https://doi.org/10.1103/PhysRevE.70.056131).
- [185] S. Fortunato. “Community detection in graphs.” *Physics Reports* **486**, pp. 75 , 2010. doi:<https://doi.org/10.1016/j.physrep.2009.11.002>.
- [186] G. De Tomasi, S. Bera, J. H. Bardarson, and F. Pollmann. “Quantum mutual information as a probe for many-body localization.” *Phys. Rev. Lett.* **118**, p. 016804, 2017. doi:[10.1103/PhysRevLett.118.016804](https://doi.org/10.1103/PhysRevLett.118.016804).
- [187] M. M. Wolf, F. Verstraete, M. B. Hastings, and J. I. Cirac. “Area laws in quantum systems: Mutual information and correlations.” *Phys. Rev. Lett.* **100**, p. 070502, 2008. doi:[10.1103/PhysRevLett.100.070502](https://doi.org/10.1103/PhysRevLett.100.070502).
- [188] R. X. Dong and D. L. Zhou. “Correlation function and mutual information.” *Journal of Physics A: Mathematical and Theoretical* **43**, p. 445302, 2010. doi:[10.1088/1751-8113/43/44/445302](https://doi.org/10.1088/1751-8113/43/44/445302).
- [189] M. A. Valdez, D. Jaschke, D. L. Vargas, and L. D. Carr. “Quantifying complexity in quantum phase transitions via mutual information complex networks.” *Phys. Rev. Lett.* **119**, p. 225301, 2017. doi:[10.1103/PhysRevLett.119.225301](https://doi.org/10.1103/PhysRevLett.119.225301).
- [190] A. A. Bagrov, M. Danilov, S. Brener, M. Harland, A. I. Lichtenstein, and M. I. Katsnelson. “Detecting quantum critical points in the t- \hat{t} fermi-hubbard model via complex network theory.” *Scientific Reports* **10**, p. 20470, 2020. doi:[10.1038/s41598-020-77513-0](https://doi.org/10.1038/s41598-020-77513-0).
- [191] B. Sokolov, M. A. C. Rossi, G. García-Pérez, and S. Maniscalco. “Emergent entanglement structures and self-similarity in quantum spin chains.” *arXiv e-prints* arXiv:2007.06989, 2020.
- [192] T. Szoldra, P. Sierant, K. Kottmann, M. Lewenstein, and J. Zakrzewski. “Detecting ergodic bubbles at the crossover to many-body localization using neural networks.” *arXiv e-prints* arXiv:2106.01811, 2021.
- [193] B. H. Good, Y.-A. de Montjoye, and A. Clauset. “Performance of modularity maximization in practical contexts.” *Phys. Rev. E* **81**, p. 046106, 2010.

- doi:[10.1103/PhysRevE.81.046106](https://doi.org/10.1103/PhysRevE.81.046106).
- [194] D. Abanin, J. Bardarson, G. De Tomasi, S. Gopalakrishnan, V. Khemani, S. Parameswaran, F. Pollmann, A. Potter, M. Serbyn, and R. Vasseur. “Distinguishing localization from chaos: Challenges in finite-size systems.” *Annals of Physics* **427**, p. 168415, 2021. doi:<https://doi.org/10.1016/j.aop.2021.168415>.
- [195] N. Pancotti, G. Giudice, J. I. Cirac, J. P. Garrahan, and M. C. Bañuls. “Quantum east model: Localization, nonthermal eigenstates, and slow dynamics.” *Phys. Rev. X* **10**, p. 021051, 2020. doi:[10.1103/PhysRevX.10.021051](https://doi.org/10.1103/PhysRevX.10.021051).
- [196] N. Pomata, S. Ganeshan, and T.-C. Wei. “In search of a many-body mobility edge with matrix product states in a Generalized Aubry-André model with interactions.” *arXiv e-prints* arXiv:2012.09853, 2020.
- [197] D. J. Luitz and Y. B. Lev. “Absence of slow particle transport in the many-body localized phase.” *Phys. Rev. B* **102**, p. 100202, 2020. doi:[10.1103/PhysRevB.102.100202](https://doi.org/10.1103/PhysRevB.102.100202).
- [198] J. Smith, A. Lee, P. Richerme, B. Neyenhuis, P. W. Hess, P. Hauke, M. Heyl, D. A. Huse, and C. Monroe. “Many-body localization in a quantum simulator with programmable random disorder.” *Nature Physics* **12**, pp. 907, 2016. doi:[10.1038/nphys3783](https://doi.org/10.1038/nphys3783).
- [199] G. De Tomasi, F. Pollmann, and M. Heyl. “Efficiently solving the dynamics of many-body localized systems at strong disorder.” *Phys. Rev. B* **99**, p. 241114, 2019. doi:[10.1103/PhysRevB.99.241114](https://doi.org/10.1103/PhysRevB.99.241114).
- [200] A. Safavi-Naini, M. L. Wall, O. L. Acevedo, A. M. Rey, and R. M. Nandkishore. “Quantum dynamics of disordered spin chains with power-law interactions.” *Phys. Rev. A* **99**, p. 033610, 2019. doi:[10.1103/PhysRevA.99.033610](https://doi.org/10.1103/PhysRevA.99.033610).
- [201] W. S. Bakr, J. I. Gillen, A. Peng, S. Fölling, and M. Greiner. “A quantum gas microscope for detecting single atoms in a hubbard-regime optical lattice.” *Nature* **462**, pp. 74, 2009. doi:[10.1038/nature08482](https://doi.org/10.1038/nature08482).
- [202] J. F. Sherson, C. Weitenberg, M. Endres, M. Cheneau, I. Bloch, and S. Kuhr. “Single-atom-resolved fluorescence imaging of an atomic mott insulator.” *Nature* **467**, pp. 68, 2010. doi:[10.1038/nature09378](https://doi.org/10.1038/nature09378).
- [203] H. Bernien, S. Schwartz, A. Keesling, H. Levine, A. Omran, H. Pichler, S. Choi, A. S. Zibrov, M. Endres, M. Greiner, V. Vuletić, and M. D. Lukin. “Probing many-body dynamics on a 51-atom quantum simulator.” *Nature* **551**, pp. 579, 2017.
- [204] S. Scherg, T. Kohlert, P. Sala, F. Pollmann, B. Hebbe Madhusudhana, I. Bloch, and M. Aidelsburger. “Observing non-ergodicity due to kinetic constraints in tilted fermi-hubbard chains.” *Nature Communications* **12**, p. 4490, 2021.
- [205] L. Clinton, J. Bausch, and T. Cubitt. “Hamiltonian simulation algorithms for near-term quantum hardware.” *Nature Communications* **12**, p. 4989, 2021.
- [206] A. Smith, M. S. Kim, F. Pollmann, and J. Knolle. “Simulating quantum many-body dynamics on a current digital quantum computer.” *npj Quantum Information* **5**, p. 106,

2019.

- [207] T. Klein Kvarning, L. Herviou, and J. H. Bardarson. “Time-evolution of local information: thermalization dynamics of local observables.” *arXiv e-prints* arXiv:2105.11206, 2021.
- [208] C. D. White, M. Zaletel, R. S. K. Mong, and G. Refael. “Quantum dynamics of thermalizing systems.” *Phys. Rev. B* **97**, p. 035127, 2018. doi:[10.1103/PhysRevB.97.035127](https://doi.org/10.1103/PhysRevB.97.035127).
- [209] A. Lerose, M. Sonner, and D. A. Abanin. “Overcoming the entanglement barrier in quantum many-body dynamics via space-time duality.” *arXiv e-prints* arXiv:2201.04150, 2022.